TECHNISCHE
UNIVERSITÄT
WIEN
Vienna | Austria

1. Gutachter

2. Gutachter

DISSERTATION

Interaction of Ultra-cold Atoms with Confined Light Fields

Ausgeführt zum Zwecke der Erlangung des akademischen Grades eines Doktors der technischen Wissenschaften unter Leitung von

Univ.Prof. Dipl.-Ing. Dr.techn. Hannes-Jörg Schmiedmayer
E141
Atominstitut

eingereicht an der Technischen Universität Wien,

Fakultät für Physik,

von

Dipl.-Ing. Dominik Fischer
0025212
Erne-Seder-Gasse 8/2/107, 1030 Wien

Wien, am

Kurzzusammenfassung

Wechselwirkung ultrakalter Atome mit räumlich beschränkten Lichtfeldern

In dieser Arbeit werden zwei Experimente beschrieben, die die Wechselwirkung von ultrakalten Rubidium-Atomen mit von rund 1 Mikrometer großen optischen Elementen geformten Lichtfeldern analysieren, die auf einer Oberfläche integriert sind, auf der sich auch die Drahtstrukturen für das magnetische Fangen von Atomen befinden.

Das erste Experiment, das "Mikrooptik-Experiment", basiert auf einem Atomchip mit lithographisch geformten Golddrähten and Mikrostrukturen aus dem Epoxidharz SU-8 zur Befestigung optischer Fasern auf dem Chip. Der Strom durch diese Drähte in Kombination mit einem externen Magnetfeld erzeugt eine präzise geformte Magnetfalle mit einem starken Einschluss in den zwei Richtungen senkrecht und einem Schwachen entlang des Chipdrahtes. In dieser Falle kann man mithilfe von Verdampfungskühlen ein quasi-1D Bose-Einstein-Kondensat (BEC) erzeugen, welches in einen magnetischen Wellenleiter geladen werden kann. Entlang dieses Führungsdrahtes können die Atome propagieren, bis sie bei der Chipregion mit dem Faserdetektor angekommen sind, welcher mithilfe der SU-8-Strukuren am Chip integriert ist. Eine Faser, mit einem als Linse agierenden Konus, fokussiert resonantes Licht auf die beförderten Atome und eine Multimodenfaser sammelt Fluoreszenzphotonen der Atome ein. Das ergibt eine Detektionseffizienz von 66% für einzelne Atome in einem thermischen Gas bei 50 μK, was eine Messung des Atomflusses durch den Detektor ermöglicht. Jedoch bei tieferen Temperaturen in der Nähe der Übergangstemperatur zum BEC ist die Dynamik der Atome im Detektionslicht komplexer und sie bleiben für längere Zeit - in der Größenordnung einer Sekunde - in der Nähe des Detekors gefangen. Die Atomoptik eines entlang des Wellenleiters propagierenden Atomensembles und dessen Auftreffen auf die Barriere am Ende des Wellenleiters wird für den Fall eines idealen Gas und eines 1d BECs bei $T = 0$ diskutiert. Das Verhalten der Atome im optischen Potential im Fokus der Konusfaser wird experimentell mit dem resonantem Detektionslicht, wo die Kraft durch den Strahlungsdruck in einem inhomogenen Magnetfeld erzeugt wird, und mit einer nichtresonanten Dipolbarriere durchgeführt und verglichen.

Das zweite Experiment, das "Nanofaser-Resonator-Experiment", ersetzt das erste durch ein neues Vakuumsystem, neue Spulen und Drahtstrukturen, welche die Erzeugung einer magneto-optischen Falle (MOT) in der Nähe einer Oberfläche mit Kupferstrukturen für das Magnetfeld und einer darauf montierten Nanofaser möglichen. Diese ist eine optische Faser, bei der ein Stück durch Erhitzen und Ziehen auf einen Durchmesser von nur 400 nm gebracht wird. Dort wird das meiste Licht außerhalb der Faser in einem radial abklingenden Lichtfeld transportiert. In der MOT gekühlte und gefangene Atome werden durch Verschieben des Magnetfeld-Minimums zur Position der Nanofaser gebracht, wo sie das durch die Nanofaser transmittierte Licht absorbieren. Um die Atom-Licht-Wechselwirkung zu erhöhen, wird in einem zweiten Schritt ein faserbasierter Fabry-Perot-Resonator verwendet. In diesem aus zwei Bragg-Spiegeln bestehenden Resonator, welche mit einem UV-Laser direkt in das Fasermaterial eingeschriebenen werden, passieren die Photonen das Atom ≈ 20 mal, was die Atom-Licht-Kopplung um diesen Faktor erhöht. Diese Wechselwirkung kann durch die Analyse der Verschiebung der Resonanzfrequenz des Resonators untersucht werden.

Abstract

Interaction of Ultra-cold atoms with Confined Light fields

In this thesis two experiments are described which analyse the interaction of ultra-cold rubidium atoms with the light fields formed by micrometer-sized optical elements close to a surface containing wire structures responsible for magnetically trapping the atoms.

The first experiment, the "micro-optics experiment", is based on an atom chip with lithographically patterned gold wires and micro-structures built from the epoxy resist SU-8 for attaching optical fibres on top of the chip. The current through these wires in combination with an external magnetic field creates a geometrically well defined magnetic trap with a strong confinement in the two directions perpendicular a weak one along the wire. In this trap it is possible to evaporatively cool to a quasi-1d Bose-Einstein condensate (BEC). This can be loaded into a magnetic waveguide, where the atoms can propagate along a guiding wire towards a chip region with a fibre detector held by the SU-8 structures on the chip. A tapered lensed fibre focuses resonant light onto the guided atoms and a multimode fibre collects fluorescence photons from the atoms. This allows for up to 66% detection efficiency for single atoms from a thermal gas at $\approx 50\ \mu$K and it is possible to measure the atomic flux through the detector. For smaller temperatures across the transition to a BEC the atomic dynamics in the detection light is more complex and they are trapped near the detector for a long time on the order of 1 s. The atom optics of an atomic ensemble propagating along a 1d waveguide and the closing at the end of the waveguide by the optical potential produced by the detection fibre, causing the atomic trapping, is investigated further by comparing this resonant potential produced by the radiation pressure in an inhomogeneous magnetic field to an off-resonant dipole barrier and are discussed for both an ideal gas and a 1d BEC at $T = 0$.

The second experiment, the "nanofibre cavity experiment", is replacing the first one by implementing a new vacuum system, new coils and wire structures, enabling a magneto-optical trap (MOT) near a surface with copper structures providing the magnetic field and a nanofibre mounted close to it. This is an optical fibre with one part heated and pulled to a thin waist of only 400 nm diameter, where most of the light is guided outside of it in a radially evanescent field. Atoms, which are cooled and trapped in a MOT, are transferred to the position of the nanofibre by shifting the magnetic field minimum inducing absorption of the light transmitted trough the nanofibre. In order to enhance the atom-light interaction, a fibre-based Fabry-Perot resonator is used in a second step. In this resonator, which is built of two Bragg mirrors, directly written into

the fibre material with a UV laser, the photons pass the atoms 20 times thus increasing the atom-light coupling by this factor. This interaction can be probed by analysing the shift of the cavity resonance frequency.

Contents

1. Introduction

The scientific investigation of atoms is done by letting them interact with other physical entities. The most accessible scatterer is light, because of its diversity of sources and detectors - and of course its availability. For a strong atom-light interaction the electric field at the position of the atom has to be large. This can be achieved by confining the light intensity to a small volume, ideally to a region with the size of the atom. The relevant size in this case is not the radius of the outermost electron shell, which is a few $\mathring{A}$ for rubidium [14], but it is the size of the atom-light scattering cross section, which is on the order of the light wavelength squared [**?**]. Thus it suffices to confine the light beam to an area with a diameter of approximately 1 μm, which is achievable by tightly focusing a light beam. With usual macroscopic lenses such a micrometer-scale alignment is mechanically challenging and the light mode entering the lens has to be perfectly collimated. This thesis describes two experiments using coherent light [25] confined to such a small area using optical elements with a size on the order of a micrometer as a tool to study ensembles of ultra-cold atoms. Both experiments have a proof-of-principle character, since they are unique in their approach to integrate a combination of magnetic microtraps [22] for atoms and optical devices on top of a surface allowing precise geometric alignment of both tools. Many things have to be understood before a coherent, versatile optical control of a degenerate atomic ensemble with tunable parameters can be implemented.

The first experiment, the so called micro-optics experiment, is using a surface mounted fibre detector for atomic arrival times [33]. It has a small volume due to the incoming and scattered light being fibre-coupled and the detection region being defined by a small focal spot of only 5 μm diameter. This leads to a large suppression of background noise as well as a good time resolution. Converting time intervals into spatial distances one of the best spatial resolutions for an insitu density measurement of ultra-cold atom clouds is obtained. This detection scheme is tested for low temperatures in this thesis, across the phase transition from a thermal gas to a Bose-Einstein condensate [3]. The dynamics in such a detector has to be understood, in order to control and improve its time resolution and its detection efficiency for atoms in this regime.

So far only the light confinement perpendicular to the beam was considered. Since there are no real traps for light [17], at least the time a photon spends in a certain region can be increased by enclosing this region with two mirrors, where the photon is reflected multiple times. This Fabry-Perot cavity [62] is utilised in the second experiment, the so called nanofibre cavity experiment, where two optical tools are combined. First the light is again confined to an area with a diameter of the light wavelength by using a fibre, but this time the light stays guided in a thin part of the fibre, where most of the light is travelling outside of it [38]. Second the a Fabry-Perot cavity can be built around

the thin part by enclosing it with two fibre Bragg mirrors [71]. Then the photons pass the atoms around 20 times, resulting in a larger electric field by this factor. Within those mirrors atoms can couple to it along this whole thin part, meaning that many of them can interact simultaneously with the guided cavity-enhanced light, therefore a large influence in the properties of the light can be expected. This change is then again an indicator for the properties of the atomic ensemble. Such properties can be determined even without destroying the atom cloud by using highly off-resonant light . This dispersion due to different atomic densities is tested in this thesis.
In this introduction first its structure is described 1.1, then the main ideas and intentions behind the experiments are discussed 1.2 and a list of the 10 main results of this thesis is given 1.3.

1.1. Organisation of the thesis

Since within this thesis two distinct experiments with integrated optics were performed, their description is divided into two completely separated parts. Part II discusses the micro-optics experiment and part III describes the nanofibre cavity experiment. These two experimental parts can be read separately with the use of a theoretical introduction in part I, where two ideas are discussed in a more general framework: first, in chapter 2, the 1d atom optics of an atomic ensemble allowed to undergo a quasi-free motion in a magnetic wave guide, needed for the micro-optics experiment; and second, in chapter 3, the scattering processes between light from integrated sources with an atom that can occur both in free space and inside a Fabry-Perot resonator. Other theoretical discussions are given in the corresponding experimental chapters in a more phenomenological way.

1.2. Motivation: Bringing atoms and photons together

Here a couple of applications of the devices described by this thesis are given. Some have already been built and tested, others are possible applications in future projects.

Seeing single atoms: fluorescence detection

> “Habens’ schon eins gesehn? ”(Ernst Mach)

The answer to Mach’s rhetorical question, whether it would be possible to see single atoms, has been shown to be yes in the last decades (for example with the atomic force microscope [8]). In this thesis a fluorescence detector is introduced which is capable not to see but to detect single atoms with a high probability, and with some changes in the detector technology even with almost 100%. Some possible applications of such a detector are introduced below.
The atom chip [57, 21] provides a good environment for one-dimensional physical systems, since its wires can have large aspect ratios. In usual atom chip experiments the coldest atomic ensembles are in the quasicondensate regime [16], where the atoms are in

the ground state in the two tightly confined degrees of freedom perpendicular to the trap wire, but there are still phonon-like excitations along the wire direction. By going to lower temperatures and/or smaller densities one should enter the Tonks-Giradeau regime [54], which is characterized by a strong repelling interaction between the atoms due to the geometric inhibition of inter-atomic passage without scattering. For quasicondensates the density is high and therefore absorption imaging with large objectives outside the vacuum chamber is feasible with a reasonable signal-to-noise ratio. But ensembles in the Tonks-Giradeau-regime have small atomic densities, thus a fluorescence detection scheme becomes favourable. The single atom detector presented in this thesis is limited by the atomic shot noise only, which means it should be feasible to measure the density distribution of a strongly interacting atomic ensemble using a large enough sample of experimental repeats.

A second application of this detector, though not tested so far, would be the measurement of the density distribution of fermionic quasi-1d gases in order to determine its equation of state. This has been done in 3d with a cavity [49].

Seeing single atoms at different places: non-local correlations in matter

It has been shown that it is possible to create correlated atom pairs propagating along opposite directions along the chip wire trap with the same momentum modulus by controlled shaking of the magnetic potential [11]. Using two detectors on both ends of the wire trap the correlations between these atoms could be probed directly with a coincidence measurement, or with the help of an atomic beam splitter - created by an optical dipole trap in the centre - it should be possible to perform Hong-Ou-Mandel type interferometry [51] to directly demonstrate atomic entanglement.

Another scheme to produce non-local density correlations in the atomic ensemble is to introduce an acoustic horizon within the atom cloud [6, 56]. This would be a proof of an acoustic analogue of Hawking radiation. This effect is expected to be very small, thus fluorescence detection seems to be the favourable option.

The shadow of the atoms: absorption detection

Instead of fluorescence detection the attenuation of a light beam can be used in an absorption detection scheme. The standard imaging technique to quantify the properties of ultra-cold atomic ensembles using CCD cameras is absorption imaging, where the attenuation of an incident resonant light beam is imaged and the column density of the atomic cloud can be measured [37]. A similar approach uses optical fibres to confine the light to a beam size comparable to the atomic absorption cross section using a tapered lensed fibre tip, saturating the atom-light coupling. This only creates a focus with a short waist. In order to overcome the proportionality between waist length and focal spot size a nanofibre [23] can be used instead. Here the light is guided along a fibre with a diameter of half the light wavelength. A standard optical fibre is tapered towards this thin waist in such way that the light is always guided in a single mode until most of the light power is outside of the fibre, acting solely as the core material, in vacuum, which then acts as the cladding, in a radially exponentially decaying evanescent field. Here a high optical density can be reached because atoms see an intense light power confined to an area on the order of the size of the scattering cross section along the whole waist of the nanofibre, which is npt diffraction limited and can be several millimetres long, thus allowing many atoms to couple strongly to the light field.

The return of the light: slowed down and stored light

The large optical density achievable with the nanofibre described in the previous section can be used in a stimulated Raman scheme, where two light fields couple three atomic levels in such a way that by shining in a strong pump light the absorption and refractive index for the second light field is strongly frequency dependent, resulting in a narrow transparency window where the detunings of the two light beams meet, leading to electromagnetically induced transparency (EIT) [20]. In this frequency region there is also a large dispersion which results in very small group velocities in the light-driven atomic medium. The speed of light of the probe beam can be slowed down to tens of metres per second (firstly demonstrated in [29] and recently in [61]). In a similar procedure light can also be stopped completely inside of the medium, which is a special application for atomic polaritons described in the next paragraph.

Photons plus atoms: a 1d Polariton gas

In the schemes discussed above the photonic information can be transferred to a polariton, the coherent superposition of the light field and a spin wave in the atomic ensemble. By carefully ramping down the pump laser the mixing between these two components can be adiabatically changed, such that the initial optical information is stored in the spin wave. The storage procedure can be reversed and the optical information can be retrieved with an efficiency depending on the atomic coherence. This can act as a quantum memory or a repeater in a proposed quantum network [19].

Adding a fourth atomic level to the Raman scheme, which also couples to the signal light field, one can achieve a situation where the refractive index for the signal light propagating trough the medium, driven by the pump laser, is dependent on its own intensity and therefore creates a non-linear susceptibility, or in other words, a strong photon-photon interaction. It can be shown [12], that such a system of interacting polaritons, created by a single-mode beam, is describable by the Lieb-Liniger model [41] for 1d strongly interacting gases. This strong interaction can lead to number squeezing in a photon gas, representing a non-classical light source.

Photons behind bars: Cavity QED using Bragg mirrors

Besides the possibility to store a photon inside a medium, as discussed above, there is no way to trap a photon without a medium. But it is possible to increase the amount of time a photon spends at a certain spatial region by enclosing it with mirrors such that the photons are reflected many times before they leave this cavity.

This can be done for example with a Fabry-Perot resonator, which is made from two opposing mirrors. The amount of photon dwell time leads to a strong cavity field, which strongly enhances the coupling of photons and atoms inside the resonator. This can be used for a highly efficient detection and manipulation of single atoms [39] and BECs [13]. It is also possible to influence the mechanical motion of the atoms, and thus to trap and cool them within the cavity [58]. This leads to a photon-mediated mechanical coupling of the rigid cavity mirrors and the atoms [67]. Already the presence of the empty resonator can completely alter the atomic scattering behaviour leading to an increased [4] or inhibited photon emission [40] and also to collective phenomena, such as spontaneous self-organisation [7]. Finally there is also the possibility (at least in the microwave regime) to reverse the role of cavity photons as probe and atoms as investigated sample by using atoms to detect the classical or highly non-classical photon state in the cavity [28].

In order to add a Fabry-Perot resonator to the nanofibre, two grids of alternating refractive index can be added to the fibre directly enclosing the tapered part. These grids act as Bragg mirrors for a certain wavelength and thus form the resonator [71].

1.3. The main goals of this thesis

The main claims verified by this thesis are:

Fluorescence detector experiment

1. Ultra-cold rubidium vapours can be confined in micro-fabricated wire traps on a so called atom chip and loaded into a magnetic wave guide

2.2,2.3,4.2

2. Atoms propagating along this wave guide can be detected with an integrated fibre-based fluorescence detector

4.3

3. The mechanical dynamics of the atoms in the detection light field can be understood and related to a detection efficiency

5,7.1

4. The number of detected fluorescence photon counts can be associated uniquely with the number of atoms passing the detector

6

5. The measured atomic flux distribution is related to the atomic trajectory in the light field and to ensemble properties in the initial magnetic trap

2.3,7.2

Nanofibre cavity experiment

6. A new experiment can be implemented, providing the vacuum system, magnetic fields and laser system, for the production of a magneto-optical trap in the vicinity of a surface- mounted nanofibre

8,9

7. The cold rubidium vapour can be transported magnetically towards the evanescent light field at the nanofibre's waist with a diameter of 400 nm

9.2,10.1

8. The coupling of the atoms to this nanofibre light can be probed by the absorption of light transmitted through the nanofibre

3.1,3.2,10.2

9. A Fabry-Perot resonator can be built of Bragg mirrors laser-written into the fibre material enclosing the nanofibre waist

3.3,11.1,11.2

10. Atoms can be coupled to the standing wave inside this resonator, which can be probed by the action of atoms onto the resonance frequency of the transmitted light

3.311.3

Part I.

Theory

2. Matter wave optics in a magnetic guide

In the micro-optics experiment, a rate of arriving atoms is measured at the end of a magnetic waveguide which is loaded from an initially closed magnetic trap (see the experiment description in ch. 4). In order to understand this atom rate signal, the measured observable is defined (2.1) as atomic current j, which is the complete equivalent of the current in electronic circuits and in hydrodynamics (the equivalence with the latter and a Bose-Einstein condensate (BEC) is further used to obtain the equations of motion). In order to understand the dynamics of the propagation process of an atom cloud in the waveguide, the problem is split into separate parts: As an initial condition the atomic distribution in the closed trap has to be understood (2.2). Then the time-evolution of the atomic ensemble is discussed (2.3), first as a free expansion along the longitudinal direction, with which atomic flux at the detector can be calculated including corrections due to the potential of magnetic waveguide along the propagation axis of the atoms. These calculations are performed for an ideal gas and 1d BEC at $T = 0$. Both models are then compared to the experimental results in part II.

2.1. Measurement observable: the atomic flux

Photon clicks are measured in the detector and their timestamps are recorded. By integration a photon click rate is calculated which is proportional to the incoming rate of atoms, the inverse of their mean temporal arrival time distance (see a sketch in Figure 2.1). Thus this rate gives the flux of incoming atoms at a certain time. This observable can be formalised as

$$\hat{I}(z,t) = \frac{\hbar}{2mi}\left(\hat{\Psi}^\dagger(z,t)\frac{\partial}{\partial z}\hat{\Psi}(z,t) - \frac{\partial}{\partial z}\hat{\Psi}^\dagger(z,t)\hat{\Psi}(z,t)\right) \tag{2.1}$$

for the atomic annihilation operator $\hat{\Psi}(z,t)$. The measured flux is then its expectation value

$$j(z,t) := \langle \hat{I}(z,t) \rangle. \tag{2.2}$$

For many cases, most notably for an ideal gas and a Bose-Einstein condensate at $T = 0$, this factorises to

$$j(z,t) := n(z,t)v(z,t), \tag{2.3}$$

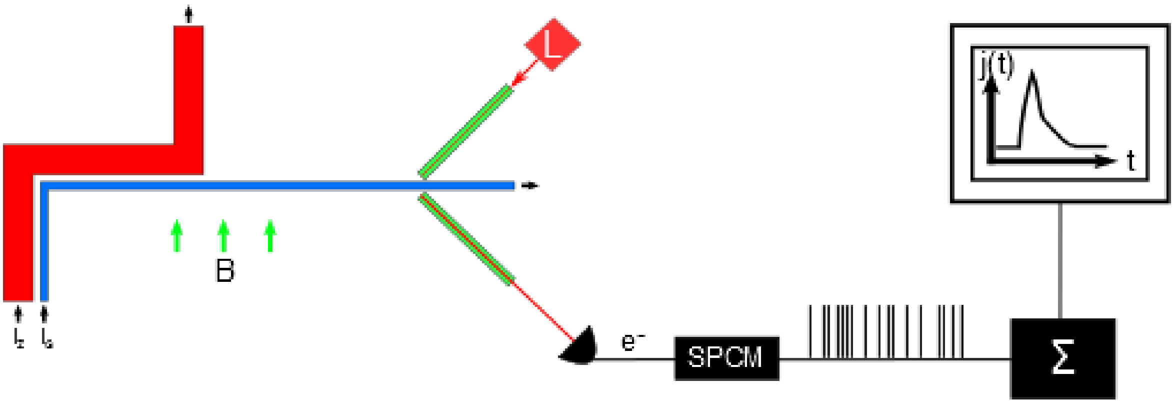

Figure 2.1.: Sketch of the detection scheme: the atoms propagating along the blue wire are detected by counting fluorescence photon clicks. These are converted to electronic timestamps which can be integrated (with an additional correction due to the detection efficiency) to an atomic flux distribution $j(t)$.

where $n(z,t)$ is the line density distribution and $v(z,t)$ the velocity distribution. The measurement in the detector cannot distinguish between a small density with a large incoming velocity and a large density with a small velocity. This ambiguity of a flux measurement can be a drawback, but with additional theoretical constraints one can obtain information about momentum and density distribution with just one observable. If the system is too complex to apply such constraints it is however only possible to measure a slice of the ensemble's phase space distribution instead.

2.2. Atom distribution in the initial trap

The atomic line density distribution in the initial trap is the starting point for the expansion of the atomic ensemble in the waveguide. The initial trap was measured to be harmonic, with longitudinal trap frequency of $2\pi \times 3$ Hz and radial trap frequency of $2\pi \times 1100$ Hz. The radial degrees of freedom can be separated and integrated away as will be shown first for an ideal gas in (2.2.1) and then for a BEC (2.2.2).

2.2.1. Density distribution of thermal atoms in the trap

Thermal atoms far from degeneracy in a deep magnetic trap can be treated with classical statistical mechanics, where losses from the trap or collisions with the background gas are neglected as well as an increase in atom number. Then a canonical distribution function within a harmonic trap

$$\rho_C(T,V,N) = \frac{e^{-\frac{H}{k_B T}}}{Z_C(T,V,N)} \tag{2.4}$$

can be assumed, with the total Hamilton function

$$H = \sum_{i=1}^{3N} \left(\frac{p_i^2}{2m} + \frac{m\omega_i^2 x_i^2}{2} \right), \tag{2.5}$$

being a sum over all three degrees of freedom of N atoms in the trap. The density distribution is given by the probability $p_1(z)$ to find a single atom at position z times the atom number. The single atom probability is derived from Equation 2.4 by integrating over $6N-1$ dimensions of the phase space, giving the one-dimensional density distribution along z,

$$n(z) = Np_1(z) = \frac{N}{\lambda_{dB}} \frac{\hbar\omega}{k_B T} e^{-\frac{m\omega^2 z^2}{2k_B T}}. \tag{2.6}$$

2.2.2. Density distribution of a BEC at T=0 in the trap

A Bose-Einstein condensate in an elongated trap is described by the one-dimensional time-independent Gross-Pitaevskii equation [46, 24]

$$\left[-\frac{\hbar^2}{2m} \frac{\partial^2}{\partial z^2} + V(z) + g_{1d} |\Psi(z)|^2 \right] \Psi(z) = \mu \Psi(z) \tag{2.7}$$

for the macroscopic wave function $\Psi(z)$ along the long axis z, which can be derived from the 3d equation [55] by integrating out the transverse degrees of freedom. This is a good description as long as the 1d criterion $\mu, k_B T < \hbar\omega_\perp$ and a 1d interaction strength $g_{1d} = 2\hbar\omega_\perp a$ can be introduced, with a being the atomic s-wave scattering length. For ultra-cold atoms the temperature is small enough that the kinetic energy term in Equation 2.7 can be neglected. This Thomas-Fermi approximation leads to an algebraic equation

$$g_{1d} n(z) + V(z) = \mu, \tag{2.8}$$

directly relating the density distribution $n(z) := |\Psi(z)|^2$ to the shape of the harmonic potential $V(z) = m\omega^2 z^2/2$, leading the inverted parabola shape

$$n(z) = \frac{\mu}{g_{1d}} - \frac{m\omega^2 z^2}{2g_{1d}} =: n_p \left(1 - \frac{z^2}{R^2} \right) \Theta(R - |z|), \tag{2.9}$$

with the peak density $n_p = \mu/g$ and the Thomas-Fermi radius $R = \sqrt{2\mu/m\omega^2}$. The density distribution is normalised to the atom number

$$N = \int n(z) dz, \tag{2.10}$$

which gives

$$n_p = \frac{3N}{4R} \tag{2.11}$$

for the peak density and

$$R = \left(\frac{3\hbar\omega_\perp aN}{m\omega^2}\right)^{1/3} \tag{2.12}$$

for the Thomas-Fermi radius. This means that the density profile is completely determined by the -usually known- trap frequencies and the atom number.

2.3. Propagation of atoms along a wave guide

The solution for the density distribution of an atomic ensemble in the static trap gives the an initial state of a time-dependent solution in the magnetic wave guide. Loading into this guide is done by changing the magnetic fields within 200 ms. But, as can be seen in Figure 2.2, the trap is not changing its shape for a long time into the ramp, until it opens into the guide potential within a few milliseconds. This indicates that adiabaticity is not given in the longitudinal direction, whereas it is maintained transversally, which means that there are no excitations spoiling the validity of the one-dimensional description. This sudden change of the longitudinal potential can thus be regarded as instantaneous in the models describing the expansion, using the static solution as the initial state at $t = 0$ in the final guide potential after the magnetic field ramp. Then the time evolution of the system can be calculated using the corresponding equations of motion, mapping this initial state to a time dependent state at the position of the fluorescence detector. This atom optics calculation is performed for thermal atoms (2.3.1) and for a BEC in the Thomas-Fermi limit (2.3.2). The flux in the detector is calculated by adding a centre-of-mass motion given by the guide potential gradient along the guiding wire (2.3.3) and reflection of atoms initially going into the direction opposite to the detector (2.3.4).

2.3.1. Expansion of a thermal atom cloud

For an ideal gas initially prepared in a static harmonic trap propagating along the magnetic waveguide, a scaling equation for the atomic flux can be found. Starting with the thermal line density distribution in the initial trap, described by Equation 2.6, it can be shown [26] that the flux at a distance z_d of atoms released from the trap at $z = 0$ is given by the rescaled initial density distribution

$$j(t) = v(t)n(z_d, t) = \frac{v(t)}{\sqrt{1+\omega^2 t^2}} n(\tilde{z}_d, t = 0) \tag{2.13}$$

times a time-dependent velocity

$$v(t) = \frac{z_d \omega^2 t^2}{t\left(1+\omega^2 t^2\right)} \tag{2.14}$$

and the rescaled spatial coordinate

$$\tilde{z} = \frac{z}{\sqrt{1+\omega^2 t^2}}. \tag{2.15}$$

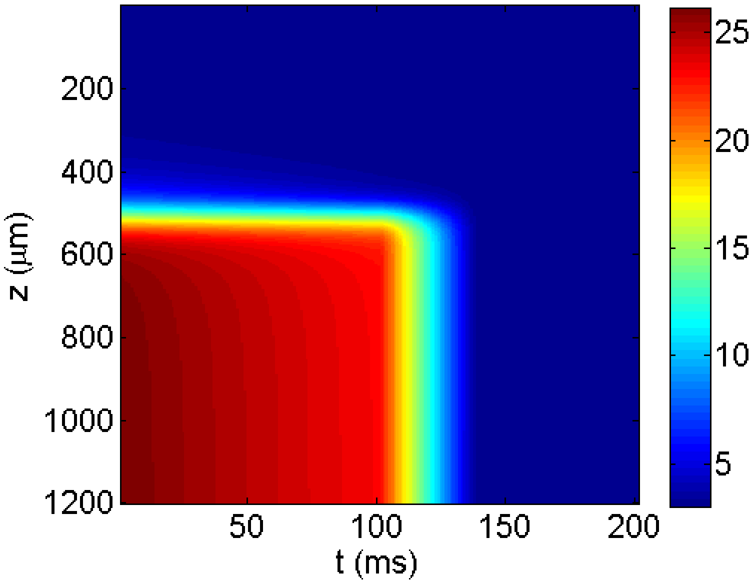

Figure 2.2.: Simulated ramp of the magnetic field from the initial trap into the magnetic wave guide. The colour scale gives the magnitude of the magnetic field in Gauss, $z = 0$ defines the centre of the initial trap. It can be seen that the trap stays almost unchanged for a long time, and then opens very rapidly along the guide direction situated at $z = 5500 \mu m$.

This scaling is possible due the fact that initially the atomic wave function is prepared in a harmonic potential. The flux then reads

$$j(t) = N\sqrt{\frac{m}{2\pi k_B T}} \frac{z_d \omega^3 t}{\left(1+\omega^2 t^2\right)^{3/2}} e^{-\frac{m\omega^2}{2k_B T}\frac{z_d^2}{1+\omega^2 t^2}}, \tag{2.16}$$

The timescale of propagation towards the fluorescence detector is fixed by the distance $z_d = 5.5$ mm between the initial trap position and the detection region, and by the initial trap frequency of $2\pi \times 3$ Hz. For these parameters the system is in the far-field regime defined by $\omega t \gg 1$. If this approximation is applied equation 2.16, the atomic flux distribution is

$$j(t) = N\sqrt{\frac{m}{2\pi k_B T}} \frac{z_d}{t^2} e^{-\frac{m z_d^2}{2k_B T t^2}}. \tag{2.17}$$

It is interesting to note that the information about the initial trap is completely lost and the flux is given solely by the Maxwell-Boltzmann velocity distribution of an initially free gas.

2.3.2. Expansion of a 1d BEC at T=0 in a waveguide potential

The time evolution of a 1d BEC is described by the time-dependent generalisation of the Gross-Pitaevskii equation 2.7

$$\left[-\frac{\hbar^2}{2m}\frac{\partial^2}{\partial z^2}+V(z,t)+g_{1d}|\Psi(z,t)|^2\right]\Psi(z)=i\hbar\frac{\partial\Psi(z,t)}{\partial t}. \tag{2.18}$$

For a useful description of the density and velocity distribution in the condensate, Equation 2.18 can be reformulated using the ansatz [53]

$$\Psi(z,t)=\sqrt{n(z,t)}e^{i\Phi(z,t)}, \tag{2.19}$$

and $v(z,t) := \frac{\hbar}{m}\partial/\partial z(\Phi(z,t))$. Applying this in Equation 2.18, and using the hydrodynamic approximation by neglecting the quantum pressure, leads to the two coupled equations

$$\frac{\partial n}{\partial t}+\frac{\partial}{\partial z}(nv)=0 \tag{2.20}$$

and

$$\frac{\partial v}{\partial t}+v\frac{\partial v}{\partial z}=-\frac{g_{1d}}{m}\frac{\partial n}{\partial z}. \tag{2.21}$$

Eq. 2.20 is the continuity equation (defining the atomic flux as $j(z,t)=n(z,t)v(z,t)$), and Equation 2.21 is the Euler equation for an ideal, irrotational liquid. Assuming that the hydrodynamic approximation remains valid during the whole propagation in the magnetic wave guide a self-similar ansatz [60] for the density distribution

$$n(z,t)=\frac{n_p}{b(t)}\left[1-\frac{z^2}{R^2(t)}\right]\Theta(R(t)-|z|), \tag{2.22}$$

can be made, where n_p is the initial peak density and $b(t)$ is the scaling parameter, defined by

$$R(t)=b(t)R_0. \tag{2.23}$$

Here R_0 is the initial Thomas-Fermi radius. At zero temperature the phase of the static condensate wave function is quadratic in the axial coordinate z and thus for the velocity field the scaling ansatz

$$v(z,t)=\frac{\dot{b}(t)}{b(t)}z \tag{2.24}$$

is made. If this ansatz is used in eqs. 2.20 and 2.21, a nonlinear equation

$$\ddot{b}(t)=\frac{\omega^2}{b^2(t)} \tag{2.25}$$

results for the scaling parameter can be derived which fully describes the dynamics of the system. This one-dimensional version of the Ermakov equation [18] can be solved numerically, as illustrated in Figure 2.3.

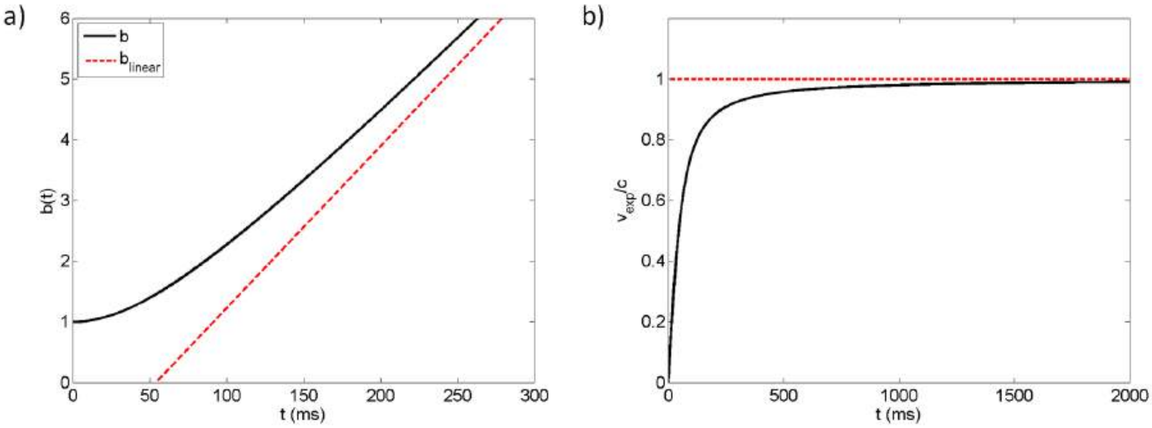

Figure 2.3.: Numerical solution of the Ermakov equation (2.25) for the scaling $b(t) = R(t)/R_0$ of the Thomas-Fermi radius $R(t)$ after releasing the trapped BEC with size R_0 into a longitudinally free potential at $t = 0$. **a)**: The radius first accelerates until after a time $t \approx 1/\omega$ the expansion reaches an almost constant rate, as indicated by a linearised version of b. **b)**: The expansion velocity of the cloud radius approximately converges asymptotically to the sound velocity c of the initial atomic ensemble in the trap centre.

After an initial acceleration phase of the time-dependent Thomas-Fermi radius $R(t)$, where most of the initial interaction energy is converted into kinetic energy, an almost constant expansion velocity is reached, which is the sound velocity of the atomic ensemble in the in the initial trap centre. Thus a linear approximation

$$b_{linear} = \sqrt{2}\,(\omega t - 1) \tag{2.26}$$

to the time-evolution of the scale parameter $b(t)$ seems evident. This linear description neglects the initial acceleration phase and accounts for the time delay by setting a new starting time $t = 1/\omega$ of the expansion from a point with vanishing radius. This is the atom optic equivalent of a geometric optics description of a magnifying glass, where a shifted virtual object in front of the lens can be assumed (see more on this equivalence in [2]). As discussed in Figure 2.4, the linear approximation seems to converge to the exact solution, but there is additionally a slowly increasing logarithmic term responsible for a small time-dependence of the slope which can be observed at timescales larger by orders of magnitude. Thus the error for experimentally relevant times is small.
The flux measured in the detector is the product of density and velocity distribution, defined by eqs. 2.22 and 2.24 evaluated at the position $z = z_d$

$$j(t) := j(z' = z_d, t) = n(z' = z_d, t)v(z' = z_d, t) \tag{2.27}$$

leading to the flux

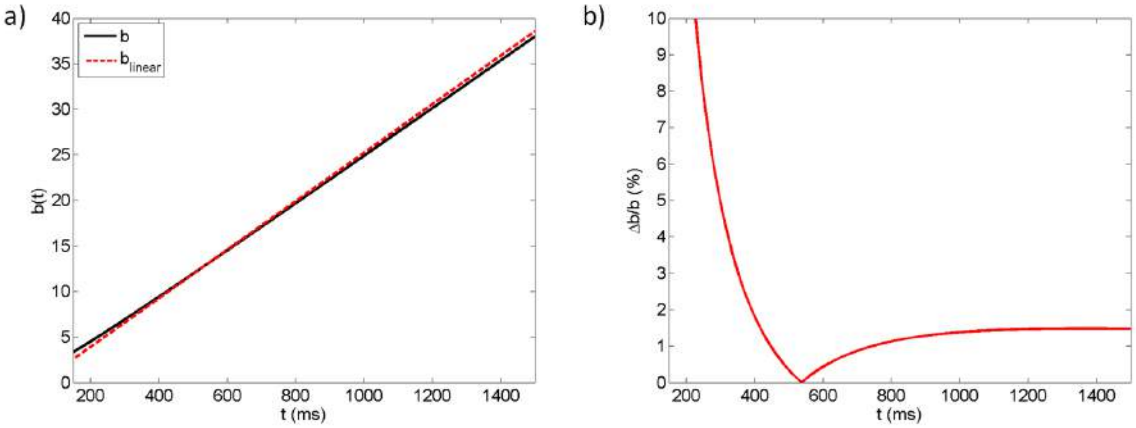

Figure 2.4.: a): Linear approximation b_{linear} compared to the numerical solution for $b(t)$ in the timescale of the fluorescence detector measurement and the evolution (**b)**) of the relative error $\Delta b/b = (b - b_{linear})/b$ between the two solutions. The linear approximation works well for this timescale, it accounts for the neglected acceleration phase by shifting the start time of the expansion to $t = 1/\omega$.

$$j^{TF}(t) = \frac{n_p}{b(t)}\left[1-\frac{z_d^2}{b^2(t)R_0^2}\right]\frac{\dot{b}(t)}{b(t)} z_d \Theta\left[b(t)R_0 - |z_d|\right] \tag{2.28}$$

2.3.3. Center-of-mass motion

So far only an expansion of the atom cloud driven by its interaction energy is taken into account. In order to include a centre-of-mass propagation along the wave guide due to a small axial gradient of its potential, a Galilei transform into the centre-of-mass system has to be performed:

$$z' = z - v_{cms}t \tag{2.29}$$

$$v' = v + v_{cms}. \tag{2.30}$$

After transforming into the moving frame, the cloud initially being at $z = 0$ and the fluorescence detector at position $z = z_d$, the flux for thermal atoms is:

$$j^{th}(t) = N\sqrt{\frac{m}{2\pi k_B T}}\frac{z_d}{t^2}e^{-\frac{m}{2k_B T}(\frac{z_d}{t}-v_{cms})^2}. \tag{2.31}$$

For $T = 0$ the density and velocity distribution read

$$n(t) = n(z'(z_d),t) = \frac{n_p}{b(t)}\left[1-\frac{(z_d - v_{cms}t)^2}{b^2(t)R_0^2}\right]\Theta\left[b(t)R_0 - |z_d - v_{cms}t|\right] \tag{2.32}$$

and

$$v(t) = v'(z'(z_d), t) = \frac{\dot{b}(t)}{b(t)}(z_d - v_{cms}t) + v_{cms}, \tag{2.33}$$

respectively. Thus the transformed atomic flux distribution becomes

$$j^{TF}(t) = \frac{n_p}{b(t)}\left[1 - \frac{(z_d - v_{cms}t)^2}{b^2(t)R_0^2}\right]\left[\frac{\dot{b}(t)}{b(t)}(z_d - v_{cms}t) + v_{cms}\right]\Theta\left[b(t)R_0 - |z_d - v_{cms}t|\right]. \tag{2.34}$$

2.3.4. Reflected part of the atom cloud

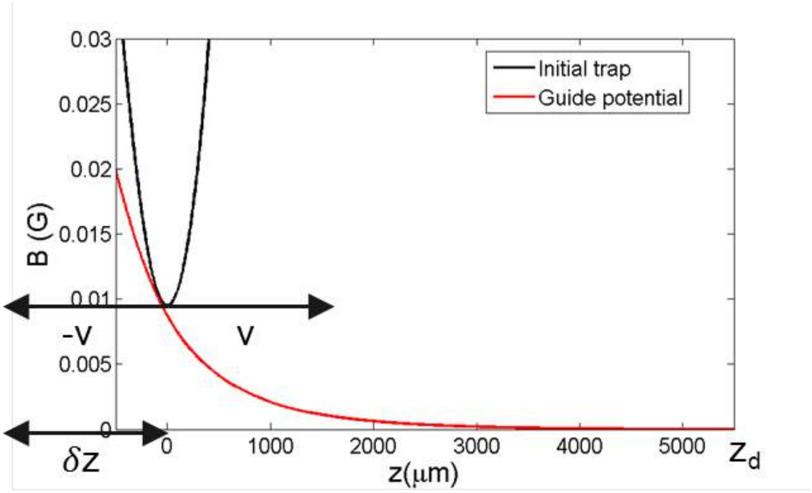

Figure 2.5.: Calculated potential for the initial static trap and the atomic wave guide. The atoms are quickly loaded into the new potential, half of them have an initial momentum pointing in the positive and the other half in the negative z-direction. While the former atoms propagate directly towards the detector at z_d, the latter ones have a longer trajectory by an amount of δz, the distance to their classical turning point and back to the centre of the initial trap. This leads to a second delayed peak arriving at the detector.

The discussion so far did not take into account the possibility of atoms having an initial momentum pointing away from the detector. These atoms first propagate into the other direction of the magnetic guide until they are reflected from the potential wall defined by the L-shape of the guide wire. After this detour of an effective path difference of δz, the atoms are accelerated towards the detector and behave similarly to the atoms going the direct path, only with a delay

$$j_r(z_d, t) = j(z_d + \delta z, t). \tag{2.35}$$

It is clear that for the reflected signal there must also be atoms trapped close to the detector. For thermal atoms this becomes

$$j_r^{th}(t) = N\sqrt{\frac{m}{2\pi k_B T}}\left[\frac{z_d}{t^2}e^{-\frac{m z_d^2}{2k_B T t^2}} + \frac{z_d+\delta z}{t^2}e^{-\frac{m(z_d+\delta z)^2}{2k_B T t^2}}\right] \tag{2.36}$$

and for $T = 0$ this is

$$j_r^{TF}(t) = \frac{n_p}{b(t)}\left[1 - \frac{(z_d+\delta z)^2}{b^2(t)R_0^2}\right]\left[\frac{\dot{b}(t)}{b(t)}(z_d+\delta z)\right]\Theta\left[b(t)R_0 - |z_d+\delta z|\right], \tag{2.37}$$

where the transformation to the centre-of-mass system is omitted for readability. The total solution is the sum of directly going and reflected atoms under Galilei transform, which is further discussed in the experimental section 7.2.

3. Atom-light coupling with integrated optics

The core of this thesis is the interaction of light fields, produced by integrated optics, with atoms. In the micro-optics experiment (part II) the atoms are excited by a tightly focused Gaussian beam from a tapered lensed fibre and the light scattered by the atom into 4π is partly coupled into a multimode fibre, its collection efficiency given by the solid angle covered by its end facet. This is an application of free space atom-light coupling discussed in section 3.2. A second application of this is the scattering of the transmitted light through the nanofibre waist with an atom. For this discussion the geometry of the light field in the nanofibre is introduced (3.1). Finally the field in a Fabry-Perot resonator and its coupling to atoms is discussed (3.3), which is necessary for the nanofibre cavity experiment (part III).

3.1. The nanofibre light field

In order to get an estimate for the order of magnitude of the mode area, an effective model for the intensity distribution of the light field outside the nanofibre is used and compared to the rather complicated analytical solution [38] for the evanescent field, which is a sum of Bessel functions. The effective model is an exponential decay

$$I(\rho, \phi) = I_0' e^{-\frac{\rho-a}{\Lambda}} \Phi(\varphi) \tag{3.1}$$

in radial direction with a decay constant Λ (see Figure 3.1), the waist radius a and, assuming linear polarised light, a sinusoidal dependence of the azimuthal angle φ, with its maxima at the direction of the initial polarisation plane. Thus, in general, the rotational symmetry of the light field is broken at the fibre waist. For the mode area it is enough to assume a mean intensity $I_0 = I_0'/2\pi \int \Phi(\varphi) d\varphi$ at the surface of the nanofibre. The total power of the light field can be calculated by integrating over the area

$$P = I_0 \int \rho d\rho d\varphi e^{-\frac{\rho-a}{\Lambda}} = 2\pi I_0 \int_a^\infty d\rho \rho e^{-\frac{\rho-a}{\Lambda}} = 2\pi I_0 \left(\Lambda^2 + a\Lambda\right). \tag{3.2}$$

The effective mode area can be defined via the surface intensity as

$$A_{eff} = \frac{P}{I_0} = 2\pi \left(\Lambda^2 + a\Lambda\right). \tag{3.3}$$

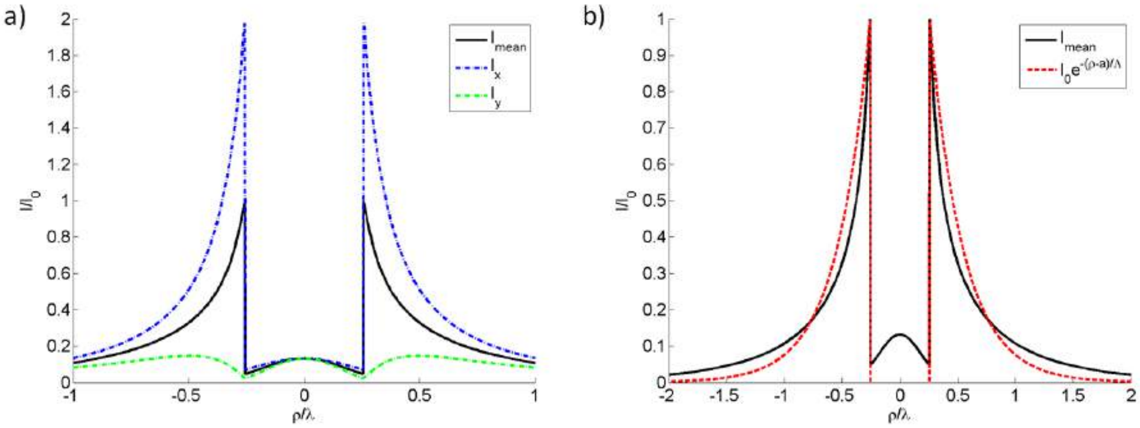

Figure 3.1.: a): Analytical solution of the intensity distribution of the nanofibre light field defined by the parameters of the experiment described in this thesis with a quasi-linear polarisation. The field is much stronger in the direction of the polarisation vector (in this plot chosen to be along the x-direction) than perpendicular to it. This sinusoidal behaviour on the azimuthal angle is averaged out when integrating over it, resulting in I_{mean}. Outside of the fibre $\approx 92.2\%$ of the total power are guided in an evanescent field. **b)**: For the discussion of the mode area, the decay of the radial field can be modelled by an exponential, with a decay constant $\Lambda/\lambda \approx 3.5$, leading to an effective mode area of $A_{eff} \approx \lambda^2$. This means the mean intensity on the fibre surface is $I_0 = P_{out}/\lambda^2$ with P_{out} being the total power in the evanescent field outside the nanofibre waist.

For the experiment a waist diameter of $a = \lambda/2 = 400$ nm is chosen because at this size the effective area is minimised [23] and the decay constant Λ is in the order of the wavelength λ. Thus the effective mode area can be estimated to

$$A_{eff} = \pi\lambda^2. \tag{3.4}$$

The confinement to such a small diameter is also possible with a free-space focused Gaussian beam, where the mode area is defined by the waist

$$A^G_{eff} = \pi\frac{w^2}{2}. \tag{3.5}$$

The smallest waist of focusing given by the Abbe limit [15] is also on the order of the light wavelength (at this point the paraxial approximation breaks down). Concerning the mode area there is thus no advantage of the nanofibre compared to a free-space beam. The difference lies in the axial length at which this confinement of the light field can be maintained. In the Gaussian beam this is restricted to the Rayleigh length $z_R = \pi w^2/\lambda$, whereas the mode guided by the nanofibre is confined to the small area over the whole thin part of the nanofibre, with a length of 5 mm in the case of this experiment, allowing emitters to couple strongly to it over the whole length, which results in high optical densities.

3.2. Free-space atom-light coupling

For small light intensities the atom-light coupling can be described by the oscillator model, treating the valence electron as a harmonic oscillator driven by the classical laser light field $E = E_0 e^{i(\omega t - kz)}$ with the equation of motion [15]

$$\ddot{x} + \Gamma \dot{x} + \omega_a^2 x = \frac{eE_{in}}{m}, \tag{3.6}$$

for the electronic oscillation amplitude x, with the atomic natural linewidth Γ and transition frequency ω_a, e and m being the electronic charge and mass respectively. This can be solved directly, choosing $z = 0$, in frequency space

$$\tilde{x}(\omega) = \frac{eE_0}{m} \frac{1}{\omega_a^2 - \omega^2 + i\Gamma\omega} \tag{3.7}$$

For light scattering the atomic polarizability α, defined via the induced atomic dipole moment d

$$d = e\tilde{x} = \alpha E_0, \tag{3.8}$$

is the defining property. For the oscillator model this is solved to

$$\alpha = 6\pi\varepsilon_0 c^3 \frac{\Gamma/\omega_a^2}{\omega_a^2 - \omega^2 - i\Gamma\omega_a^3/\omega^2}. \tag{3.9}$$

At large distances $r \gg \lambda$, near the optical axis, where $\sin\theta \approx 1$, the atomic radiation, being an oscillating dipole, has the behaviour of a spherical wave

$$E_a(r,\theta) = \frac{k^2 \sin\theta}{4\pi\varepsilon_0} \frac{e^{ikr}}{r} \alpha E \approx \frac{k^2}{4\pi\varepsilon_0} \frac{e^{ikr}}{r} \alpha E. \tag{3.10}$$

The total scattered power

$$P_{tot} = \frac{ck^4}{12\pi\varepsilon_0} |\alpha E|^2 \tag{3.11}$$

is given by the integral of $I_a(r,\theta) = \varepsilon_0 c |E_a|^2/2$ over the whole sphere. This can be compared to the scattering into a distinct mode E_M which is given by the geometric overlap integral [64] between the mode and the atomic spherical wave leading to a simple relation between the initial and the scattered field into this mode

$$E_M = i\beta E. \tag{3.12}$$

Here the complex coupling parameter β is proportional to the polarizability α and otherwise only depends on the geometry of the mode. This parameter becomes

$$\beta = \frac{\omega}{2c\varepsilon_0 A_{eff}} \alpha, \tag{3.13}$$

with the effective mode area A_{eff} defined in the previous section. The ratio between the scattered power into the mode $P_M = c\varepsilon_0 A_{eff}|E_M|^2/2$ and the total power from eq. 3.11

$$\frac{P_M}{P_{tot}} = 4C_1 \tag{3.14}$$

defines the free-space single atom cooperativity C_1. In order to obtain the light absorption by the atom the opposite process has to be described, the scattering of photons from a specific mode E_{in} into 4π, i.e. the amount of photons scattered away from an incident beam. The ratio of these powers

$$\frac{P_{4\pi}}{P_{in}} = \frac{P_{abs}}{P_{in}} = 2\,\mathrm{Im}(\beta) \tag{3.15}$$

is the absorption by one atom. In the rotating wave approximation β has the simple form

$$\beta = 2C_1(\mathcal{L}_a + i\mathcal{L}_d) \tag{3.16}$$

with the absorptive

$$\mathcal{L}_a = \frac{1}{1+\left(\frac{\Delta_{la}}{\gamma}\right)^2} \tag{3.17}$$

and the dispersive Lorentzian

$$\mathcal{L}_d = -\frac{\Delta_{la}}{\gamma}\frac{1}{1+\left(\frac{\Delta_{la}}{\gamma}\right)^2}, \tag{3.18}$$

respectively, and the light-atom detuning $\Delta_{la} = \omega_l - \omega_a$. With this, the ratio 3.15 becomes

$$\frac{P_{abs}}{P_{in}} = 4C_1\mathcal{L}_a(\Delta_{la}). \tag{3.19}$$

For N atoms coupling to the mode this can be integrated along the beam axis to be - on resonance -

$$\frac{P_{in} - P_{abs}}{P_{in}} = \exp(-4C_1 N) \tag{3.20}$$

for the transmission of an incident light beam. This is known as Beer's law [15], where the optical density can be recognised to be

$$OD = 4C_1 N = 4C_N, \tag{3.21}$$

defining the N-atom cooperativity C_N. This is the basis for absorption imaging.

3.3. Atom-light coupling in a cavity

After dealing with the coupling of light and atoms in free space, a similar calculation can be performed for the light field inside of a Fabry-Perot resonator. The properties of such a resonator are introduced (3.3.1) and then the change of the transmitted signal due to the presence of an atom in the light field is discussed, first using the classical oscillator model (3.3.2) and then by applying the Jaynes-Cummings model of cavity QED to weak optical fields (3.3.3).

3.3.1. The Fabry-Perot resonator

The electric field E_c inside a Fabry-Perot resonator, made of two mirrors with reflectivities r_1 and r_2, respectively and an internal transmittivity t_c per round trip , separated by a distance L, can be related to the incoming field E_{in} by summing the contributions of all round trips [62]. At first the there is the incoming field transmitted through the first mirror

$$E_0 = it_1 E_{in}, \tag{3.22}$$

where the mirror transmittivities are given by the lossless mirror condition $r_i^2 + t_i^2 = 1$. The field after n cavity round trips is

$$E_n = r_1 r_2 t_c e^{2ikL} E_{n-1} = \left(g_{rt} e^{2ikL}\right)^n E_0, \tag{3.23}$$

defining the resonant round trip gain $g_{rt} = r_1 r_2 t_c$. The sum of all contributions is a geometric series resulting in

$$E_c = \frac{it_1}{1 - g_{rt} e^{2ikL}} E_{in} \tag{3.24}$$

for the cavity field. This gives the electric field directly after mirror 1 with a wave vector pointing towards mirror 2. The field transmitted through the resonator is given by

$$E_{tr} = it_2 e^{ikL} E_c = -\frac{t_1 t_2}{\sqrt{r_1 r_2}} \frac{\sqrt{g_{rt}} e^{ikL}}{1 - g_{rt} e^{2ikL}} E_{in}. \tag{3.25}$$

The transmitted power spectrum $|E_{tr}/E_{in}|^2$ shows a comb of maxima for every resonance condition $kL = m\pi$ for all integer numbers m. Since the Finesse, being defined as the ratio of the cavity linewidth $\delta\nu_{FWHM} =: \kappa/\pi$ to the free spectral range $FSR = \frac{c}{2L}$, and related to the resonator parameters by

$$\mathcal{F} = \frac{\pi\sqrt{g_{rt}}}{1 - g_{rt}}, \tag{3.26}$$

is much larger than one, and it is possible to expand the round trip gain around one maximum. The expansion, also using $t_i \ll 1$ and $t_c \approx 1$,

$$g_{rt}e^{2ikL} \approx r_1 r_2 \left(1 + 2i\frac{\Delta_{cl}L}{c}\right) \approx 1 - t_1 t_2 + i t_1 t_2 \frac{\Delta_{cl}}{\kappa}, \tag{3.27}$$

introducing the light-cavity detuning $\Delta_{cl} = \omega_l - \omega_c$, yields

$$E_c = \frac{ie^{ikL}E_{in}}{t_1 t_2} \frac{1}{1 - i\frac{\Delta_{cl}}{\kappa}} \tag{3.28}$$

leading to the Lorentzian dependence

$$\frac{P_{tr}}{P_{in}} = \frac{1}{1 + \left(\frac{\Delta_{cl}}{\kappa}\right)^2} \tag{3.29}$$

of the ratio between transmitted $P_{tr} = \varepsilon_0 c A_{eff} t_2^2 |E_c|^2/2$ and incoming $P_{in} = \varepsilon_0 c A_{eff} |E_{in}|^2/2$ power.
Additionally the reflected field from the resonator

$$E_{ref} = r_1 E_{in} + i t_1 \frac{g_{rt}e^{2ikL}}{r_1} E_c = \frac{r_1^2 - g_{rt}e^{2ikL}}{r_1(1 - g_{rt}e^{2ikL})} E_{in} \tag{3.30}$$

is used to measure the mirror reflectivities, due to its asymmetry against a swap of the mirrors (see section 11.2).

3.3.2. An atom in a cavity - classical description

The combination of the electric field inside the cavity E_c and the field scattered by the atom is given by the sum for their sources [64]

$$E_c = \frac{1}{t_1 t_2} \frac{1}{1 - i\frac{\Delta_{cl}}{\kappa}} \left(i t_1 E_{in} + 2E_M\right), \tag{3.31}$$

the incoming field E_{in} and the field scattered into both directions of the mode E_M by the atom. Using relation 3.12, the latter field can be expressed by the incoming field, in this case the cavity field to $E_M = 2i\beta E_c$. The additional factor 2 comes from the standing wave inside the cavity, assuming the atom to be situated in the field maximum. The total field inside the cavity is thus

$$E_c = \frac{iE_{in}}{t_2} \frac{1}{1 - i\frac{\Delta_{cl}}{\kappa} - 4i\beta/t_1 t_2}. \tag{3.32}$$

Using β again in the rotating-wave approximation (eq. 3.16) the cavity transmission as a ratio of transmitted P_{tr} and incoming P_{in} power dependent on the laser-atom detuning and the laser-cavity detuning is

$$\left(\frac{P_{tr}}{P_{in}}\right) = \frac{1}{\left(1 + 2C\mathcal{L}_a(\Delta_{la})\right)^2 + \left(\frac{\Delta_{cl}}{\kappa} + 2C\mathcal{L}_d(\Delta_{la})\right)^2}, \tag{3.33}$$

with a cooparativity C increased by a factor $4/t_1 t_2 \approx 4\mathcal{F}/\pi$ compared to the coupling in free space.

3.3.3. An atom in a cavity - quantum description

Usually in cavity QED this relation is derived in the corresponding quantum description, using the Jaynes-Cummings model with the Hamilton operator

$$\hat{H}_{JC} = -\hbar\Delta_{la}\sigma^{+}\sigma^{-} - \hbar\Delta_{cl}a^{\dagger}a + \hbar g\left(a\sigma^{+} + a^{\dagger}\sigma^{-}\right), \tag{3.34}$$

with the respective atomic and photonic ladder operaters, σ^{+}, σ^{-} and $a^{\dagger}, a$ and a photon-atom coupling strength g. For the drive laser an additional term

$$\hat{H}_{d} = -i\hbar\eta\left(a - a^{\dagger}\right) \tag{3.35}$$

is introduced with the incoming photon rate η^2. Assuming a weak drive field [30], which couples only the first excited states $|0, e\rangle$ and $|1, g\rangle$ to the ground state $|0, g\rangle$ of the uncoupled eigenbasis, the Heisenberg equations of motion

$$\begin{aligned} \dot{a} &= i\Delta_{cl}a - ig\sigma^{-} - \kappa a + \eta && (3.36) \\ \dot{\sigma}^{-} &= i\Delta_{la}\sigma^{-} + ig\sigma_{z}a - \gamma\sigma^{-}, && (3.37) \end{aligned}$$

where the coupling to the vacuum is added via the terms containing κ and γ, a steady state with $\langle\dot{a}\rangle = \langle\dot{\sigma}^{-}\rangle = 0$ is formed. From the atoms being far from saturation follows $\langle\sigma_{z}a\rangle \approx -\langle a\rangle$. Thus one can directly find a system of equations

$$\begin{aligned} 0 &= i\Delta_{cl}\langle a\rangle - ig\langle\sigma^{-}\rangle - \kappa\langle a\rangle + \eta && (3.38) \\ 0 &= i\Delta_{la}\langle\sigma^{-}\rangle - ig\langle a\rangle - \gamma\langle\sigma^{-}\rangle && (3.39) \end{aligned}$$

for the expectation values of the ladder operators. From the weak field in the steady state the photon number operator factorises to $\langle\hat{n}\rangle = \langle a^{\dagger}a\rangle \approx \langle a^{\dagger}\rangle\langle a\rangle$. Solving eqs. 3.38, the classically derived equation 3.33 for the cavity transmission

$$\frac{\langle\hat{n}\rangle}{\eta^2}\kappa^2 = \frac{1}{\left(1 + 2C\mathcal{L}_a(\Delta_{la})\right)^2 + \left(\frac{\Delta_{cl}}{\kappa} + 2C\mathcal{L}_d(\Delta_{la})\right)^2} \tag{3.40}$$

is obtained, using the definition of the coupling strength $g^2 = 2\kappa\gamma C$.

Part II.

One-dimensional atom optics in a matter wave guide

4. Introduction to the micro-optics chip experiment

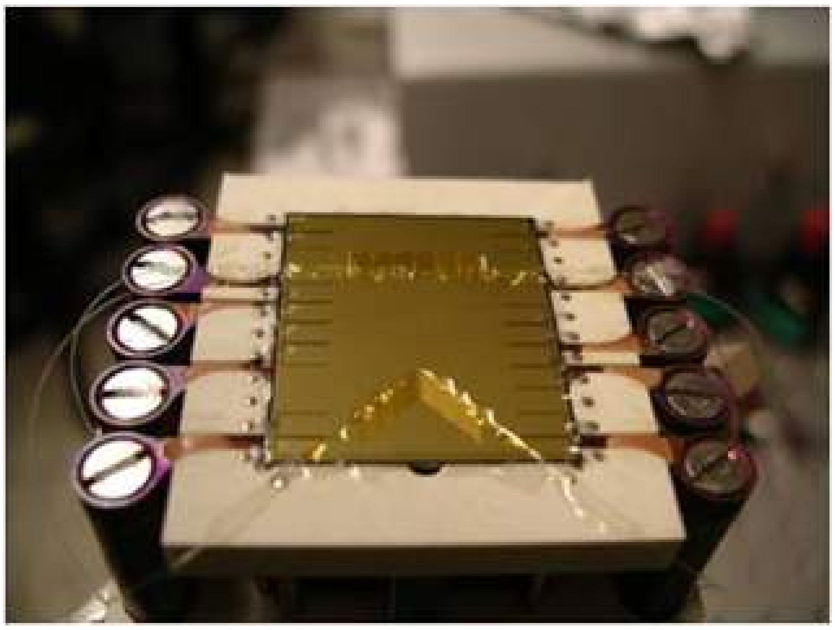

Figure 4.1.: Picture of the micro-optics chip experiment. The gold chip is acts as a mirror and in its centre microscopic trapping wires are situated. On top of the chip optical fibres are glued into holding structures. At the tip of the triangular shape, formed by two fibres, the fluorescence detector discussed in this thesis is traversed by a guiding wire transporting cold atoms from the central trapping region towards the detector. This chip is mounted on top of copper structures for large magnetic traps and on insulating ceramics (white) for good thermal conductivity to the outside of the vacuum chamber.

4.1. General introduction

The purpose of the micro-optics experiment was to act as a first test for integrated optics on an atom chip (a picture of it is given in figure 4.1), testing the advantages of large numerical apertures while maintaining a low optical background and good relative alignment of atom traps with optics. The fluorescence detector discussed in this thesis is a prototype for future experiments involving more sophisticated detection schemes with better controlled preparation of the detected atomic ensemble, making use of this powerful tool to gain knowledge about these coherent many-body systems from another perspective than it is possible with conventional imaging techniques. The main advantage of this detector is the direct access to the in-trap density distribution of a quasi one-dimensional atomic ensemble. This second part of the thesis is dedicated to first experiments with this detector and Bose-Einstein condensates (BECs). This part is organized as follows:

In this chapter the micro-optics experiment setup is described as well as the cooling and detection procedure for cold atoms.

Chapter 5 treats the dynamics of condensate atoms in the detector compared to thermal atoms. This is done by looking at the timescales in which the atoms interact with the detection light in 5.1, then by using a the detector in pulsed instead of continuous wave mode (5.2) and finally by imaging atomic ensembles scattered at non-resonant light in the detector (5.3).

In chapter 6 the signal strength of condensed atoms is determined and compared to that of warmer atoms.

Chapter 7 summarizes the results of this experiment and gives an outlook for future developments in the integration of micro-optics on an atom chip.

4.2. Experimental preparation of the atomic ensemble

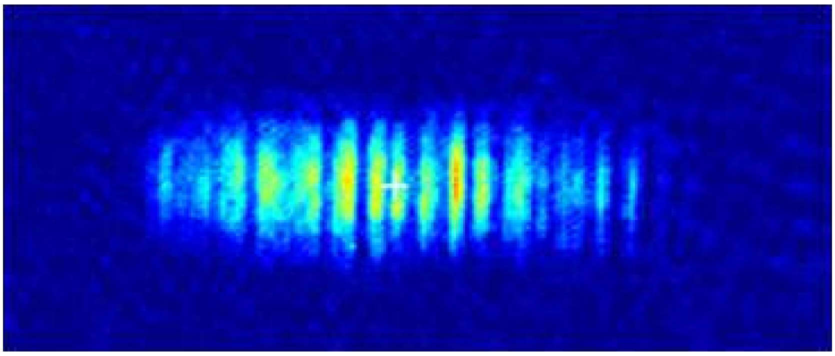

Figure 4.2.: Absorption image of a quasicondensate after 8 ms time-of-flight: The density distribution of ≈ 20000 atoms shows the characteristic ripple pattern of quasi one-dimensional condensates due to in situ phase fluctuations turned into density fluctuations in time-of-flight by self-interference. This ripple structure is used to estimate a temperature of ≈ 50 nK for the atomic ensemble.

Since the micro-optics atom chip experiment is well described in [32] and [70], only a brief description is given in the following.

The experimental cycle starts with the evaporation of Rubidium atoms in the vacuum chamber. There, a magneto-optical trap with Rubidium 87 atoms is formed in the crossing region of the cooling lasers and the centre of a magnetic quadrupole, which is formed by external coils in Helmholtz configuration in combination with a large current carried by a copper substructure behind the chip. This mirror MOT (see [68] and its discussion in chapter 9.2) is further cooled in an optical molasses, optically pumped into the $|F = 2, m_F = 2\rangle$ sub-state and loaded into a large magnetic trap also formed by a copper substructure. There the atoms are evaporatively pre-cooled before they are loaded into the chip trap.

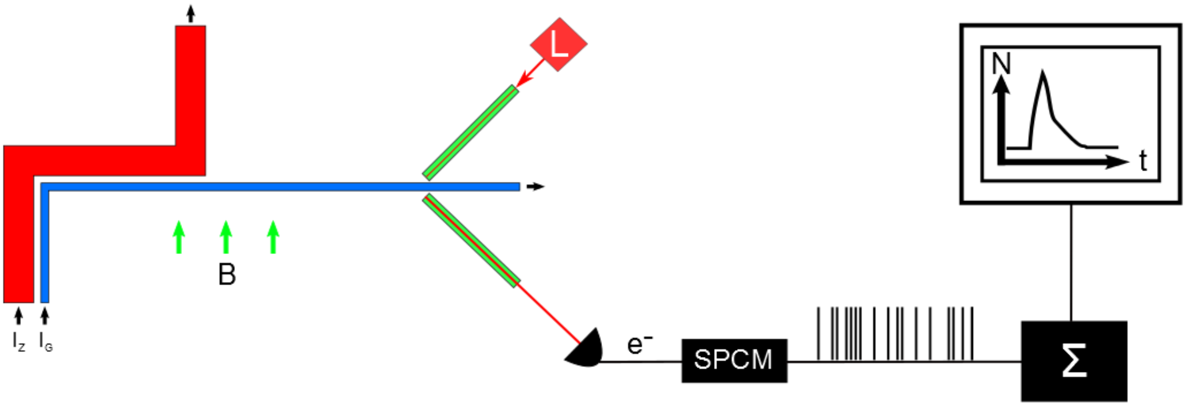

Figure 4.3.: Sketch of the geometry of the involved wires and the detection scheme. The Ioffe-Pritchard configuration of the magnetic trap is defined by a bias field B produced by external coils pointing in the direction of the arrows in combination with a current I_Z or I_G going through the wire along the corresponding arrows. The red Z-shaped wire is responsible for the initial trap were the cooling to the quasicondensate phase takes place. Such prepared atomic ensembles are loaded into the magnetic guide by decreasing the current through the Z-wire and ramping up the current through the L-shaped guiding wire. This wire provides a tight confinement in the perpendicular and a small gradient away from the L-corner along the current direction. The atoms are running along the magnetic guide for 5.5 mm towards the fluorescence detection fibres indicated by the green bars. The atoms are resonantly excited by the light focused onto the atoms by the tapered fibre and fluoresce into 4π. Some fluorescence photons are collected by a multimode fibre and guided outside the vacuum chamber and detected by an avalanche photo diode. The electronic signal is converted into digital time stamps and integrated by software to obtain a count distribution versus time.

The chip wires (see the sketch in Figure 4.3) needed for this thesis are the central chip-Z, a Z-shaped 200 μm wide gold wire and an L-shaped magnetic guide of 50 μm width. Both wires have an approximate height of ≈ 1 μm. Running a current through the Z-wire in combination with an external bias field perpendicular to the central bar of the Z, forms a magnetic trap in the central region of the atom chip with a strong confinement in both transversal directions and weak confinement in longitudinal direction with respect to the central bar, thus forming a needle-shaped trap. In this geometry the atoms are further cooled by evaporation to degeneracy, forming a quasi one-dimensional Bose-Einstein condensate. This quasicondensate regime [16, 9] is given if all energy scales are smaller than the transversal level spacing of the harmonic trap:

$$\mu, k_B T < \hbar\omega_\perp . \tag{4.1}$$

The phase fluctuations characteristic for quasicondensates [35], which translate into density fluctuations after a brief time of free expansion can be seen in Figure 4.2 for an atom cloud at a temperature of ≈ 50 nK determined by the distribution of these fluctuations

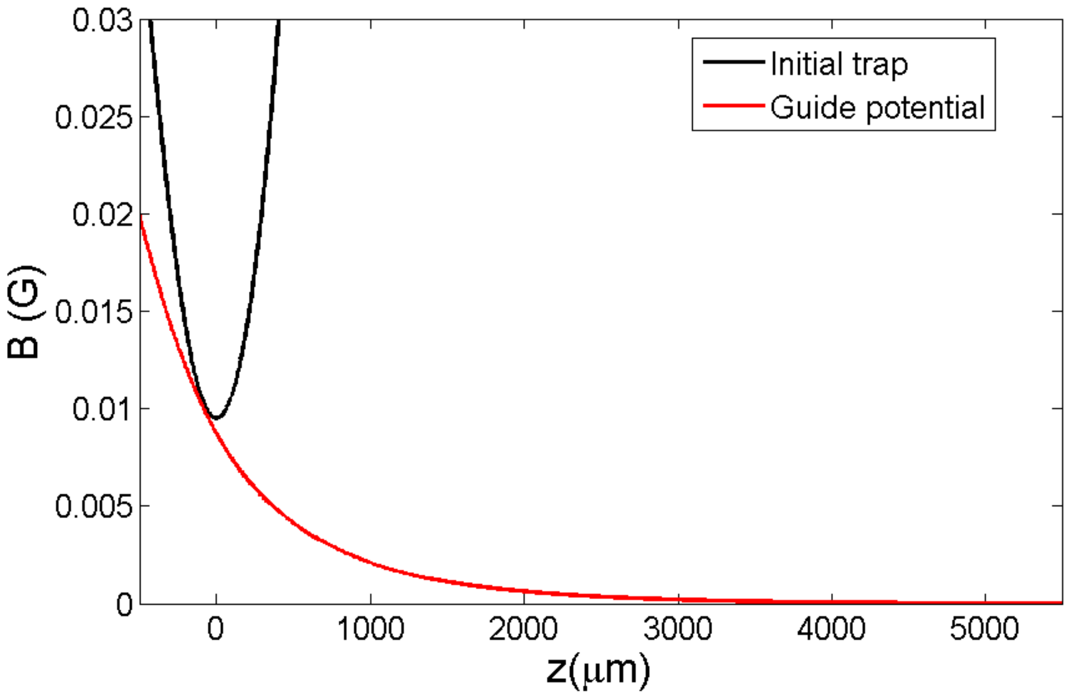

Figure 4.4.: Longitudinal part of the initial magnetic trap with a trapping frequency of $2\pi \times 3$ Hz and the final wave guide. The potential zero is defined as the field strength at the detector at $z = 5500$ μm. There the trap bottom is ~ 3 G.

(see [36] and [43] for a theoretical and an experimental description, respectively, of thermometry using these density ripples).

The quasicondensate is loaded into the L-shaped wire guide by appropriately changing the magnetic fields. The magnetic guide also provides tight transversal confinement but the trap is open in one longitudinal direction, while the L-shape closes the trap in the opposite direction. The latter is also responsible for a small potential gradient along the wave guide forcing the atoms to propagate towards the region of the fluorescence detector which is situated 5.5 mm from the Z-trap centre. The longitudinal part of the magnetic potential is plotted in Figure 4.4.

4.3. A single atom fluorescence detector for cold and ultra-cold atoms

Having arrived at the detection region, the atoms hit the focused laser beam resonant with the closed $F = 2 \rightarrow F' = 3$ transition. This excitation light is guided into the vacuum chamber by a fibre attached to the chip surface with lithographically patterned holding structures and focused by a taper at the tip of the fibre, as can be seen in a microscope image (Figure 4.5). The atoms in the waist of the beam scatter photons and

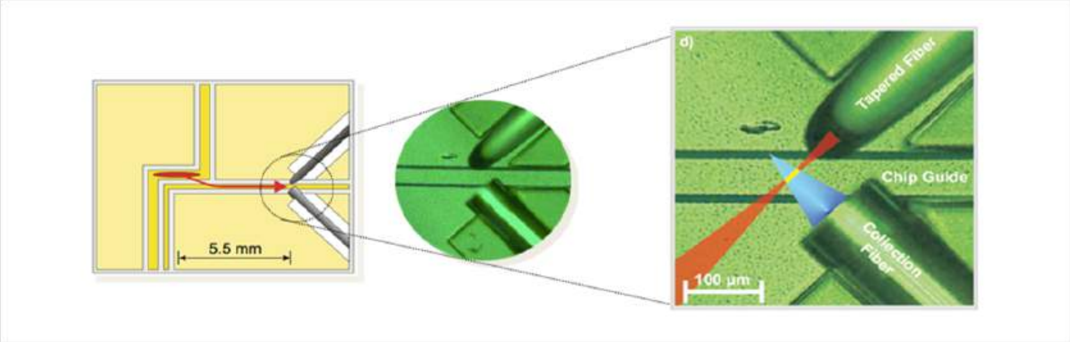

Figure 4.5.: Micro-optics atom chip design: a) Sketch of the wire geometry. The atoms are trapped in the central region of the Z-wire and then loaded into the L-shaped magnetic guide. The atoms propagate towards the triangular fluorescence detection region. b) A microscope picture of the actual chip. The guide wire in the centre runs through the two detection fibres which are held by epoxy structures next to them. c) In red the focused excitation beam is sketched, in blue the cone of maximum coupling efficiency of fluorescence light into the collection fibre defined by its NA.

some of the fluorescence photons are coupled into a multi-mode fibre fixed at a 90° angle with respect to the excitation fibre. This collection fibre guides the light outside of the chamber into a single photon counting module. This detector produces a set of photon click time stamps which can be integrated to obtain a distribution of photon counts per time bin. In order to learn more about the photon detection scheme, the reader is again referred to [32]. In the latter work the atoms are prepared differently than in this thesis, the difference is described as follows: Instead of initially loading the atoms into a large volume magnetic trap for evaporative pre-cooling, the atoms are directly loaded into the microscopic chip trap, where due to a worse mode matching to the transversally tight harmonic potential the atom cloud can only be prepared with relatively warm temperatures of $\approx 25\ \mu$K instead of ≈ 50 nK - or at best with temperatures at the crossover to degeneracy defined by

$$k_B T_d = \frac{\hbar^2 n^2}{2m}. \tag{4.2}$$

This difference is also manifest in the count distribution as can be seen in Figure 4.6, where atoms propagating to the detector are probed in continuous wave mode. The signal of the measurement without intermediate cooling step is completely different from that for ultra-cold atoms. The first one is well understood and has an overall photon detection efficiency of slightly above 1% of all scattered photons. Hence all the signal is directly proportional to the atomic flux hitting the detector. Its single peak distribution can be well related to a Maxwell-Boltzmann velocity distribution in the initial magnetic trap. The other two samples are measured in this thesis, where the RF-cooling [45] is stopped at two different values leading to two slightly different sample temperatures, both in the quasicondensate regime. Besides a large difference in absolute counts also the shape of the distribution looks much more complicated as can be best seen in the logarithmic plot in the inset. A major goal of this thesis is the explanation of this shape, which is again plotted in detail in Figure 4.7.

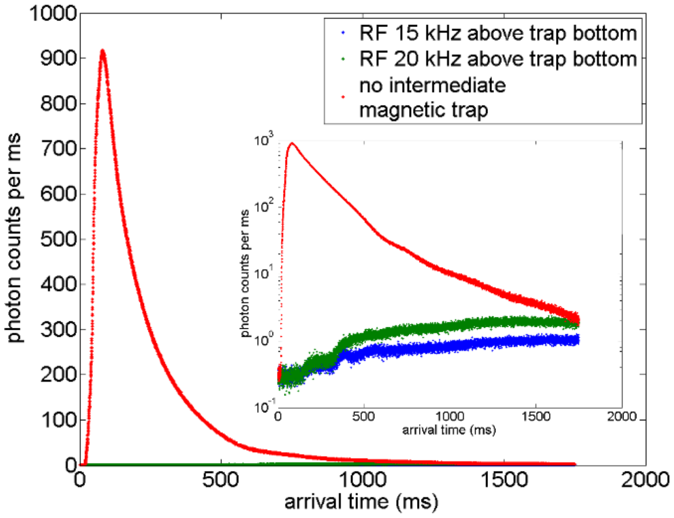

Figure 4.6.: Signal of thermal atoms (red) prepared without intermediate cooling step in a large magnetic trap compared to signals (blue and green) cooled to the quasicondensate phase. As can be seen in the inset logarithmic plot, the signals for ultra-cold atoms are completely different from the simple shape of the red curve.

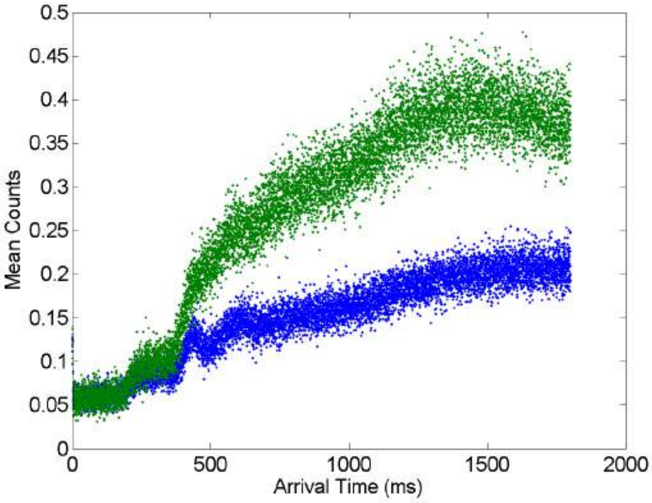

Figure 4.7.: Binned mean photon (bin size $\Delta t = 200\ \mu$s) counts versus arrival time in the fluorescence detector for two different temperatures given by RF-knives of 15 kHz (blue) and 20 kHz (green), respectively, above the trap bottom. The different features in the measured data are discussed in this part of the thesis.

5. Atom dynamics in the detection light field

It is important to understand at (least phenomenologically) the atom dynamics in the light field of the excitation fibre in order to be able to turn photon clicks into a measure for the atomic flux arriving at the fluorescence detector. First in section 5.1 the relevant timescales are introduced. Further information about these is obtained in section 5.2 by analysing pulses of the detection light, and finally the dynamics of atoms is imaged after their reflection at a non-resonant barrier, which gives more insight into the dynamics of ultra-cold atoms at the detector, as described in section 5.3.

5.1. Time interval distribution

There are three timescales involved with light-atom dynamics in the fluorescence detector, which can be well separated as they are of different orders of magnitude. The shortest timescale is given by the single photon interaction with an individual atom, i.e. the lifetime of the resonant atomic transition. Single atoms as single photon sources were demonstrated in this experiment with a Hanbury-Brown and Twiss type measurement [10]. The coincidence at two detectors showed very good anti-bunching behaviour with a rise time of 26 ns, the lifetime of the rubidium D2 transition, see [32],[34] and [31] for a detailed discussion. This thesis deals only with atom dynamics, which occurs over much larger times, where single photon dynamics is negligible.

The second timescale is defined by the interaction of an individual atom with many photons, following a trajectory similar to a random walk through phase space driven by the light field and the magnetic trap. This induces a time-dependent photon scattering rate and a geometry-dependent coupling efficiency into the collection fibre.

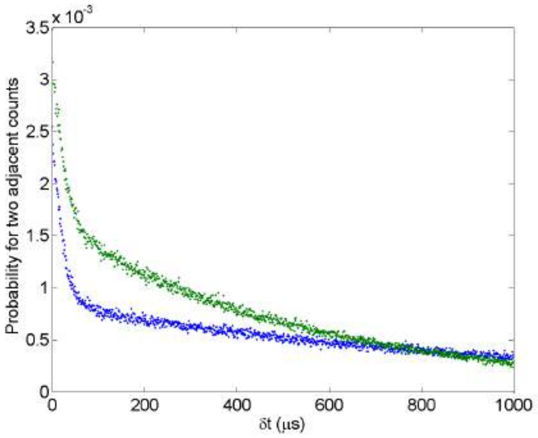

Figure 5.1.: Time interval distribution for two atomic samples with different temperature. This probability measure for time intervals is given by two exponential decays on two time scales defined by the interaction of an individual atom with the detection light on the short and the incoming flux of atoms into the detector on the long time scale

The longest timescale is given by the flux of incoming atoms along the guide wire, governed by atomic statistics solely.
The latter two timescales can be analysed with the measured probability distribution of temporally adjacent time intervals, whereas the single photon timescale is integrated out with an integration time of 500 ns. The time interval distribution is obtained by making a histogram of time intervals in the tail of late arrival times, where the atomic flux is small enough to guarantee a negligible probability of having two atoms in the same time bin and where the atom detection efficiency is constant (see chapter 6). This distribution is normalised by the total number of intervals, thus forming a frequentistic probability measure (see fig. 5.1). In the case of completely random photon scattering a Poissonian distribution can be assumed and the probability for a time interval τ_f to be empty is given by

$$p_\tau(0) = e^{-\langle n_{cts}\rangle \tau_f}, \tag{5.1}$$

where $\langle n_{cts}\rangle$ is the mean count rate. Then the probability to have a count after the time τ_f is

$$p_\tau(1) = e^{-\langle n_{cts}\rangle \tau_f}(1 - e^{-\langle n_{cts}\rangle}). \tag{5.2}$$

The natural logarithm of this,

$$\log(p_\tau(1)) = -\langle n_{cts}\rangle \tau_F + \log(1 - e^{-\langle n_{cts}\rangle}), \tag{5.3}$$

is a straight line whose slope is strictly the count rate. This explains the fast exponential decay of the time interval distribution, as shown in Figure 5.2. The slowly decaying tail of the distribution is given by the atomic arrival statistics and it is also exponential with the mean atom detection rate being the decay constant if the arrival time distribution is Poissonian. This is confirmed for all investigated temperatures, as a second straight line with the right slope can be fitted to the tail of the distribution with high confidence and the Poissonian nature of the atomic statistics is further supported by the analysis discussed in the chapters 6 and 7. These time interval distributions are measured for differently prepared atomic ensembles with temperatures defined by different end values of the final RF-cooling ramp, with an intermediate cooling step in a large magnetic and compared to a sample without this pre-cooling step. The mean interaction times, collected in Figure 5.3, defined by the fast decay, is always around 60 μs for the ultracold ensembles, whereas it is around 10 μs for samples without pre-cooling before the chip trap. Thus there is a different dynamics in these two regimes, which is further investigated with other methods described in the next sections. From this follows that the photon scattering for the pre-cooled samples is very low. Also the detection rates for individual atoms are very low, see Figure 5.4. This rate can be indirectly related to the detection efficiency which is reduced by a factor of 5 for the pre-cooled samples. The detection efficiency is best understood with the help of the variance analysis in section 6.1.

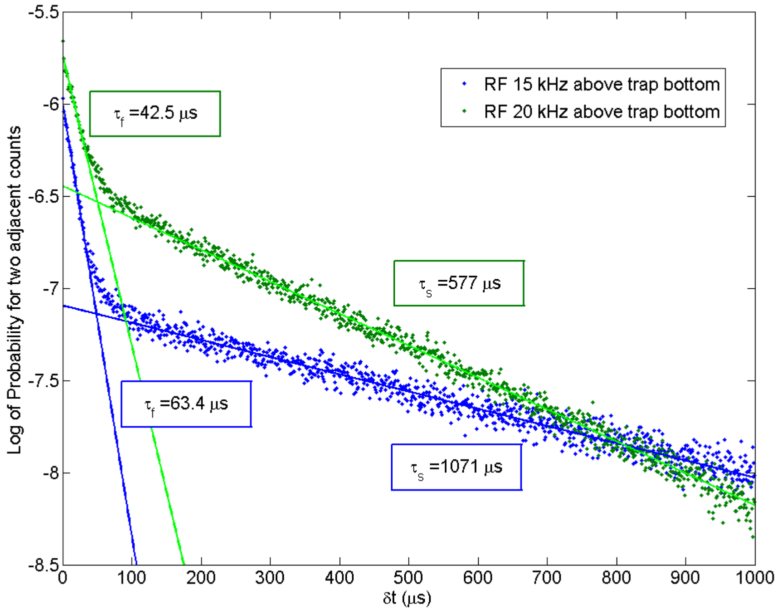

Figure 5.2.: Logarithmic plots of the time interval distribution for two atomic samples with different temperature. The fast slope is defined by the interaction time of individual atoms with the detection light, the slow slope is given by the rate of incoming atoms. Assuming that the arrival statistics of individual atoms is Poisson distributed the slope of the slow decay gives the mean time between neighbouring detected atoms.

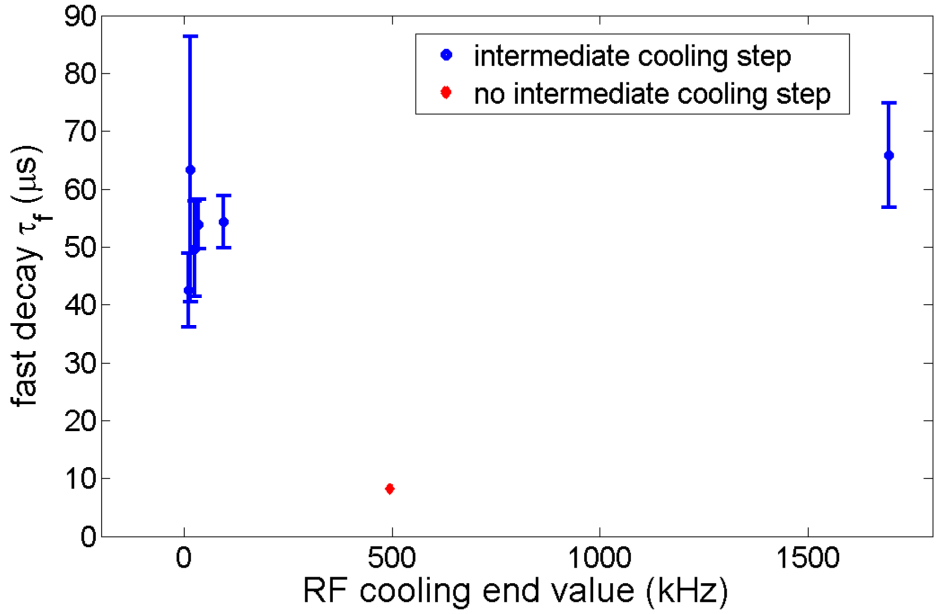

Figure 5.3.: Fast decay time of the time interval distribution versus the cooling knife in the chip trap. For cold atoms this decay is always around 50 μs. This defines the mean interaction time of individual atoms with the detection light. The error bars are defined by 95% confidence intervals of the linear fit of the logarithm. of the measured time interval distribution.

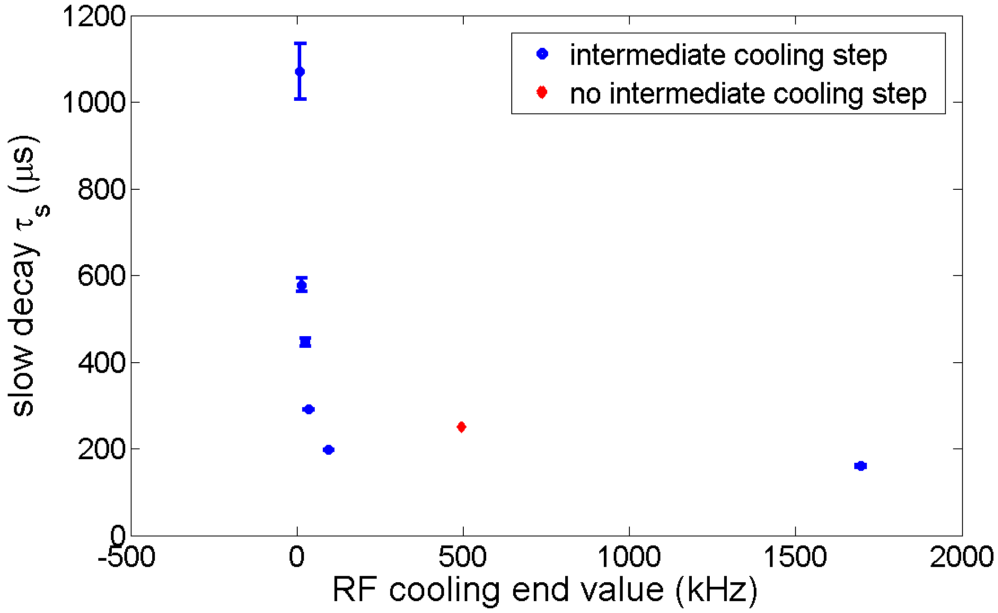

Figure 5.4.: Slow decay time of the time interval distribution versus the cooling knife frequency in the initial trap. This time of incoming atoms is given by the rate of detected atoms. The error bars are defined by 95% confidence interval of the linear fit of the logarithm of this data.

5.2. Pulsed measurement

So far the fluorescence detector has been driven in continuous-wave (cw) mode. In order to learn more about the atomic dynamics in the light field a pulsed mode is used. The atoms can move freely through the detection region until they are excited by a light pulse. By changing the pulse duration and rate information about the dynamics can be obtained.

5.2.1. Atomic response to a single pulse

The characteristic shape of the pulse shows an overshoot of detected counts in the first few tens of microseconds, corresponding to atoms already populating the detection region when the light pulse starts. These atoms are per time slice very similar in terms of their velocity and the detector is averaging over all possible atomic positions in the magnetic trap, thus they all undergo the same mean dynamics when the pulse hits them. The decay to the count rate plateau is given by the drop of these initial atoms out of the trap or their acceleration out of resonance due to their Doppler shift or the pumping into the dark $F = 1$ state.

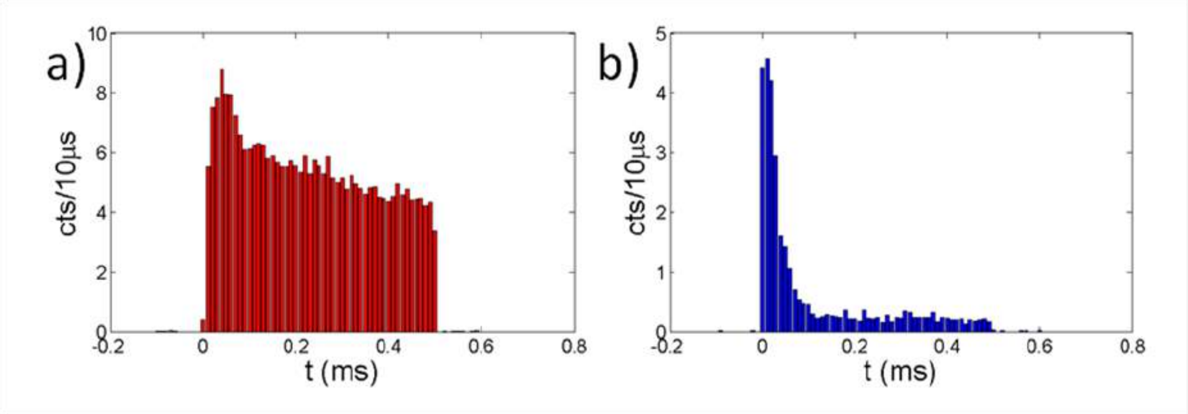

Figure 5.5.: Scattered photon counts versus time during a 500 μs pulse of the excitation light for a) thermal and b) ultra-cold atoms. The atoms saturate the detection region initially. When they are hit by the light pulse, they are pushed through resonance in the first tens of microseconds, producing the initial peak of scattered photons until a balance between resonant incoming and non-resonant outgoing atoms is reached after ≈ 500 μs. For cold atoms the signal drops more rapidly.

As can be seen in Figure 5.5 there is a different behaviour between atoms which are further cooled in the chip trap to a few hundred nanokelvin, and those where the evaporative cooling is stopped early in the initial large magnetic trap before loading into the chip trap. For the latter atoms at ≈ 20 μK a heuristic numerical explanation for the pulsed signal can be found. Before the light pulse, atoms populate the whole detection region, all of which have similar velocities and Zeeman shift. These initial atoms undergo

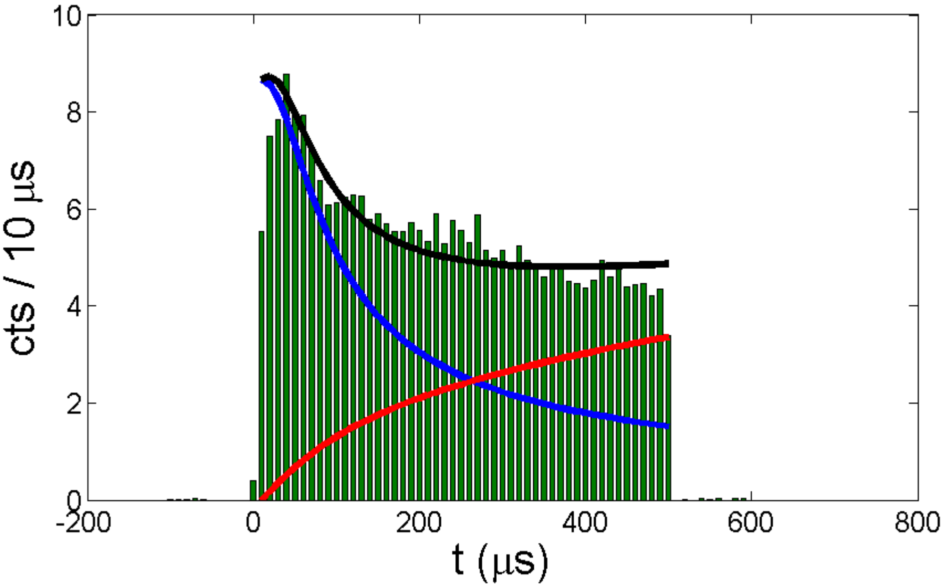

Figure 5.6.: Single pulse for thermal atoms at 20 μK: A numeric model can be used to heuristically explain the pulse for these atoms. The simulated scattered signal (blue) for atoms which populate the whole detection region with an initial velocity of 12 mm/s decays by Doppler shifts of the atomic resonance due to photon momentum transfer. During the pulse a constant flux of atoms comes in and undergoes the same scattering behaviour as the initial atoms. This increasing part (red) of the total scattering signal is given by the integral over atoms being in different stages of resonance. Note that also an outgoing flux of atoms equal to the ingoing one is assumed which is justified for a fast photon scattering rate. The cw scattering is reached after 0.5 ms.

a similar change of their scattering rate due to kicks from the excitation light photons. The atoms are first stopped and then accelerated into the opposite direction, and thus get more and more blue shifted with respect to the frequency of the excitation light. There is a static incoming and outgoing flux of atoms which are assumed to be equal for the calculation, which is justified as long as the detuning out of resonance is fast compared to the lifetime of the atom in the detection region. The incoming atoms have the same time dependence of the scattering rate as the initial atoms thus in every time bin there are atoms of every scattering rate depending on their lifetime in the detection region. This mean scattering rate is dominant after the initial atoms are completely out of resonance after $\approx 500\ \mu$s, and this is the rate of the continuous wave mode. This behaviour can be numerically described and gives a good estimation of the pulse shape for the warm sample, see Figure 5.6.

For the ultra-cold samples no such estimation fits their fast decay and their smaller plateau corresponding to the continuous wave mode. Thus another mechanism besides detuning due to photon kicks seems to be responsible for their time-dependence of photon scattering into the collection fibre. Simulations in [60] give some evidence that for atoms strongly confined in the magnetic guide, meaning they are transversally cold, the atoms are on average earlier repelled by the radiation pressure of the excitation fibre than transversally warmer atoms. Thus the acceleration due this force onto the atoms compared to its velocity is already large in a region where the coupling of fluorescence photons into the collection fibre is geometrically unfavourable. This leads to a smaller overall scattering rate of these cold samples, as was already observed with the time interval distribution in the previous chapter.

5.2.2. Pulse distance and atomic velocity

If the pulse distance in time is changed, a comparison between the height of the overshoot in the first and second pulse can be made. The time after which a revival of the full height is achieved corresponds to a full atomic passage time through the detection region. In figure 5.7, given the Gaussian profile of the light field, an error function is fitted to the pulse height ratio. From the full width of the error function a passage time of 556 ± 58 μs through the full waist of the focused detection beam is determined. Assuming as specified a waist of $\sqrt{2} \times 5$ μm, the factor $\sqrt{2}$ being due to the 45° angle between the excitation fibre and the atomic wave guide, a velocity can be estimated to 12.3 ± 1.25 mm/s for the atoms. This is consistent with the calculated acceleration of a single atom in the guide potential and also with the centre-of-mass velocities obtained by the analysis of the whole arrival signal in chapter 7. Also for several pulses with large enough distance an average ratio between the peak height and the cw count rate can be made. For thermal atoms the cw rate is (41.5 ± 0.6) % of the initial peak height, while for ultra-cold atoms it is only (6.3 ± 0.6) % both with 10 μs time bins. The ratio of initial peak height of the pulse and the cw height also results in a value for the average atomic penetration depth into the Gaussian light field of the detector of ≈ 1 μm.

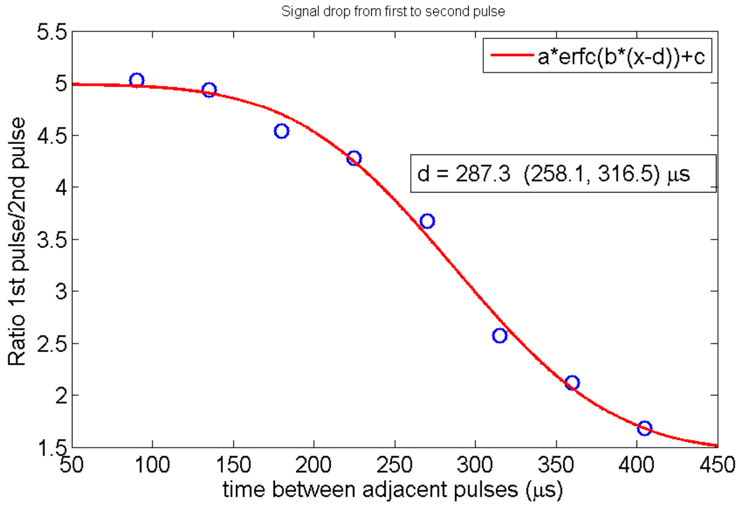

Figure 5.7.: Ratio of the initial peak of the detected counts of the pulsed light scattered by the atoms to the peak of the second pulse versus the distance in time between those two pulses. A ratio of 1 corresponds to a full passage of the atoms through the detection region. This ratio saturates at ≈ 5 for ultra-cold atoms. The fit is an error function because this is the integral of the number of scattering atoms in the Gaussian profile of the excitation beam. A half width of $287 \pm 29 \mu s$ is found.

As a conclusion it can be stated that the dynamics for thermal atoms, which have a weak transversal confinement, can be understood at least qualitatively, whereas for atoms subject to at least some evaporative cooling into the radially tight chip trap no straightforward explanation for their behaviour in the fluorescence detector could be found.

5.3. A dipole barrier for guided atoms

At the fluorescence detector the atoms, deeply trapped in the magnetic potential, seem to be repelled by the radiation pressure of the excitation light beam. This is describable as a location-dependent force on the atoms. In order to study the dynamics of these atoms scattering at this potential it would be advantageous to measure the density before and after the scattering with absorption imaging. But with resonant light the atoms scatter photons too rapidly and go dark with respect to the imaging laser, they are "detected away". The straightforward solution to this is the use of far detuned light instead and to make the assumption that this dispersive force on the atoms is geometrically comparable to the resonant force due to the local radiation pressure on the atoms. This can be justified because of the small size of the interaction region between light and atoms, which is only a fraction of the whole waist of the excitation light. The penetration depth into this light was measured with pulsed light to be on the order of 1 μm, (see sec. 5.2), which is comparable to the de Broglie wavelength of quasicondensate atoms. Thus the optical potential can be modelled as a step or even an infinite wall. This argument holds for both the resonant and the far-detuned case if the light in the latter case is blue-detuned with respect to the atomic transition. This blue detuned dipole potential can be used to investigate the scattering behaviour of the atoms in the vicinity of the detector on length scales much larger than the waist of the detection light with the help of usual absorption imaging ([63],[37]).

5.3.1. Experimental implementation

The resonant light through the excitation fibre is replaced by light coupled in from another laser source set close to the magic wavelength between the D1- and D2-transitions of rubidium. The overall light shift is then the sum of both contributions [27]

$$U_{dip}(\vec{r}) = \frac{\pi c^2 \Gamma}{2\omega_0} \left(\frac{2}{\Delta_{D2}} + \frac{1}{\Delta_{D1}} \right) I(\vec{r}), \tag{5.4}$$

where $\Delta_{D2} = \omega_L - \omega_{D2}$ and $\Delta_{D1} = \omega_L - \omega_{D1}$ are the detunings of the laser with respect to both transitions (see Figure 5.8) and $I(\vec{r})$ is the intensity distribution of the light beam. Due to the Gaussian shape of the beam, the intensity distribution

$$I(\vec{r}) = \frac{2P}{\pi w(z)} \exp\left(-2 \frac{r^2}{w^2(z)} \right) \tag{5.5}$$

and thus the shape of the optical potential can be estimated just by knowledge of the light power P coupled into the excitation fibre. In eq. 5.4 large detunings compared to the hyperfine splitting and linear polarised light are assumed. The former condition is guaranteed by the use of a far-detuned light source. The latter condition can be justified by the fact that for the resonant imaging laser, being prepared with linear polarisation before the coupling into the excitation fibre, scattering of the atoms has been measured to be on the same order of magnitude for the two Zeeman split cycling transitions $|F = 2, m_F = -2\rangle \longrightarrow |F = 3, m_F = -3\rangle$ and $|F = 2, m_F = 2\rangle \longrightarrow |F = 3, m_F = 3\rangle$, driven by σ_- and σ_+, respectively. Thus the polarisation of the dipole laser, with respect to a quantisation axis along the magnetic guide, is at least close to linear. At the crossing wavelength, which has been measured [5] to be 790.034(7) nm in vacuum the contributions of both light shifts cancel and the light force is zero in the dipole approximation. Going to larger wavelengths thus means having a positive light shift due to being blue detuned with respect to the D1-line and a weaker negative light shift due to the red detuning with respect ot the D2-line. The highest achievable stable set point for the laser diode in use[1] was at a wavelength of 793.35 nm, thus this was chosen to be the working point for the dipole barrier. Up to 200 μW light power could be coupled into the fibre, which corresponds to a central barrier height of $\approx k_B \times 100\ \mu$K. By using an acousto-optic modulator the trap height could be modified up to this bound.

5.3.2. 1d dynamics of the atomic flux at the barrier

In order to study the dynamics of the atomic distribution in the region of the dipole barrier, absorption images are taken from the side perpendicular to the magnetic wave guide for 20 ms-steps in atomic propagation time in this guide. This measurement of the atomic density distribution, performed in time-of-flight 6 ms after switching off all magnetic fields, is done with and without dipole barrier (Figure 5.9) and the results are compared. The difference between these distributions is given by the density of the reflected part of the atom cloud at the high potential wall and the vanishing density after it.

The time evolution of the atomic line density $n(z, t)$ along the wave guide was studied. Independent of its state the atomic ensemble has to obey a continuity equation:

$$j(z, t) = j_{in}(z, t) \tag{5.6}$$

with $j_{in}(z, t)$ being the ingoing and $j(z, t)$ the outgoing atom current at a surface perpendicular to the wave guide at a certain position z. For both an ideal gas and a (quasi-) condensate this trivial form of Kirchhoff's rule can be expressed by the line densities and velocities as

$$j(z, t) = n(z, t)v(z, t) = n_{in}(z, t)v_0(z, t) = j_{in}(z, t). \tag{5.7}$$

The incoming atomic density n_{in} is measured and the centre-of-mass velocity of 12 mm/s was already determined by the pulsed detector measurement (see section 5.2). The

---

[1] Roithner Lasertechnik: RLT790-80MGS1

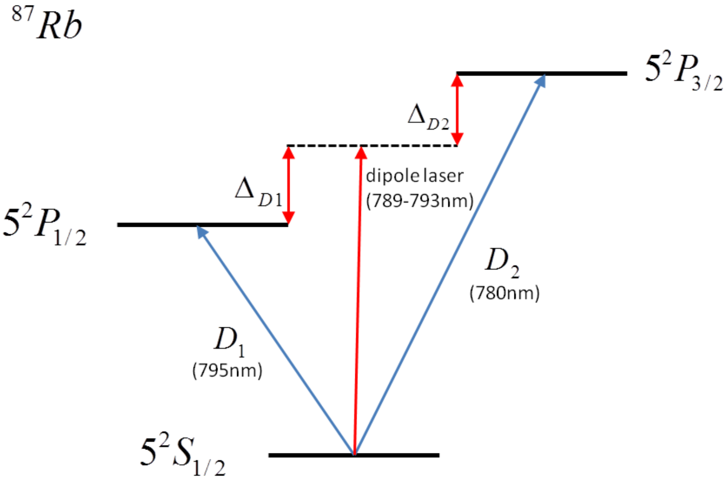

Figure 5.8.: Level scheme of the rubidium fine-structure. The light shifts due to a dispersive coupling to the two excited states with $J = 1/2$ (D1) and $J = 3/2$ (D2) cancel at a wavelength of ≈ 790 nm. The dipole laser wavelength is tunable around this threshold, thus allowing net light shifts of both positive and negative sign, corresponding to a repelling or attractive dipole force, respectively. In this thesis is only run at the maximum wavelength of ≈ 793 nm to provide a large potential barrier for the guided atoms.

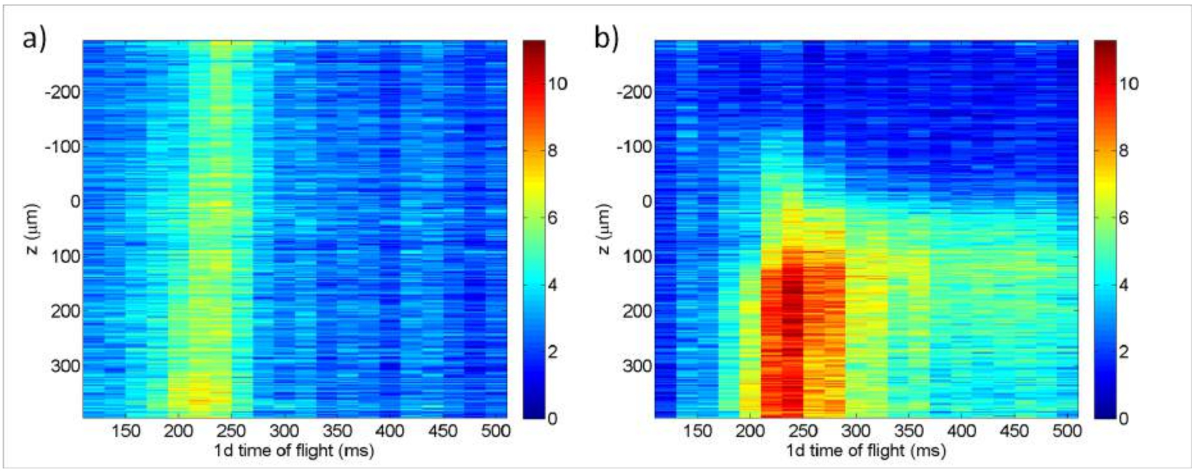

Figure 5.9.: Atomic line densities without (a) and with (b) dipole barrier along the magnetic guide coordinate, where $z = 0$ marks the estimated location of the dipole barrier, for different propagation times along the guide. The densities are calculated by absorption imaging after 6 ms time-of-flight.

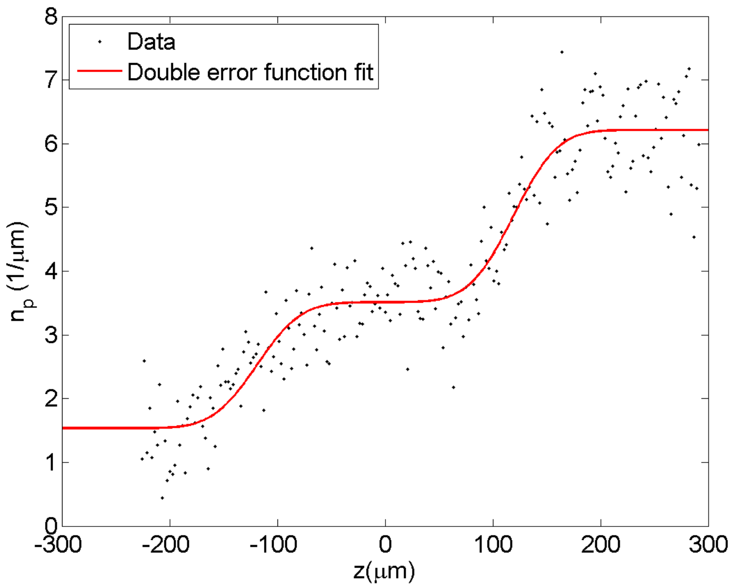

Figure 5.10.: Line density distribution in time-of-flight in the vicinity of the dipole barrier situated at $z = 0$. The double step is due to the centre-of-mass velocities of both ingoing and outgoing atoms. A sum of two error functions is fitted to the data and the relative velocities can be determined by their distance.

outgoing current has to be decomposed into a transmitted and a reflected part, j_{tr} and j_r, at the dipole barrier. In this measurement the height of the potential barrier is much larger than all atomic energies, thus the transmitted current can be set to zero and the above equation can be reduced to

$$v_r(z,t) = \frac{n_{in}(z,t)v_0(z,t)}{n_r(z,t)}. \tag{5.8}$$

If this were a true 1d problem the ingoing and outgoing velocity should be the same due to momentum conservation - and so should the densities. But since the dipole barrier is tilted by 45° with respect to the incoming atomic beam it seems natural that a large fraction of the initial momentum will be transferred to the transverse degrees of freedom. Due to this transverse excitation in the magnetic potential the density close to the barrier is increased as can be seen in Figure 5.9. The density distribution in time-of-flight has the shape of a double step symmetrically distributed with respect to the position of the barrier. This is due to the centre-of-mass velocity of the incoming beam and of the outgoing into the opposite direction. Thus, after a time-of-flight of $t_{tof} = 6$ ms, the two clouds are displaced by $\delta z = (v_0 + v_r)t_{tof}$, which is on the order of 120 μm for perfect reflection. In order to quantify this double step a sum, of two error functions

$$n_{tof} = n_{in}\,\mathrm{erf}\left(\frac{z - v_0 t_{tof}}{\delta v\, t_{tof}}\right) + n_r\,\mathrm{erf}\left(\frac{z + v_r t_{tof}}{\delta v\, t_{tof}}\right) \tag{5.9}$$

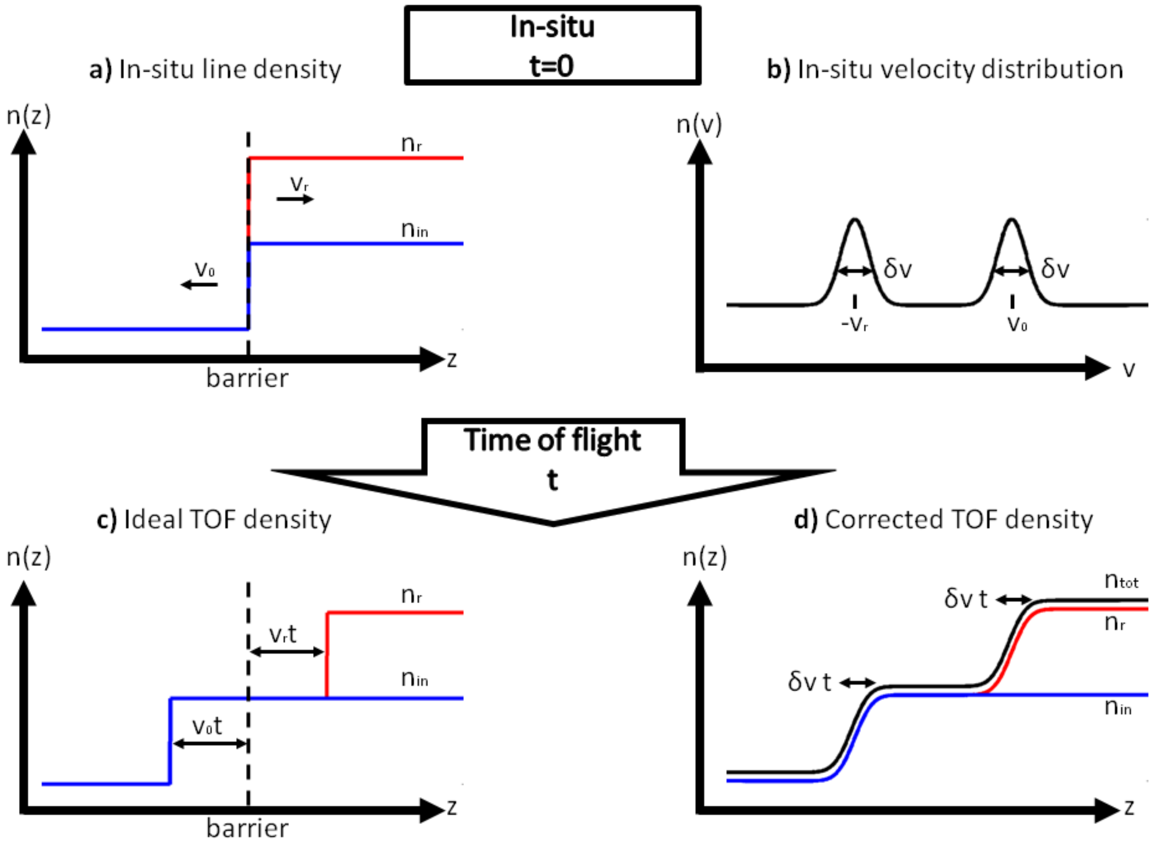

Figure 5.11.: Graphical explanation of the double error function behaviour of the line density distribution near the dipole barrier in time-of-flight. **a)** After some propagation time in the wave guide the atom cloud of density n_{in} is reflected at the barrier and a part of the initial cloud with density n_r is propagating into the opposite direction. **b)** There are then atoms with the mean velocity v_0 and reflected atoms with $-v_r$ yielding a velocity distribution around these mean values with a certain Gaussian uncertainty due to the position uncertainty in the initial chip trap. **c)** After releasing the atom cloud from the magnetic guide the incoming and reflected part of the cloud get separated by a distance $(v_0 + v_r)t$, where t is the time-of-flight and the density distribution for a cloud with vanishing velocity uncertainty is a double step. **d)** Including the velocity uncertainty one obtains a sum of two error functions with a width of $\delta v\, t$ for the time-of-flight density distribution.

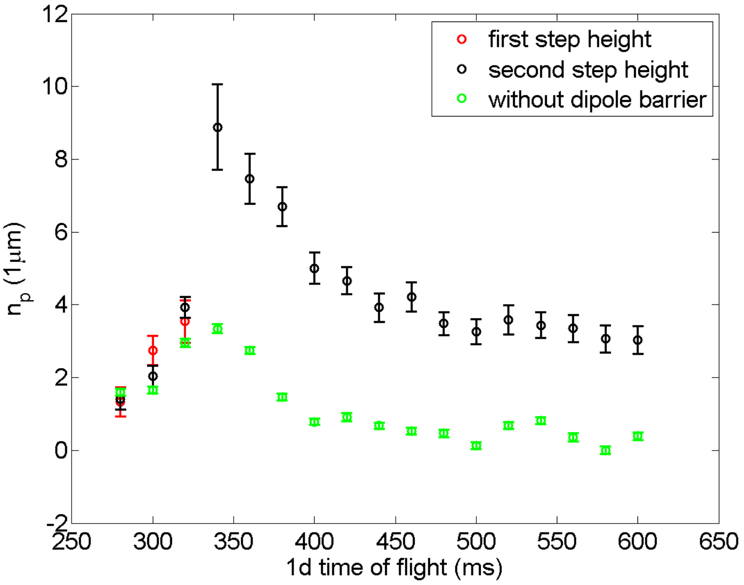

Figure 5.12.: Line densities at the position of the detector with and without dipole barrier. The density with dipole barrier is given by the amplitude of an (for the first three data points double) error function fit.

is fitted to the data as shown in Figure 5.10, which allows for a Gaussian velocity distribution around the centre-of-mass velocity (see an explanation for this signal shape in Figure 5.11). The heights of these steps give the densities of the incoming and the outgoing beam, respectively.

These can be compared to the density in a measurement without the dipole barrier for different propagation times or 1d time-of-flights (Figure 5.12) which can also be written as an effective reflectivity (Figure 5.13), defined as the ratio $R = n_r/n_{in}$. The latter being larger than one is caused by the fact that transversal dynamic is involved, quantifiable by using the measured densities and the centre-of-mass velocity for the incoming beam v_0 in eq. 5.8 and calculating the velocities v_r and $v_\perp := v_0 - v_r$ from this. The last relation is a consequence of momentum conservation.

As a result, one can analyse the dynamics of the incoming atom flux (Figure 5.14) and the reflected flux, from which the amount of momentum transferred to the transverse degree of freedom can be estimated (Figure 5.15). These results for the time evolution of the atomic momentum can be interpreted as follows: After an initial phase, where the atoms get reflected almost perfectly, see the first data points in Figure 5.13, an increasing fraction of atoms get excited transversally until finally around 80% of the initial longitudinal momentum is transformed into transversal potential energy. Qualitatively something similar seems to happen with resonant light in the fluorescence detection scheme (see a comparison of timescales between the dispersive and the radiation pressure barrier in chapter 7), where there is only a small net momentum towards the detector, leading to a low probability to enter the region of high coupling into the collection fibre,

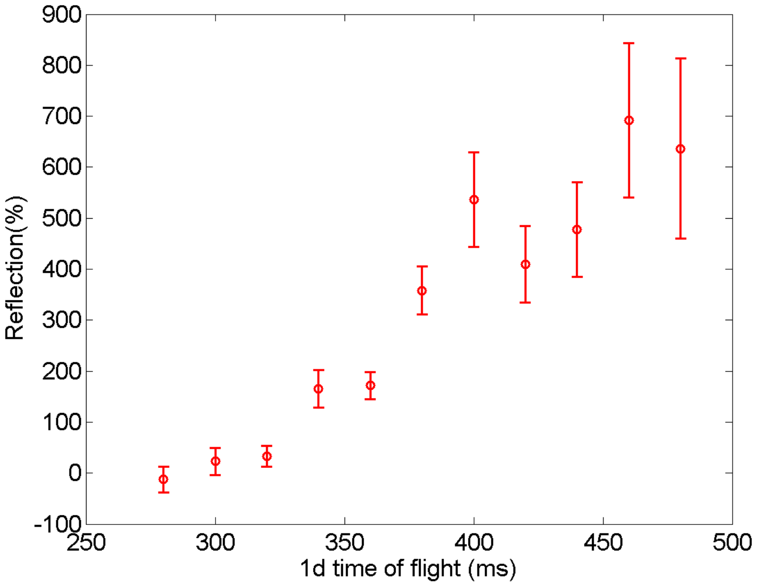

Figure 5.13.: Ratio between reflected and incoming line density at the position of the dipole barrier.

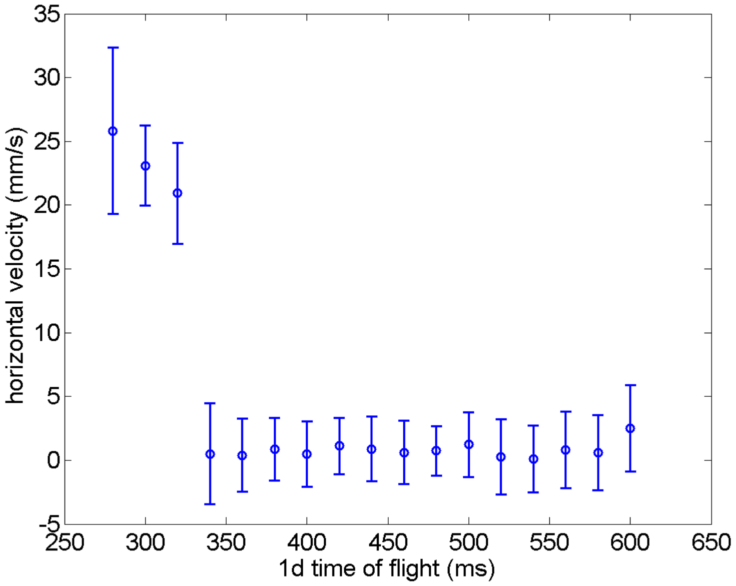

Figure 5.14.: Horizontal centre-of-mass velocity determined by the double error function fit of the horizontal density profile in the vicinity of the dipole barrier.

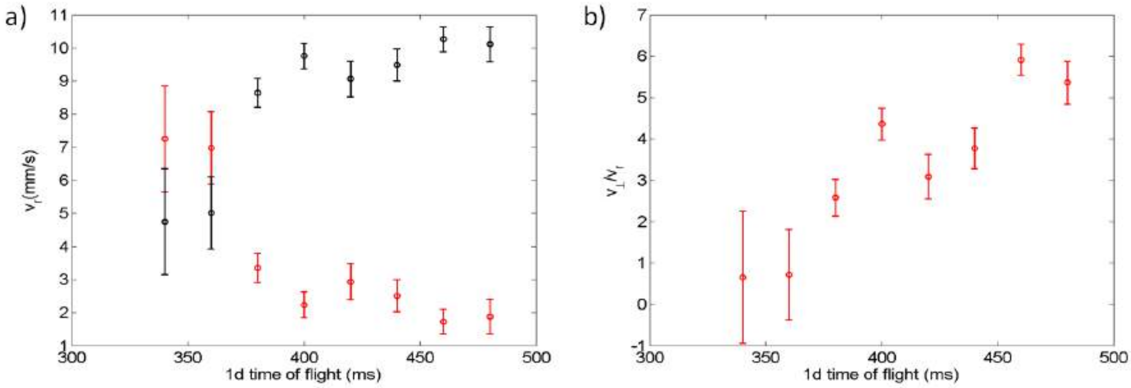

Figure 5.15.: **a)** The velocity of the reflected cloud v_r (red) and the transversal velocity $v_\perp$ (black) derived from the latter versus the 1d time of flight. After ≈ 400 ms most of the atomic momentum along the magnetic wave guide is transformed into transversal excitations. **b)** Ratio of the velocities of the reflected cloud v_r (red) and the transversal $v_\perp$ (black) derived from the latter versus the 1d time of flight. This is measure for the ratio of transverse energy and longitudinal kinetic energy. The former results in an increased density close to the barrier and the latter in the atoms being reflected by the barrier. Since this ratio gets larger than 1, this means more and more atoms are trapped near the barrier.

although the quantitative agreement of the factor of 5 for the signal strengths of the fluorescence detector and the momenta at the dipole barrier is probably a coincidence.

5.3.3. Transverse dynamics

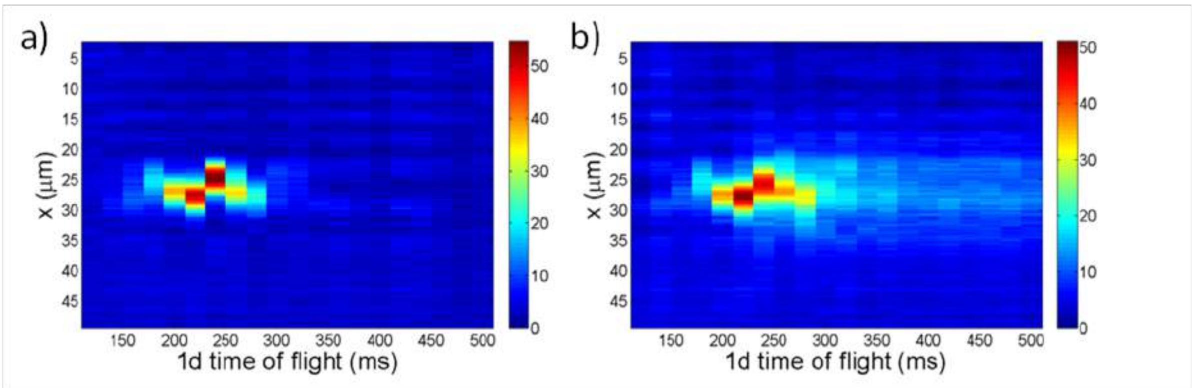

Figure 5.16.: Line density distribution perpendicular to the magnetic guide for the same times as in the other coordinate with the dipole barrier off **a)** and on **b)**.

So far the atomic density distribution was only analysed along the direction of the magnetic wave guide. The analysis of the transverse density profile perpendicular to the guide further supports the findings with the 1d description. A Gaussian can be fitted to

the transversal density profiles integrated along the direction of the magnetic wave as shown in Figure 5.16 for the profile with a dipole barrier, and for atoms passing through the detection region undisturbed. In order to gain more information about the behaviour in the vicinity of the dipole barrier, a transversal fit is performed at all positions along the magnetic wave guide. This allows an estimation of what happens in the direction along the imaging axis, meaning perpendicular to the imaging plane. This is necessary because the 45°-geometry can introduce significant atom dynamics in this direction. Some physically reasonable assumptions have to be made though. The estimation for the amplitude and width of the cloud in this invisible direction is as follows:
The atomic density distribution can be written as

$$n(\vec{r}) = \frac{n(z)}{2\pi\sigma_x\sigma_y} e^{-\frac{x^2}{2\sigma_x^2}-\frac{y^2}{2\sigma_y^2}}, \tag{5.10}$$

where care has been taken that it is normalized with respect to the line density along the z-coordinate

$$\int n(\vec{r}) dx dy = n(z). \tag{5.11}$$

The remaining two-dimensional Gaussian distribution can be probed only in one direction (in this chapter this is chosen to be the x-coordinate), the other direction is always optically integrated away, so that

$$n(x,z) = \int n(\vec{r}) dy = \frac{n(z)}{\sqrt{2\pi}\sigma_x} e^{-\frac{x^2}{2\sigma_x^2}} \tag{5.12}$$

where no information about the y-direction is left. The distribution $n_{in}(x,z)$ is measured for the case without dipole barrier as a reference for the measurement of the distribution $n(x,z)$ with dipole barrier. A few assumptions have to be made: Firstly the density distribution is a assumed to be isotropic in the two transversal direction, which is very well fulfilled due to the small gradient along z. Since the magnetic trap is much wider in the direction along the wave guide compared to the radial degree of freedom, the partial derivative with respect to z can be neglected in Maxwell's equation,

$$\frac{\partial B_x}{\partial x} + \frac{\partial B_y}{\partial y} + \frac{\partial B_z}{\partial z} \approx \frac{\partial B_x}{\partial x} + \frac{\partial B_y}{\partial y} = 0, \tag{5.13}$$

and equal slopes

$$|\frac{\partial B_x}{\partial x}| \approx |\frac{\partial B_y}{\partial y}| \tag{5.14}$$

are obtained in the two transverse directions, therefore yielding equal harmonic potentials. This approximation is fulfilled on the order of one percent. So, for a density distribution without dipole barrier, the isotropic description

$$n_{in}(\vec{r}) = \frac{n_{in}(z)}{2\pi\sigma_\rho^2} e^{-\frac{\rho^2}{2\sigma_\rho^2}} \tag{5.15}$$

is introduced, where $\rho^2 = x^2 + y^2$ and $\sigma_\rho = \sigma_y = \sigma_x$. Thus for the case without a symmetry-breaking dipole barrier the distribution is known. The second assumption is much stronger and will only be valid in the early stages after the reflection at the dipole barrier, and this is the claim of a conserved 3d-density at the origin before and after the reflection, or equivalently the claim that there is an equal density

$$n(0,0,z) = n_{in}(0,0,z) \tag{5.16}$$

with and without dipole barrier. The same assumption is made for incompressible liquids rather than dilute gases, but it can be argued that by momentum conservation the large initial velocity in z-direction is transferred into high transverse momenta after reflection and the atoms thus occupy completely different positions in (phase-) space: the gas initially covers more volume instead of being compressed. If the definitions 5.10 and 5.15 for the densities evaluated at the origin are used in eq. 5.16, the relation

$$\frac{n(z)}{\sigma_x \sigma_y} = \frac{n_{in}(z)}{\sigma_\rho^2} \tag{5.17}$$

is obtained. Thus there is a way to express the width of the unmeasurable density distribution

$$\sigma_x = \frac{n(z)}{n_{in}(z)} \frac{\sigma_\rho^2}{\sigma_y} \tag{5.18}$$

by measurable observables only. From the Gaussian fit one can derive the time evolution of the peak density and width of the atom cloud perpendicular to the chip surface. One can directly compare these two parameters to those measured without dipole barrier, as is illustrated in Figure 5.17. The peak densities are almost equal for some time, until the cloud gets denser next to the dipole barrier compared to the incoming one, indicating that the atoms are trapped for a while near the barrier. The evolution of the width seems to explain why it takes some time before the density rises. The width increases steadily due to the barrier, indicating some dynamics perpendicular to the chip surface, i.e. some deviation from the ideal case of a planar geometry of the problem. From these properties perpendicular to the chip it is now possible to estimate the behaviour of the atom cloud, in the plane of both dipole barrier and magnetic wave guide using eq. 5.18. The results given in Figure 5.18 show that the transverse width in the plane parallel to the chip surface, σ_x, increases to larger values than in the case without dipole barrier, giving indirect evidence that a potential shaped by the tapered lensed fibre induces transverse excitations, as already found in the previous section.

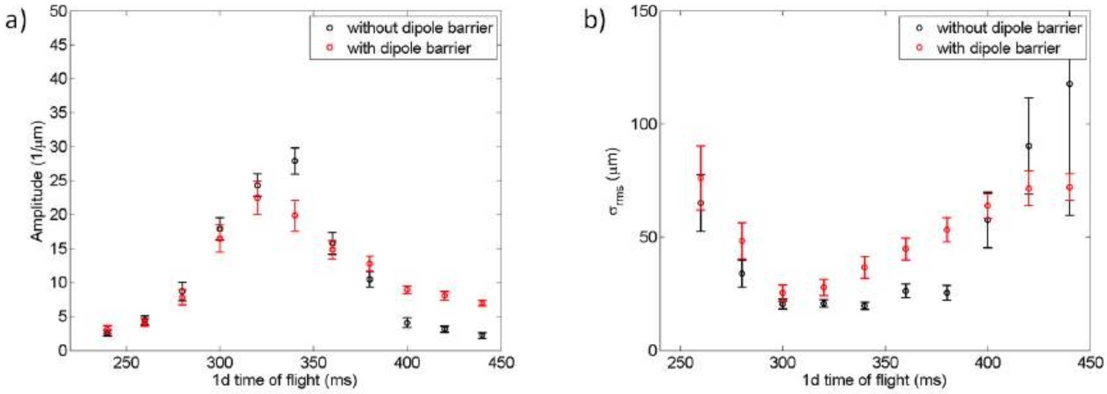

Figure 5.17.: Parameters obtained from the transverse Gaussian fit of the integrated profile along the magnetic guide with and without a dipole barrier. **a)** Peak density Amplitude of the Gaussian profile. **b)** Root mean squared width of the Gaussian

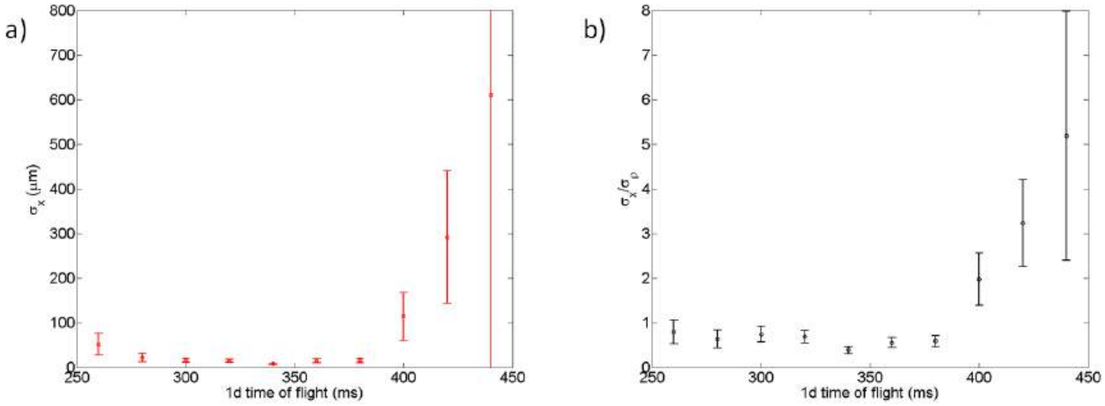

Figure 5.18.: Evolution of the "hidden" transverse width σ_x of the atom cloud parallel to the chip surface (**a)**) and its ratio to the incoming width measured without dipole barrier (**b)**), derived from the results shown in Figure 5.15 from eq. 5.18. After an initial phase of almost constant transverse width, it grows, which is an evidence for transverse excitations due to the barrier.

6. Signal strength for guided ultra-cold atoms

After the discussion of the atomic dynamics in the fluorescence detector in the previous chapter, the count statistics can be used to convert the count distribution into a measure of the incoming atomic flux and thus it is possible to completely forget about the photon statistics. In order to arrive at this measure for the mean atomic flux, every information about deviations from the mean, such as second order correlations, is sacrificed to obtain the signal strength.

6.1. Signal strength and background

In order obtain the atomic flux distribution from the measured distribution of fluorescence counts an analysis of the signal's variance has to be performed. A rigorous derivation of the number of photon counts per atom for a certain integration time is given in [32]. As can be seen in Figure 6.1, the signal strength saturates whereas the increase in background counts scales linearly with integration time. The signal to noise ratio strongly depends on the integration time and it has a maximum at the largest curvature of the atomic saturation curve. For thermal atoms it is on the order of ≈ 20 and for the ultra-cold samples, due to the slower scattering rate, it is around $5-10$, depending on the mean atomic flux. For the measurement of the atomic flux distribution an integration time of 200 μs was chosen.
The signal strength is given by α, defined as the average number of counts per atom

$$\langle n_{cts} \rangle = \alpha \langle n_{at} \rangle \tag{6.1}$$

which can be determined by comparing the variance and the mean of the detection signal

$$\frac{\langle \delta n_{cts}^2 \rangle}{\langle n_{cts} \rangle} = 1 + \alpha \frac{\langle \delta n_{at}^2 \rangle}{\langle n_{at} \rangle}, \tag{6.2}$$

as shown in Figure 6.2. This assumes the generation of photon counts by an atom to be a Poissonian process and the statistics of background counts to be negligible. Both assumptions are well fulfilled, as already observed with the time interval distribution (see section 5.1). For all measurements Poissonian statistics of the atomic flux were found, thus it is justified to set $\langle \delta n_{at}^2 \rangle = \langle n_{at} \rangle$ reducing the above relation to

$$\frac{\langle \delta n_{cts}^2 \rangle}{\langle n_{cts} \rangle} = 1 + \alpha. \tag{6.3}$$

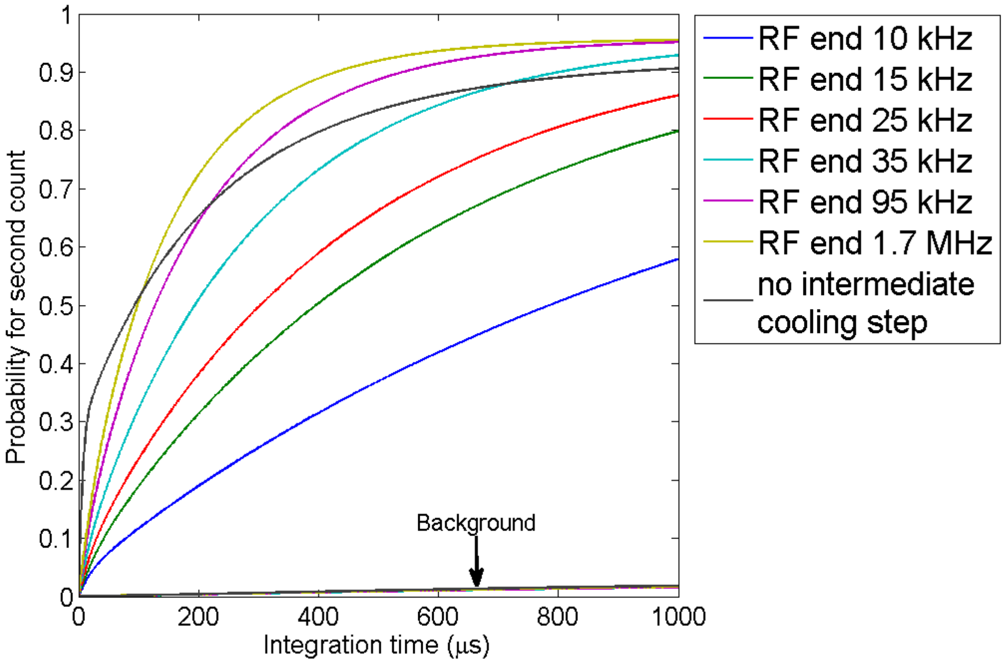

Figure 6.1.: Integrated time interval distribution: this is the cumulative sum of the time interval distribution plotted in Figure 5.1 for samples prepared with different temperatures, defined by the end values of the RF cooling above the trap bottom. This is the probability to detect another count after a certain integration time. This is done with guided atoms and also without atoms giving the signal background by the excitation light. For atoms this is a saturating curve and for the background it grows linearly in time. There is a certain integration time at the largest curvature, where the signal to noise ratio has its maximum value. The black curve is measured from a sample not pre-cooled in an intermediate trap, the other signals are pre-cooled for better mode-matching to the chip trap to different end temperatures. The differing shape of these curves indicate the different dynamics at the detector as discussed in the previous chapter.

Therefore it is sufficient for the measurement of α to take the slope of a linear fit of the signal's variance plotted versus its mean, as shown in Figure 6.3 for different temperatures. As in the previous chapters a difference of a factor ≈ 5 is observable between atomic samples which are directly loaded from the magneto-optical trap into the chip trap and those samples where evaporative pre-cooling is performed in a larger magnetic trap to prepare an ensemble better mode-matched to the very elongated chip-Z trap. The coldest samples are quasicondensates, where the cooling knife is ten to a few tens of kHz above the trap bottom. The warmest of these pre-cooled clouds has a knife more than 1.5 MHz above the trap bottom, thus the temperature is in the few μK range. All of these pre-cooled samples have a similar signal strength, as can be seen in Figure 6.4 independent of their temperature. The sample without pre-cooling on the other hand has a much higher signal strength. Most probably these atoms are transversally more excited than the other samples and therefore the interaction with the detection light is different, as was already described in the previous chapters.

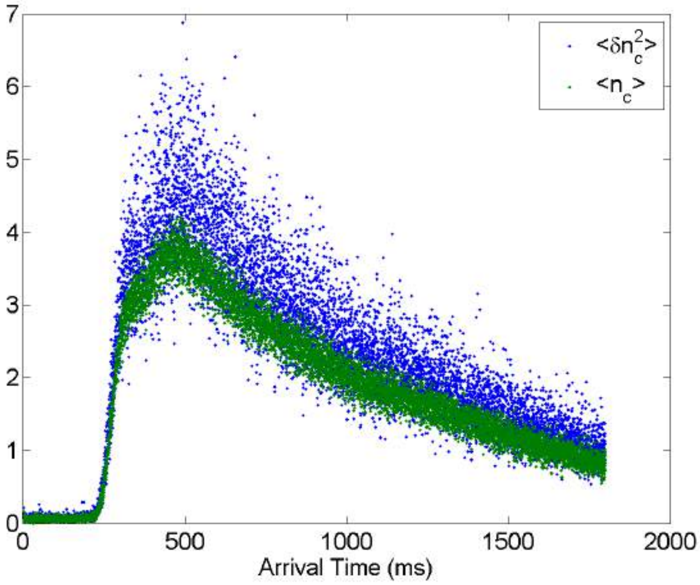

Figure 6.2.: Variance and mean of photon counts for one ultra-cold atomic sample. The ratio of these parameters is related to the signal strength α.

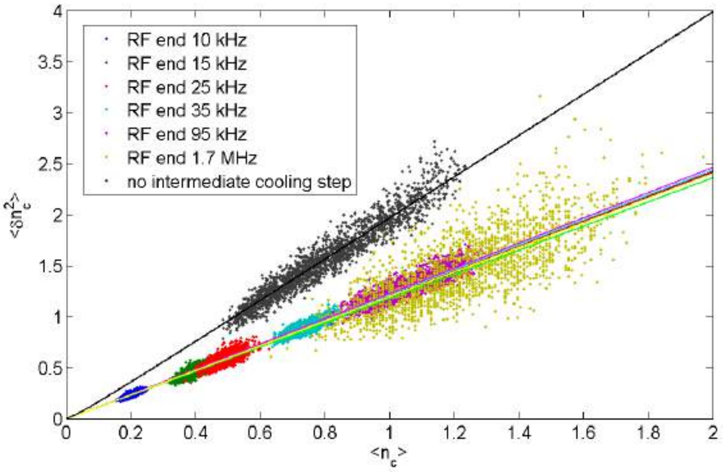

Figure 6.3.: Variance versus mean of the fluorescence photon counts for different signals measured at late atomic arrival times where the signal strength is constant. The slope of the linear fit is directly proportional to the signal strength α, and it is corrected for Poissonian background counts measured at times without atomic presence. The sample without pre-cooling before the chip trap (black) has a steeper slope and thus larger signal strength than the other ensemble at smaller temperatures. From the linearity of the data a Poissonian distribution is deducible for all temperatures.

This measurement of α at late arrival times, i.e. at times ≥ 1 s, allows a determination of the mean atom flux in a certain time bin, which is just the number of detected counts over this signal strength α. This works because α is almost constant for these times, thus it is possible to use a mean α. Such a description is no longer possible for the early arrival times (see next section). It has to be emphasized again that the signal strength is calculated from the measured variance of the count distribution, which is directly related to the second order correlation for a time interval $\Delta t = 0$. Thus the mean atomic flux is derived by ignoring any correlations deviating from a Poissonian distribution but since there is no evidence for such a deviation it is justified to do so. It is therefore futile to consider any correlations of the flux distribution.

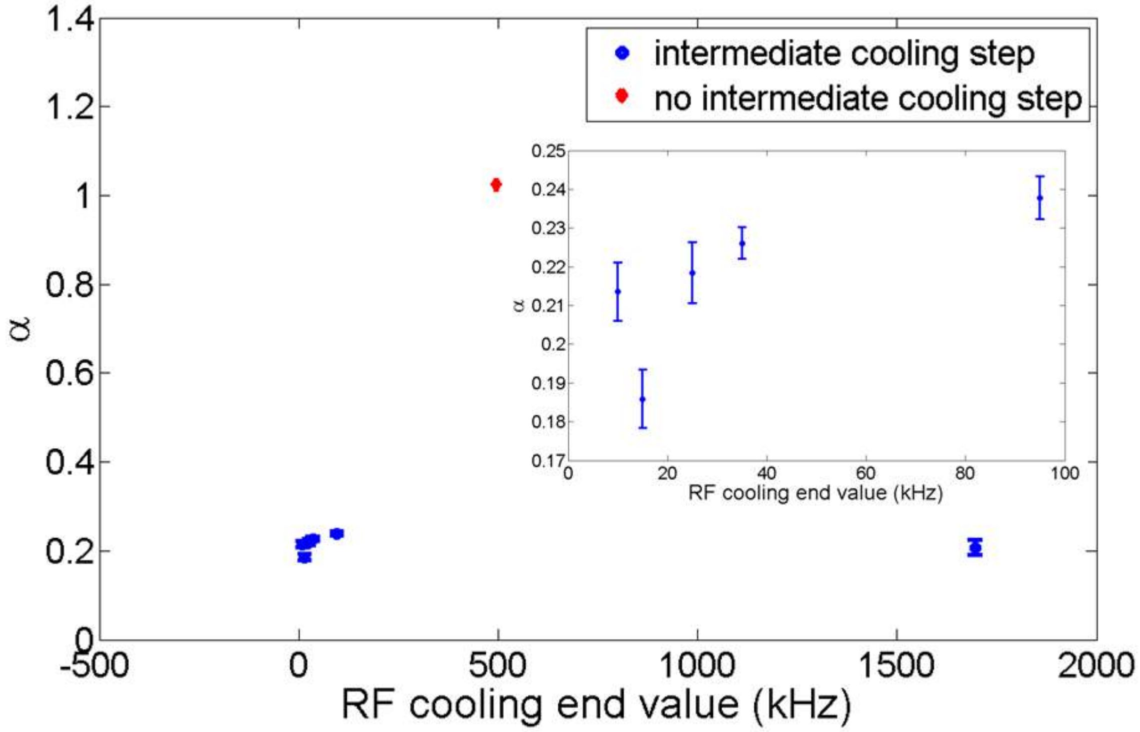

Figure 6.4.: The signal strength α derived from the fits in Figure 6.3, for different temperatures defined by the end values of the RF cooling ramp: the ultra-cold samples with $\alpha \approx 0.2$ are evaporatively pre-cooled in a larger magnetic trap making it possible to be further cooled in the chip trap, the sample without pre-cooling (red) has a much larger signal strength $\alpha \approx 1$ because these atoms at $\approx 20\ \mu$K have enough kinetic energy to enter the region of maximum scattering rate into the collection fibre.

6.2. Time dependence of the signal strength

As already indicated in the previous chapters, the signal strength α of transversally confined atoms in the magnetic wave guide is smaller than those with a high thermal occupation of the transversally excited energy levels. As a possible reason a geometric effect seems to play a role in this lower collection rate of fluorescence photons: Less atoms seem to enter the region of maximum photon collection efficiency because they get repelled by the detection light.

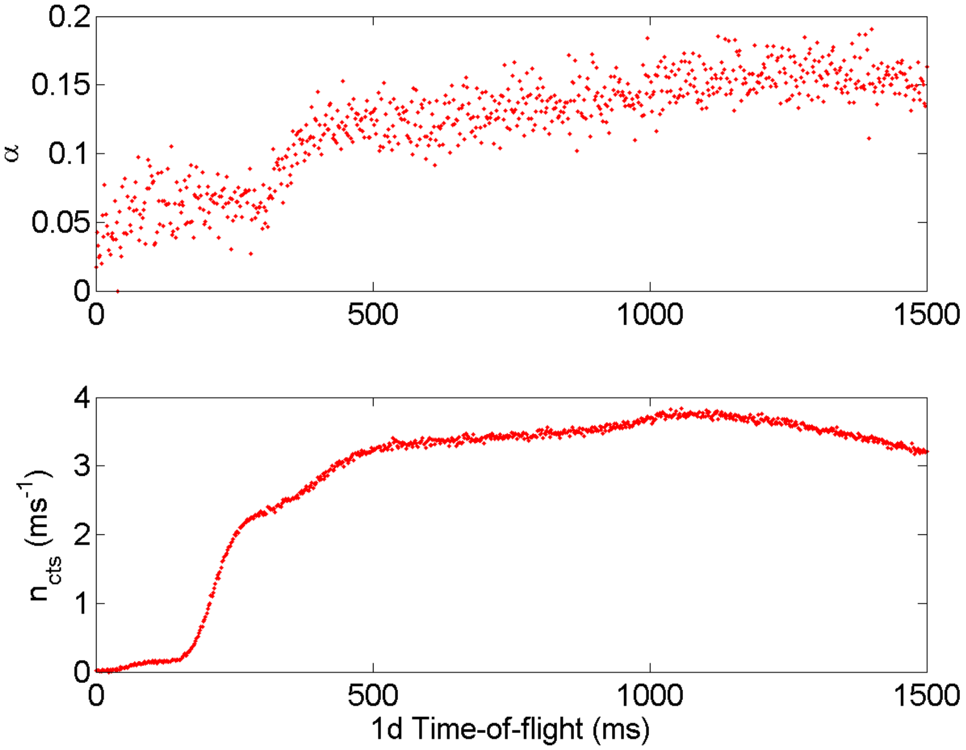

Figure 6.5.: Signal strength α and mean photon count rate $n_{cts}(t)$ versus 1d time-of-flight for an atomic ensemble initially cooled with an RF-knife 35 kHz above the trap bottom. Note the step in the signal strength by a factor of ≈ 2 between 300 and 400 ms, which occurs some time after the first slope of the mean signal.

If an analysis of the variance over the whole arrival time span is made, as is done for Figure 6.5, an additional effect can be observed: α is smaller by a factor of ≈ 2 before it reaches its final value discussed in the previous section. The atoms arriving at the detector in the first few hundred milliseconds scatter light even more slowly than in the late arrival times where the signal strength is reaches a plateau. So there seem to be two different kinds of signal measured with differing efficiency, where the contribution to the total signal transitions from the one type to the other within ≈ 100 ms. A possible explanation of this effect occurring with all ultra-cold signals (see Figure 6.6) is given in more detail in the next section. In order to transform the fluorescence count signal into an atomic flux distribution a time dependent α has to be assumed. This is valid because it was shown that the decay time of the time interval distribution (described in detail in section 5.1) is still strictly given by the inverse mean count rate for this early part of the signal with smaller α. This means that the atomic arrival statistics is locally Poissonian and a simple variance analysis can be performed to obtain the signal strength. The final atomic flux distribution is given by the measured count rate divided by the time-dependent $\alpha(t)$ correcting the signal shape to a physical distribution of arriving atoms (see an example in Figure 6.7 in comparison to the original count distribution). The resulting atomic flux distribution has a visible peak in the first few hundred milliseconds and a long, slowly decaying tail. This distribution can be related, using the methods discussed in section 2, to the ensemble in the initial chip trap before loading into the wave guide. A few additional assumptions have to be made though, as described in the next chapter.

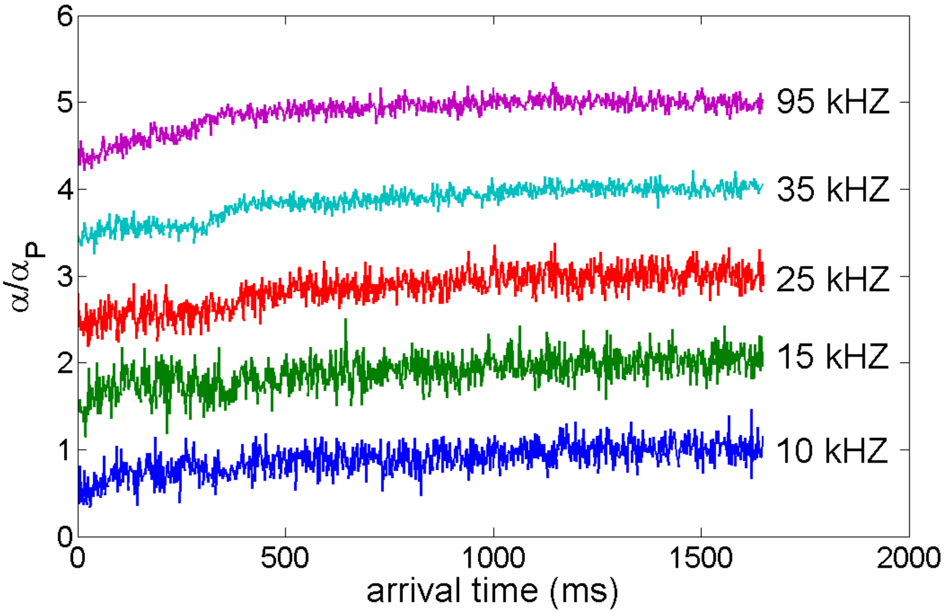

Figure 6.6.: Signal strength α versus time, normalised by the mean signal strength α_P, obtained from the plateau in the detection efficiency for late arrival times for atomic samples prepared at different end values of the cooling RF. The data is offset by integer numbers for better visibility. An increase of the detection efficiency can be seen at around 300 ms for all ensembles as well as a convergence to the plateau value.

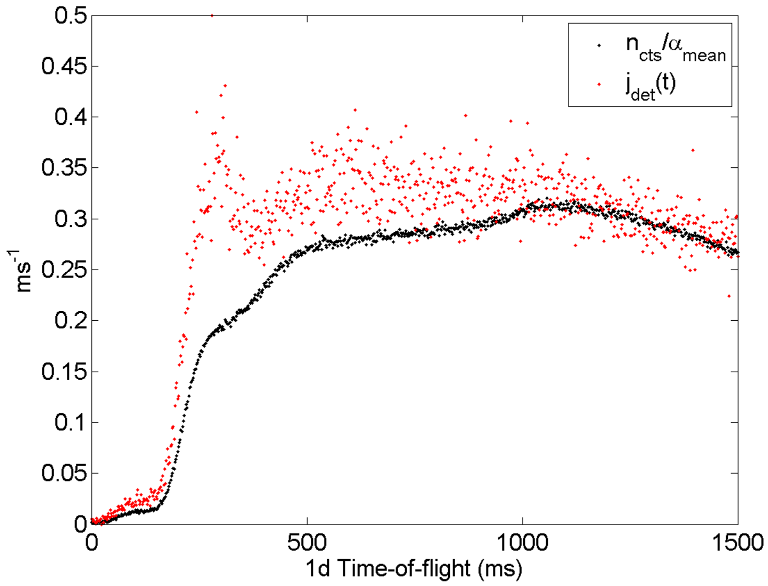

Figure 6.7.: Photon count distribution $n_{cts}(t)$ compared to the final atom flux distribution defined by $j_{det}(t) = n_{cts}(t)/\alpha(t)$. For better comparability, the count distribution is normalised to the mean α of the long tail of the distribution as defined in the previous section. So the black data points would be the atomic flux assuming constant signal strength, whereas the red points take the time dependence of α into account.

7. Micro-optics: Results and outlook

After the phenomenological treatment of the measurements involving the atomic current through the detector, the different approaches are combined to give an explanation of the signal shape. First a comparison between the resonant fluorescence detector and the off-resonant dipole barrier (7.1) indicates that both light fields act in a similar way onto the atoms. This leads to the conclusion that the possibility of trapped atoms near the detection region has to be included, in order to understand the whole signal (7.2). After including of such a long-lived atomic signal in the theory introduced in chapter 2 the full signal is compared to it. Since a primary goal of the micro-optics experiment was the measurement of possible quantum correlations between the atoms of an expanding quasicondensate, a brief analysis (7.3) of the measured correlation function indicates that such correlations are either non-existent due to the expansion, or not measurable. Lastly possible improvements of the fluorescence detector are discussed (7.4).

7.1. Comparison of the resonant and the dipole barrier

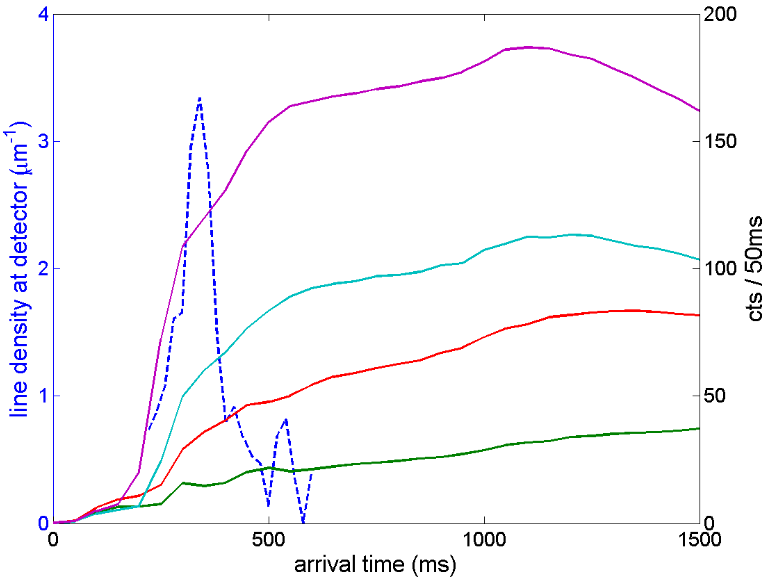

Figure 7.1.: Comparison of the detector signal (solid lines, colors are different initial temperatures) to an imaged density distribution at the detection region without any light from the excitation fibre. A large discrepancy between the respective timescales can be observed.

In this section an attempt is made to explain the shape of the detection signal by combining the results of the previous chapters. For cold atoms below and close above the condensation threshold, the atomic flux distribution takes on a non-trivial form, and also the signal strength seems to change during 1d time-of-flight. If one compares the timing of the imaged density at the detection region of a freely propagating quasicondensate without detection light on and the detected arrival time distribution one immediately observes a large difference in the signal shape (see Figure 7.1). Without detection light most of the atoms have passed the detection region after a few hundred milliseconds, whereas in the working detector the signal's maximum arrives after more than one second. Thus the detection light changes the dynamics of the incoming atoms, as we have seen in chapters 5 and 6. It is revealing to compare the timescale of this dynamic with that using a dipole barrier instead of resonant light. There are several contributions discussed and partly justified by comparison with similar systems. First, the jump in the detection efficiency can be understood as a geometrical effect due the transversal dynamics of the atoms near the detector, similar to what was seen with the dipole barrier. Then a reflection at the guide potential is introduced to explain the second peak in the flux distribution. Finally the atoms seem to be trapped in the vicinity of the detector, which can be described by an effective model.

7.1.1. Discussion of the detection efficiency jump

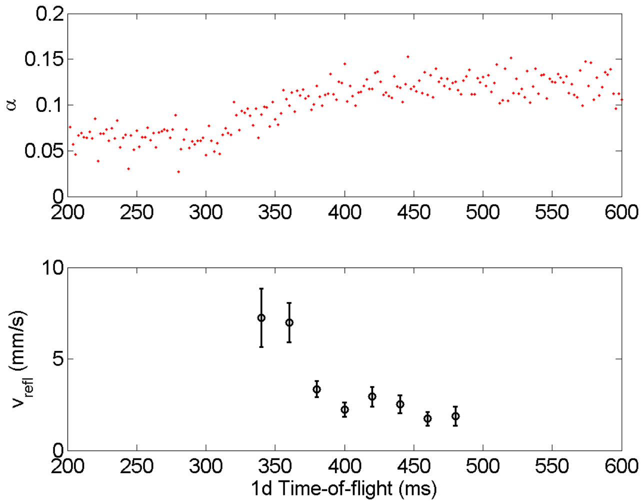

Figure 7.2.: Comparison of the time dependence of the signal strength α in the fluorescence detector (top) and the derived velocity of atoms (bottom) reflected from the dipole barrier at the position of the detector. The smaller velocity corresponds to many trapped atoms near the barrier. As in the dipole barrier case, the number of atoms accumulating near the detector increases, due transversally excitations. The photon scattering rate into the detection fibre thus increases correspondingly, and the signal strength rises until most of the atoms are excited.

As can be seen in Figure 7.2, the timescales for both resonant and completely off-resonant light seem to agree. The most simple explanation for this agreement is that the atom dynamic in the resonant detection light is similar to that in a combined magnetic guide and a dipole barrier. For atomic ensembles transversally in the ground state, the focused light from the tapered fibre seems to build a reflecting potential barrier. The atoms are not able to enter the cone of maximum photon coupling to the collection fibre as long as they stay in the transverse ground state. The signal starts to rise when more and more atoms are trapped near the detector, getting excited transversally due the angled geometry of the combined magnetic and radiation pressure force. In Figure 7.3 this increase in signal strength is compared to the contribution of trapped atoms to the total signal, as further discussed in this chapter. This trapping may explain the long lifetime of the atomic signal compared to the case without detection light. In front of the detector a kind of atomic battery is "charged" until the incoming atomic current reduces. The battery leaks into the region of highest photon collection efficiency on a much longer timescale than that of the incoming current pulse.

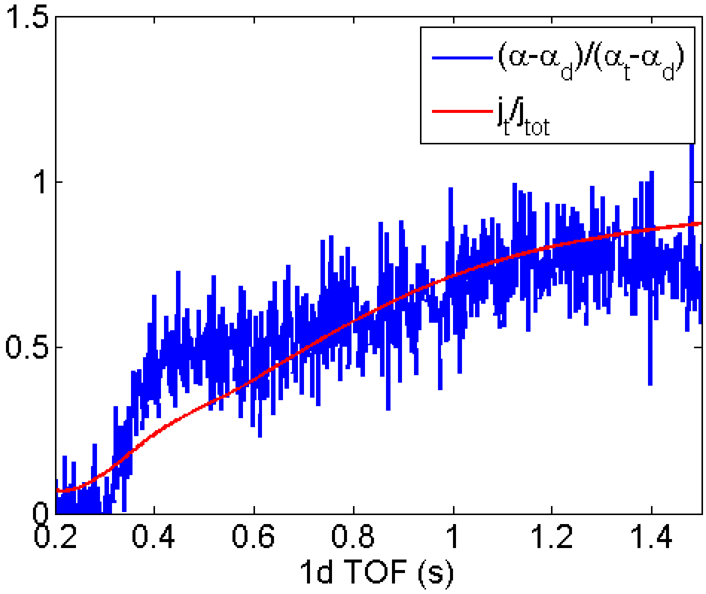

Figure 7.3.: Comparison of the relative increase of the signal strength $\alpha(t)$ in the resonant fluorescence detector with the relative contribution of initially trapped atoms near the detector to the total atomic flux measured in the detector. This ratio of different fluxes is obtained from the fit described in Figure 7.7. Initially only atoms directly entering the detector are measured with a low direct signal strength α_d defining the base level of the relative increase, then the amount of trapped atoms is increased to almost 100 % after $\approx$ 1.5 s, leading to a similar increase in signal strength until it reaches the mean final α_t.

7.1.2. Accumulation of atoms near the detection region

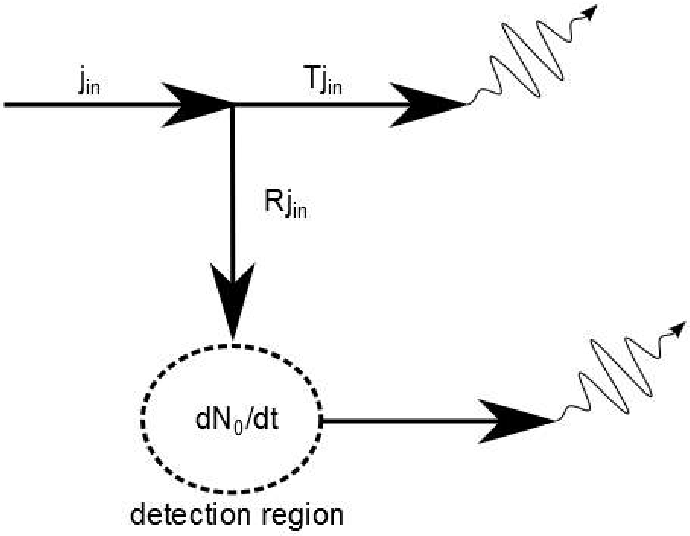

Figure 7.4.: Schematics of the atom detection process using the continuity equation. First the incoming flux j_{in} is split in a part Tj_{in} which is directly detected and a part Rj_{in} of atoms being trapped for longer times near the detector and therefore accumulating to a number of $N_0(t)$ before they are detected away at a slow rate.

Following this interpretation of atoms losing their initial longitudinal velocity one can make a heuristic model for the number of atoms being accumulated close to the detection region after a time t. First one has to differentiate between atoms detected away directly upon arrival and those trapped for some time before detection. For this one has to employ the continuity equation, leading to a relation

$$j_{in}(t) = j_t(t) + j_r(t) = Tj_{in}(t) + Rj_{in}(t) \tag{7.1}$$

of $j_t(t)$ for the atoms directly detected and of $j_r(t)$ for atoms trapped near the detector to the incoming flux $j_{in}(t)$. This can be described by effective transmission and reflection coefficients T and R in close analogy to an optical mirror (see 7.4). In order to calculate the number of accumulated atoms $N_0(t)$ the continuity equation

$$\frac{dN_0(t)}{dt} = j_t(t) = Rj_{in}(t) \tag{7.2}$$

is useful again to relate it to the part of the incoming flux not detected immediately. This can be formally integrated so that

$$N_0(t) = R\int_0^t j_{in}(t')dt' \tag{7.3}$$

This loading with atoms is closely related to the charging of a capacitor with the difference that the charged electrode does repel incoming charges, leading to a characteristic exponential loading curve, whereas the atoms do not repel each other as long as the interaction energy can be assumed to be small. This should be the case for transversally excited atoms after reflection from the detection light because there are many states available to occupy and therefore possible initial degeneracy will be gone after reflection. So ideally the "charging" of the detection region would go on until all atoms from the wave guide are trapped there. But of course some of them are detected away and therefore one has to assume a rate of atoms being lost. Using the fact that the detection process is, to a good approximation of Poissonian nature (see chapters 5 and 6), one can define a loss of the trapped atoms due to detection by

$$N(t) = e^{-t/\tau} N_0(t) \tag{7.4}$$

with an average detection rate of $1/\tau$. In order to obtain the mean rate of detected atoms one has to multiply the number of atoms with this single-atom detection rate:

$$j_N(t) = \frac{N(t)}{\tau} = R\frac{e^{-t/\tau}}{\tau} \int_0^t j_{in}(t')dt'. \tag{7.5}$$

The timing of this charging flux can be compared to that of the density next to the dipole barrier (see Figure 7.5). The full flux measured by the detector becomes

$$j_{det}(t) = T j_{in}(t) + R\frac{e^{-t/\tau}}{\tau} \int_0^t j_{in}(t')dt'. \tag{7.6}$$

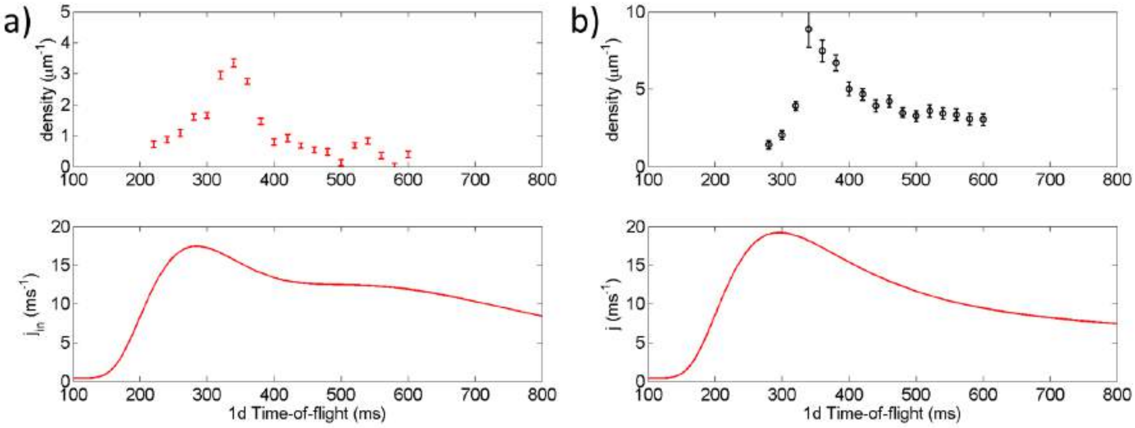

Figure 7.5.: Comparison of the imaged atomic density near the detector and different contributions to the atomic flux measured by the fluorescence detector. **a)** Without any light going through the detection fibre, the atomic density decreases very rapidly after the first peak. The detection signal below shows similar behaviour, although the contribution from the delayed reflection at the guide potential is visible. **b)** For the case with a dipole barrier the density is larger than without and it stays so for the rest of the time due to the trapped atoms. The same is true for the detection signal below, where the trapped atoms are responsible for the majority of the total signal.

7.2. Full analysis of the atomic flux

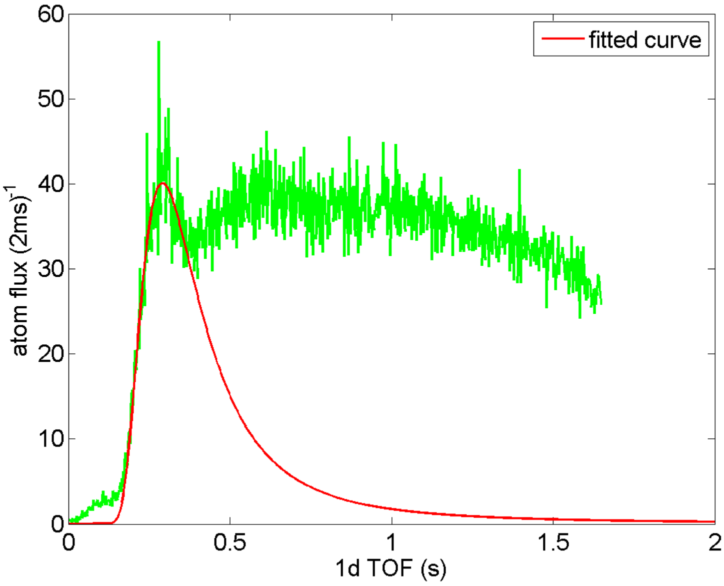

Figure 7.6.: Comparison of a theoretically derived flux distribution given by eq. 2.17 and the measured data for the atomic flux. The initial peak seems to be well described by theory but the timescale of the measured data is much longer than explainable by this simple approach.

It can be seen in Figure 7.6 that a simple Boltzmann fit to the data does not describe the whole signal as for warmer atoms. Only the first peak in the distribution seems to be describable by such a fit. With the ingredients introduced above it is possible to analyse the full atomic flux distribution. The total incoming flux is given by the sum of atoms directly propagating towards the detector and atoms being first reflected by the guide potential

$$j_{in}^{tot}(t) = j_{in}(z_d, t) + j_{in}(z_d + \delta z, t). \tag{7.7}$$

The detected atomic flux can be related to the total incoming flux by

$$j_{det}^{tot}(t) = T j_{in}^{tot}(t) + R \frac{e^{-t/\tau}}{\tau} \int_0^t j_{in}^{tot}(t')dt', \tag{7.8}$$

which can be further decomposed into direct and reflected parts

$$j_{det}^{tot}(t) = T\left[j_{in}(z_d, t) + j_{in}(z_d + \delta z, t)\right] + R\frac{e^{-t/\tau}}{\tau}\int_0^t \left[j_{in}(z_d, t') + j_{in}(z_d + \delta z, t')\right]dt'. \tag{7.9}$$

The collection of these terms can be used to perform a fit to the full atomic flux distribution. In the following a fit of a thermal Boltzmann distribution and of a Thomas-Fermi distribution at $T = 0$ are compared.

7.2.1. Thermal distribution

In Figure 7.7 a fit of a thermal distribution to the data is shown. For this, the flux due to a Boltzmann distribution (eq. 2.17)

$$j_{in}^{th}(t) = N\sqrt{\frac{m}{2\pi k_B T}}\frac{z_d}{t^2}e^{-\frac{mz_d^2}{2k_B T t^2}}$$

is used as derived in chapter 2. First the loading of the detection region has to be calculated for this case,

$$N_0^{th}(t) = R\int_0^t j_{in}^{th}(t')dt' = RN\sqrt{\frac{m}{2\pi k_B T}}\int_0^t \frac{z_d}{t'^2}e^{-\frac{mz_d^2}{2k_B T t'^2}}dt'. \tag{7.10}$$

Integration gives

$$N_0^{th}(t) = R\frac{N}{2}\,\mathrm{erfc}\left(\sqrt{\frac{m}{2k_B T}}\frac{z_d}{t}\right), \tag{7.11}$$

with the complementary error function defined as

$$\mathrm{erfc}(x) := \frac{2}{\sqrt{\pi}}\int_x^\infty e^{-x'^2}dx'. \tag{7.12}$$

Thus the detected current of the initially trapped atoms according to Equation 7.5 is

$$j_N^{th}(t) = R\frac{N}{2}\frac{e^{-t/\tau}}{\tau}\,\mathrm{erfc}\left(\sqrt{\frac{m}{2k_B T}}\frac{z_d}{t}\right). \tag{7.13}$$

After a Galilei transformation due to a centre-of-mass velocity the final flux of the trapped thermal atoms

$$j_N^{th}(t) = R\frac{N}{2}\frac{e^{-t/\tau}}{\tau}\,\mathrm{erfc}\left(\sqrt{\frac{m}{2k_B T}}(\frac{z_d}{t} - v_{cms})\right) \tag{7.14}$$

is obtained.

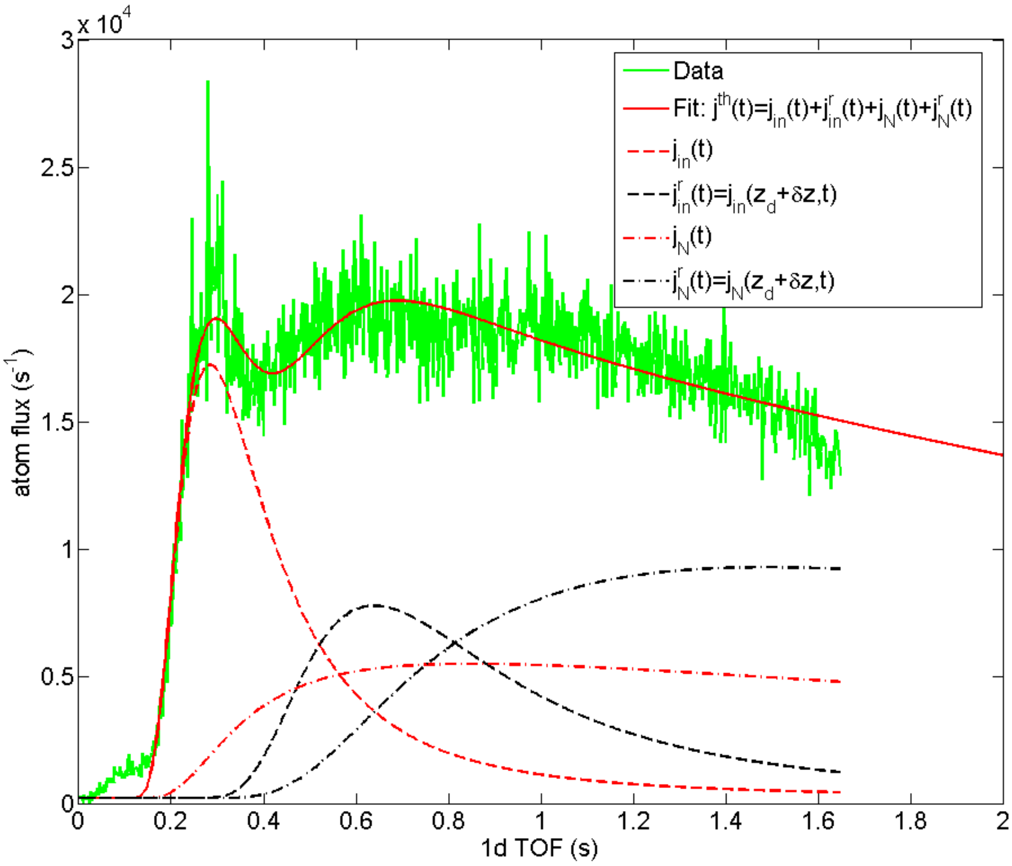

Figure 7.7.: Atomic flux versus arrival time at the detector. The full fit $j^{th}(t)$ is given according to the main text as sum of four terms of the thermal distribution: The flux of atoms, which are immediately detected $j_{in}(t)$, and the flux of atoms $j_N(t)$ which are detected on a longer timescale, because they were initially trapped close to the detector (both in red). And then there are two similar contributions from atoms initially propagating away from the detector until they are reflected at the turning point of the guide potential: The immediately detected atomic flux $j_{in}^{(r)}(t)$ of the reflected atoms and $j_N^{(r)}(t)$, the contribution of reflected atoms which are initially trapped close to the detector before being detected (both in black). It can be observed the last contribution is the main cause of the long tail of the total distribution. The most relevant fit parameters are the temperature and centre-of-mass velocity. For the temperature values between 500 nK and a few μK are found. This underestimates the temperatures for the coldest samples at ≈ 50 nK. Thus for doing thermometry, a few more calibration measurements should be done, which fix some of the other fit parameters. For the centre-of-mass velocity values of $10 - 15$ mm/s are found, in agreement with the value found by the pulsed measurement (see Section 5.2). The ratio of directly detected flux to detection after an initial trapping is $T/R \approx 1 : 5$. Thus 5 times more atoms are trapped instead of immediately being detected. The values for the lifetime τ in this trap range from ≈ 1 s for the warmer samples to much larger values which are possibly because the total measurement time is too short to describe the right behaviour at these late times.

7.2.2. T = 0 distribution

Since at low temperatures the atomic ensemble is in the quasicondensate phase in the initial trap the contribution of atoms in this phase to the detection signal has to be discussed. As has been shown in chapter 2 for a BEC at $T = 0$ in the Thomas-Fermi approximation an analytic expression for the atomic flux after a certain expansion time t exists. For the distribution (eq. 2.28)

$$j_{in}^{TF}(t) = \frac{n_p}{b(t)} \left[1 - \frac{z_d^2}{b^2(t)R_0^2}\right] \frac{\dot{b}(t)}{b(t)} z_d \Theta\left[b(t)R_0 - z_d\right], \tag{7.15}$$

(where the centre-of-mass velocity has been omitted for the moment), a loading of the detection region has to be assumed, as in the thermal case. First, the integral

$$N_0^{th}(t) = R \int_0^t j_{in}^{TF}(t')dt' \tag{7.16}$$

is solved to

$$N_0^{th}(t) = R n_p R_0 \left(\frac{2}{3} - \frac{z_d}{b(t)R_0} + \left(\frac{z_d}{b(t)R_0}\right)^3\right) \tag{7.17}$$

and after a Galilei transformation it can be used to express the measured flux of trapped atoms as

$$j_N^{TF}(t) = R n_p R_0 \frac{e^{-t/\tau}}{\tau} \left(\frac{2}{3} - \frac{z_d - v_{cms}t}{b(t)R_0} + \left(\frac{z_d - v_{cms}t}{b(t)R_0}\right)^3\right). \tag{7.18}$$

So also for the BEC an analytic solution for the full problem exists. If this is compared to the data (see Figure 7.8) one can come to the conclusion that the part of the true condensate or the Penrose-Onsager mode [52] is small, or the ensemble loses its coherence (or its memory thereof from the initial trap) before it arrives the detector. This loss of coherence is also indicated by the fact that no inter-atomic coherence was found (see the next section). It should also be emphasised again, that in the quasicondensate regime many longitudinal excitations are still occupied. These are phonon-like, i.e. there are no large density fluctuations due to the interaction energy but phase fluctuations which result in fluctuations in the velocity field of the condensate, which looks like a thermal distribution in momentum space. Since the atomic flux is measured in the detector, these velocity fluctuations make a large contribution to the signal, making it impossible to distinguish from an ideal gas source. This also explains why there seems to be no visible or quantifiable difference between the completely different temperature scales at which the experiments were performed, from 50 nK to the few microkelvin regime.

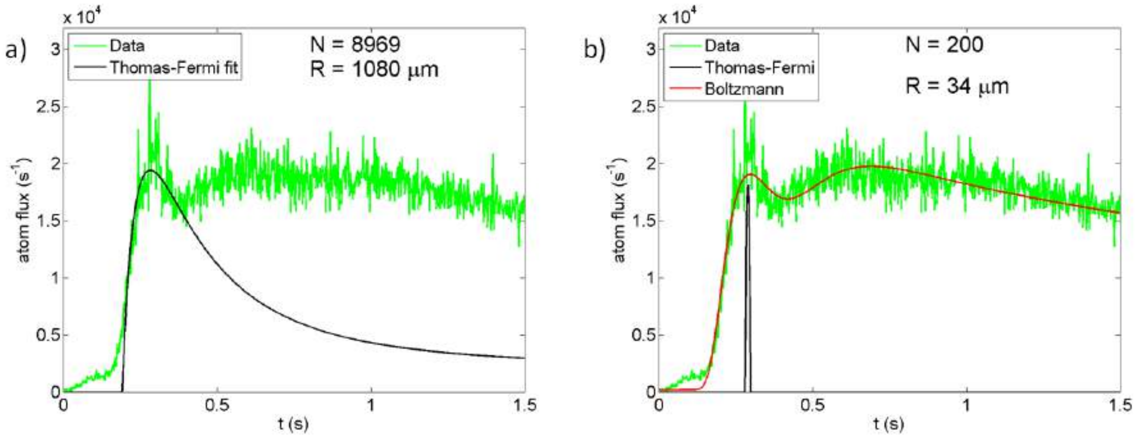

Figure 7.8.: Two possible ways to introduce a Thomas-Fermi fit to the detection signal. **a)** Using both the initial radius R and the atom number N as free independent fit parameters (which they are not, if the trap frequencies are known), one obtains a reasonable agreement with the first peak in the distribution, but the resulting fit parameters are incompatible by $2-3$ orders of magnitude. **b)**Another approach is using N as the only parameter and by tuning it one finds the right signal height for a very small number of atoms compared to the that obtained from the corresponding Boltzmann fit (order of 10000). This means, if there are some atoms in the true condensate phase, they will be completely hidden in the background of - at least longitudinally - excited atoms.

7.3. On inter-atomic correlations

One of the initial goals of the fluorescence detector was to measure atomic correlations in a Hanbury-Brown and Twiss type [10] intensity interferometry. There is a clear difference between the atomic density-density correlation function $g^{(2)}(z,z') := \langle \hat{n}(z)\hat{n}(z')\rangle / (\langle \hat{n}(z)\rangle \langle \hat{n}(z')\rangle)$ of a thermal Bose gas and a BEC (see [50]). Their behaviour can also be described in terms of flux-flux correlations

$$g^{(2)}_{fl}(z,t;z',t') := \frac{\left\langle \hat{I}(z,t)\hat{I}(z',t')\right\rangle}{\left\langle \hat{I}(z,t)\right\rangle \left\langle \hat{I}(z',t')\right\rangle}, \tag{7.19}$$

with the atomic flux operator $\hat{I}(z)$ defined by 2.1, which can be directly related under some assumptions to the (rescaled) density-density correlations [26]. In the micro-optics experiment atomic ensembles in different regimes were prepared in the initial Z-trap and loaded into the wave guide. While the coldest samples were deep in the quasicondensate regime at temperatures of ≈ 50 nK, where the contribution of the thermal background gas is already very small, some measurements were also taken at the crossover between quasicondensate and thermal gas at $\approx 1\ \mu$K and finally, ensembles with many transversal excitations at a few tens of microkelvin were studied. The measured correlation function is obtained by replacing the flux operator in eq. 7.19 by a sum

$$\hat{I}(z,t) = j(z,t) + \delta\hat{j}(z,t) \tag{7.20}$$

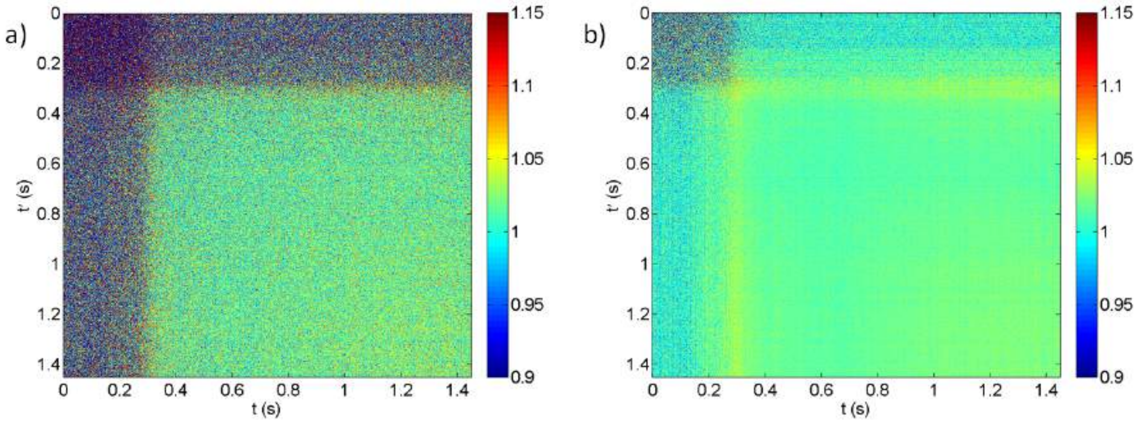

Figure 7.9.: Measured correlation functions of the atomic signal as defined in eq. 7.19 with an integration time of **a)** 200 μs and **b)** 1 ms. The darker areas are correlations with the background noise before the actual signal. It can be observed that the features exceeding a value of 1.05 for the longer time binning completely vanish by going to the smaller time bins. Given that the coherence time in the atomic ensemble should still be small compared to the integration time, these small correlations are most probably caused by technical time jitter close to the regions of largest slope in the signal.

of its expectation value $j(z,t) = \langle j(z,t) \rangle$ and fluctuations $\delta\hat{j}(z,t)$ around it to give

$$g^{(2)}_{exp}(t,t') = 1 + \frac{\langle \delta j(z_d,t)\delta j(z_d,t') \rangle}{j(z_d,t) j(z_d,t')}, \tag{7.21}$$

where the expectation values are given by averaging over many measurements. Such a correlation function can be seen in Figure 7.9 for a cold ensemble at the crossover to the quasicondensate regime. The measured correlation function shows no significant correlations, as is the case for all other temperature scales for small integration times. The very small features visible in the plot with larger integration times coincide with the times where the slope in the count signal is steep, and thus the error is most sensitive to fluctuations in time between realisations. This systematic effect is uncovered by the comparison to smaller integration times, where these false correlations vanish, whereas physical ones would be more pronounced. There are several explanations why occurring correlations may not be measurable with this detector. The main reason has been discussed in this chapter, most of the signal is given by atoms scattering randomly with the detection light and staying very long close to it. Therefore at all times several atoms contribute to the correlation function and therefore spoil any coherence.

7.4. Possible workarounds: an outlook

This experiment showed the advantages and the drawbacks of this type of fluorescence detector. There are two directions of improving this device: increasing the number of photon counts per atom to increase the signal to noise ratio and therefore to maybe address atoms individually rather than only statistically. The second approach towards improvement is changing the atom dynamics in the detector in such a way that atoms scatter photons rapidly and then leave the detection region completely without any trapping effects. This second problem is solved very easily by modifying the position of excitation and collection fibre (see Figure 7.10) such that the excitation light points away from the atomic source so that the radiation pressure always accelerates the atoms towards the opposite side of the detection region. This should largely prevent the atoms from being trapped and it should be easier to recognize individual atoms by a sudden photon burst. This fast scattering of photons should be possible in combination with the first improvement approach, the increase of the detection efficiency by using a larger collection fibre with a core diameter of 200 μm and a numerical aperture (NA) of 0.48 instead of 62.5 μm and 0.13, respectively. This dramatically increases the solid angle within which efficient coupling of fluorescence photons is possible, leading to an average number of ≈ 3.5 photon counts per atoms (see Figure 7.11). Thus the probability to measure at least one count for an atom arriving at the detector is ≈ 0.95. Also by setting a detection threshold to 2 or even 3 counts the false positive detection probability is small enough (< 2 %) to recognise individual atoms, making it possible to manipulate them with fast control. First tests of integrating these fibres have already been performed. The lithographic patterning of the holding structures had to be modified to include a double layer fabrication process (see appendix A). This makes it possible to use fibres with different diameters at the same working distance from the chip surface (as sketched in Figure 7.10 b)).

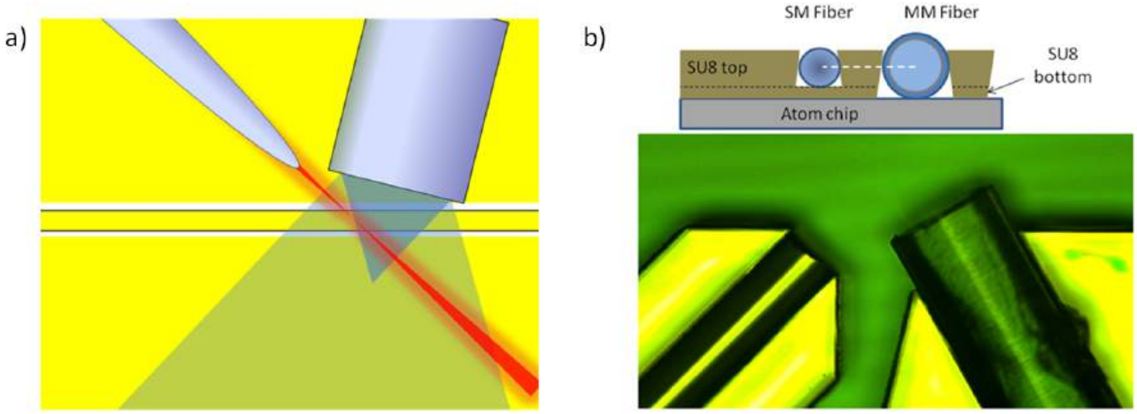

Figure 7.10.: Possible future geometry of the fluorescence detector: **a)** The tapered excitation fibre and the multimode fibre with a larger diameter are integrated on the chip in reversed order compared to the old geometry. If the atoms are transported along the central wire from left to right, the radiation pressure from the excitation light will always point away from the detector. The atoms scatter photons and leave the detection region without being trapped. **b)** Top: a sketch from the side shows the different diameters of the excitation single mode (SM) fibre and the multimode (MM) fibre for photon collection. The larger numerical aperture of the latter fibre compared to collection fibre of the old detector should lead to an increase in detection efficiency. In order to integrate fibres with different diameters a double layer structure had to be designed for the integrated holding funnels on top of the gold chip. A first feasibility test has been successful, as can be seen in the microscope image of fibres mounted into such holding structures.

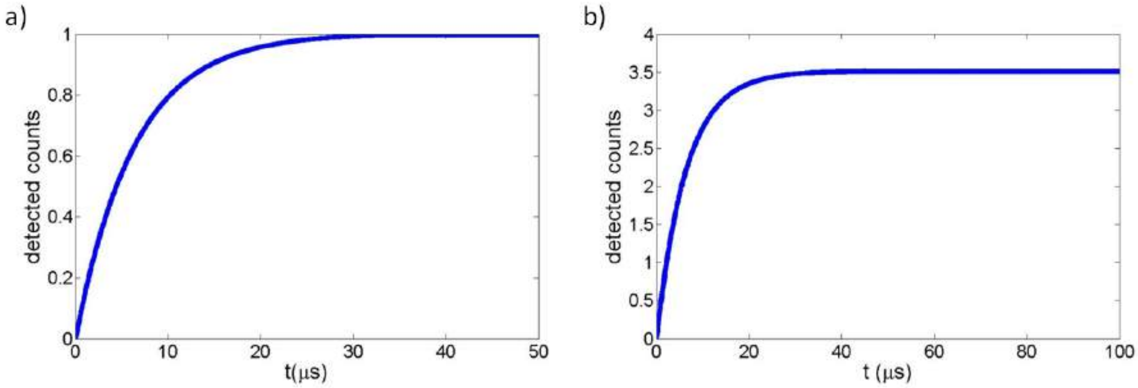

Figure 7.11.: Simulated number of detected fluorescence counts for the collection fibre on the old micro-optics chip **a)** and for a proposed new collection fibre with a diameter of 230 μm and a numerical aperture of 0.48 (**b)**). The atom scatters most of the photons in the first 20 μs to a saturation value of about 1 and 3.5 photon counts, respectively.

Part III.

Coupling atoms to a nanofibre light field

8. Introduction to the nanofibre cavity experiment

Within this thesis integrated optical devices are combined with magnetic atom traps. The advantage of this is the (at least geometric) independence of the optical probing device from the trapping device, the integrated wire. After an introduction of the main components of this new built experiment (8.1) its construction is described and characterised (9). For a first test nanofibres without Bragg mirrors are used in the experiment (10) and its coupling to the MOT is analysed. Then the cavity nanofibre is built in and, after its characterisation in vacuum, the atom-cavity coupling is described (11). In the end the main results are given as well as a brief outlook (12).

8.1. Description of the main components

The main goal of this experiment is a high coupling between a trapped atomic ensemble and a light field. In this Chapter the main ingredients to achieve this goal are introduced: The rubidium vapour, the nanofibre cavity and the scheme to combine both systems.

An ultra-cold Rubidium vapour

The atomic species used in this experiment is rubidium 87 because its preferable properties concerning laser cooling and evaporative cooling. In order to achieve the required high atomic densities and small inhomogeneous broadening of the driven optical transition the atoms have to be well isolated in a vacuum chamber and cooled in a magneto-optical trap (MOT). Most of the atoms are finally in the $F = 2$ hyperfine state and can be cyclically driven via the excited $F' = 3$ state. For a cold vapour these two states form a two-level system to a good approximation, which can be driven by the nanofibre light field.

The nanofibre

The second tool used in this experiment is a nanofibre ([65],[23]), which is a single-mode optical fibre with a diameter of 125 μm, heated and pulled in a 5 mm long region to a diameter of only half the wavelength of the guided light - in the case of this experiment this diameter is 400 nm. At the conic transition region between those extremely different diameters, the guided light inside the fibre's core is adiabatically out-coupled until most of the light is guided outside of the fibre at its thinnest part. There at the waist the

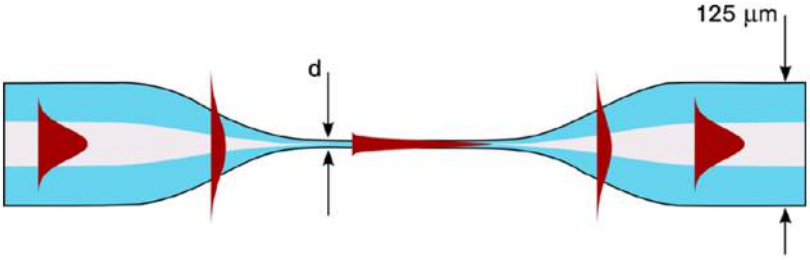

Figure 8.1.: Sketch of the nanofibre (from [23]). In the fibre taper the refractive index step is slowly transformed from a glass-to-glass transition of standard optical fibre to a glass-to-vacuum transition in such a way, that the single mode condition for the light field is maintained. In the thin part with a diameter of $d = \lambda/2$ most of the light power is guided in the evanescent field outside of the fibre. The transmission through the 5 mm long waist is $\approx 99\%$.

evanescent light field is still guided and the transmission to the other end of the fibre in the again thick part is on the order of $\geq 99\%$.

The fibre Bragg mirror Fabry-Perot resonator

In order to enhance the coupling between atoms and the light field at the nanofibre's waist it is placed between two mirrors forming a Fabry-Perot resonator [71]. These mirrors are formed by a refractive index grating directly written into the fibre material with the help of a precisely controlled UV laser [42].

The nanofibre cavity

The combination of the former two tools yields the nanofibre cavity, were the part of the standing wave in the resonator is guided outside the fibre, thus allowing coupling of atoms nearby.

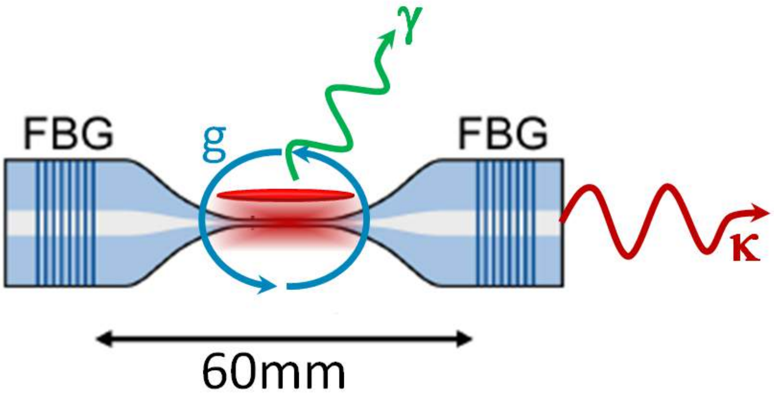

Figure 8.2.: Sketch of the nanofibre cavity. The cavity is a Fabry-Perot resonator built of two fibre Bragg gratings (FBG) separated by 60 mm with a cavity linewidth κ. The atom cloud with a linewidth γ is magnetically brought to a geometric overlap with the evanescent light field with a coupling strength g. (adapted from [71])

Cold atoms near a nanofibre cavity

The last step is the combination of ultra-cold trapped Rubidium atoms and the nanofibre cavity by magnetically aligning both systems until a good geometric overlap provides a large optical density for the transmitted light. This is achieved by mounting the nanofibre cavity adjacent to the copper structure producing the magnetic field, thus allowing good control of the trap position with respect to the nanofibre.

9. Building the experiment

This setup replaced the micro-optics experiment (described in part II). The vacuum system as well as all the coils providing the magnetic fields were replaced, while still using most of the former laser system. The most important components of the vacuum system as well as the pump down procedure are described (9.1). After a discussion of the new coil geometry the principle of the magneto-optical trap in this setup is explained (9.2). Lastly a list of the different lasers and their purposes is given (9.3).

9.1. Vacuum chamber and experiment mount

The starting point of experiments involving ultra-cold atoms is the assembly of a working vacuum system. The described experiment should be capable to achieve ultra-high vacuum with a pressure on the order of $10^{-11} - 10^{-12}$ mbar, for the magneto-optical trap 10^{-8} mbar was shown to be sufficient. The experiment is built using a standard commercially available vacuum chamber[1]. The top flange (B.3) is custom made[2] for the experiment's purposes with wire feedthroughs also designed for future experiments utilizing an atom chip. The flange also contains special feedthroughs for optical fibres[3], which are made UHV-tight with the use of a teflon cone (see [1]). As can be seen in Figure 9.1, on this flange also the experiment block is mounted, thus everything peculiar to this experiment is attached to it. Since the top flange is easy accessible by design, it will be possible to change the experimental setup in a short amount of time.

9.1.1. Experiment mount

The experiment mount contains a solid copper block for good heat conduction to the outside of the vacuum chamber, with pits on top to avoid eddy currents. As an insulating layer between the copper and the experiment wires a machined AlN plate (B.4) is screwed on top of the copper block (see Figure 9.1). A large H-shaped copper structure (B.5) is glued onto the insulating plate with thermally conductive glue[4] (see Figure 9.2). The currents up to 60 A through it provide the inhomogeneity of the magnetic quadrupole field for the magneto-optical trap. The mirror for the MOT is a cleaved silicon wafer (with the exact dimensions of a future atom chip) with a 300 nm layer of gold on top of a 30 nm titanium layer for better adhesion evaporated onto the silicon surface. This mirror

---

[1] Kimball 8.0" Spherical Square - Vacuum Chamber: MCF800-SphSq-G2E4C4

[2] assembled by: tectra GmbH

[3] Swagelok: SS-200-6-2W

[4] EPO-TEK H74

[44] is again glued on top of the copper wire with the same thermally conductive glue . The nanofibre mount is a U-shaped MACOR plate (B.6) fitting around the gold mirror, on top of its legs are glued two piezo actuators[5] with a combination of the thermally and electrically conductive glue[6] as a connection to the feedthrough wires. Onto those piezos the nanofibres are glued with a UV cured epoxy directly after pulling and the mount is screwed onto the experiment mount directly before the flange is mounted onto the vacuum chamber to minimize the probability of contaminating the nanofibre waist with dust. See a sketch of the relative positioning of the nanofibre and the rest of the assembly in Figure 9.2.

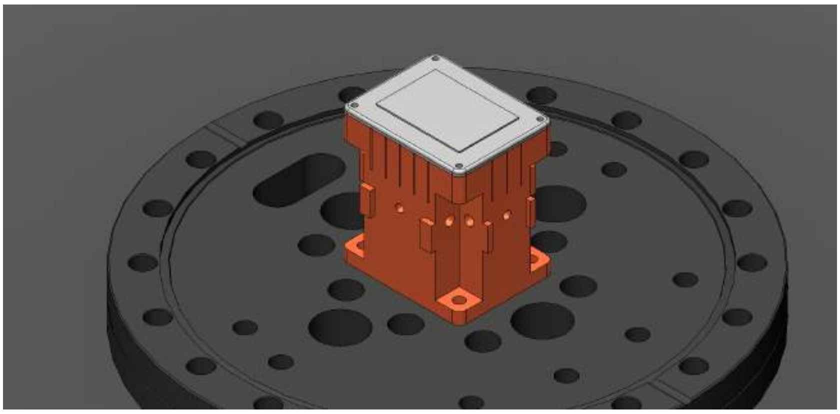

Figure 9.1.: Experiment flange (dark grey) with the copper block (bronze) and the insulating AlN sub-structure (white). The 8 ″ flange contains all the wire and fibre feedthroughs (see B.3).

9.1.2. Vacuum pumps and pump down procedure

After the experiment flange is installed, the system is pumped down carefully, see Figure 9.3 for a sketch of the vacuum system. Attached to the vacuum chamber are an ion pump and a non-evaporative getter pump for the running experiment. The latter is not used in this experiment, since a pressure of $5 * 10^{-9}$ mbar achieved solely with the ion pump is enough for the magneto-optical trap, it will be needed though for atom chip experiments involving BECs. The pump down from atmospheric to low pressures is done by the combination of a turbo-molecular and a membrane pump. Between those pumps a needle valve and a high-pressure gauge are installed for a precise control of the initial pump down during the viscous flow phase, which is crucial to avoid too much particle flux from the chamber walls to the nanofibre due to a large pressure gradient between experiment chamber and pre-pump.

The initial pump phase is performed as follows. After closing the chamber and additional tightening of the fibre feedtroughs, the membrane pump is switched on with the needle valve completely closed until the pressure on the pump side -measured by the gauge- no

---

[5] Noliac: CSAP03

[6] EPO-TEK: E2001-HV

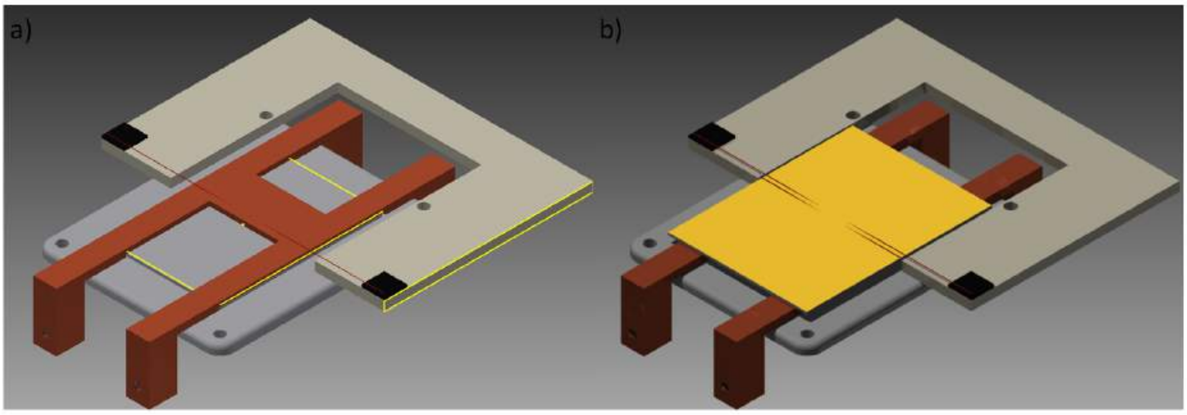

Figure 9.2.: Sketch of nanofibre assembly on top of the copper mount (see Figure 9.1). While in **a)** the whole setup is shown including the gold mirror in **b)** the latter is removed to show the relative position of fibre and copper H. This defines the location of the MOT relative to the nanofibre.

longer changes significantly. Then the valve is opened gently until the pressure has risen to a value not exceeding one order of magnitude larger then the initial pressure. The experiment is left in this state until the pressure has once again decreased to the initial value. This procedure is repeated several times, where the waiting time for pressure saturation of each step decrease from one hour to a few minutes, until the needle valve is completely open. Then it is safe to switch on the turbo-molecular pump. This method is proven to leave the nanofibre transmission unchanged and thus the waist unharmed. When a pressure of $1 - 2 \times 10^{-8}$ mbar is reached the ion pump can be switched on and the valve between turbo pump and experiment chamber can be closed. From this point on a stable nanofibre experiment is possible.

9.2. Magnetic field configuration for a mirror-MOT

The first stage to obtain ultra-cold atoms is the magneto-optical trap [48], where a local Zeeman shift of the atomic transition provided by a quadrupolar magnetic field in combination with a polarised strong laser field produces a position dependent radiation pressure pushing the rubidium atoms towards the trap centre. For a full confinement of the atoms the MOT laser beams are shone onto the atoms from all six spatial directions, which can be easily achieved with six straight beams for a free standing experiment. In an experiment with atoms close to a surface is performed here, this configuration is not possible and it is necessary to make the surface - at least partly - reflective in order to create a mirror MOT, see a rigorous description in [68]. Here one straight beam pair in parallel to the surface is left as in the six-beam MOT. The other directions are covered by another counter-propagating beam pair shone onto the surface mirror under 45 °. Thus the remaining spatial directions are covered by both the two incoming beams and their reflections, respectively. This works only for a large beam width in order to have a large overlap area between the beam and its reflection. The volume of the quadrupole

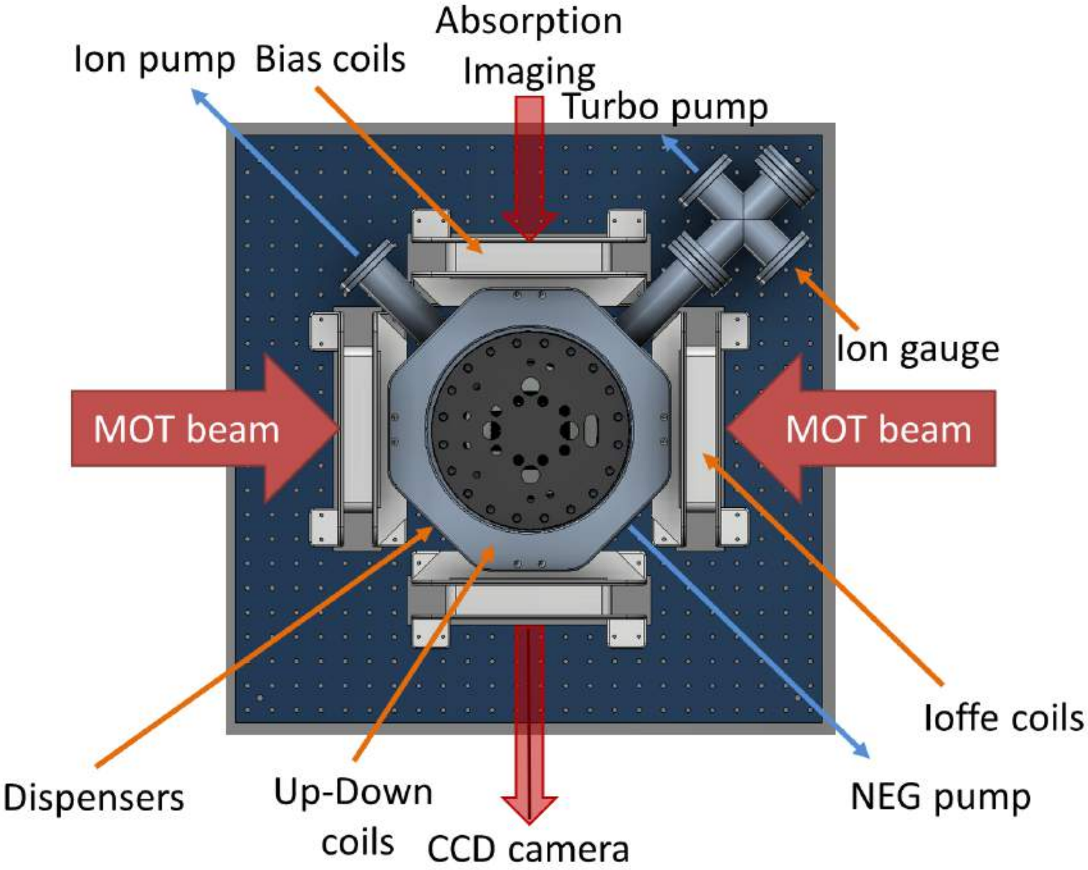

Figure 9.3.: Top view of the vacuum chamber.

magnetic field thus has to be matched to height of the triangular shaped region under the mirror being determined by the beam width of $\approx 1\,''$ in this experiment. A second design peculiarity comes from the fact that the inhomogeneous part of the magnetic field is produced by a solid copper structure between mirror and chip mount, whereas the external coils are connected in Helmholtz configuration, hence providing a homogeneous field to break the symmetry of the copper structure's field. This structure is H-shaped with a height of 1 mm, the width of the side bars is 5 mm and of the central bar is 10 mm. The distance between the inner edges of the side bars is 20 mm (see B.5).
Simulations of the initial MOT (Figure 9.4) show that the trap centre is at a distance of 2.3 mm underneath the chip. The field gradients are on the order of 50 G/cm in the transversal directions and ≈ 10 G/cm in the longitudinal direction.

9.2.1. Coils

The experiment contains three Helmholtz coil pairs (see [47] for an excellent guideline for coils design) covering all spatial directions, where the two horizontal ones (B.1) are almost rectangular to better fulfil the Helmholtz condition at the distances given by the

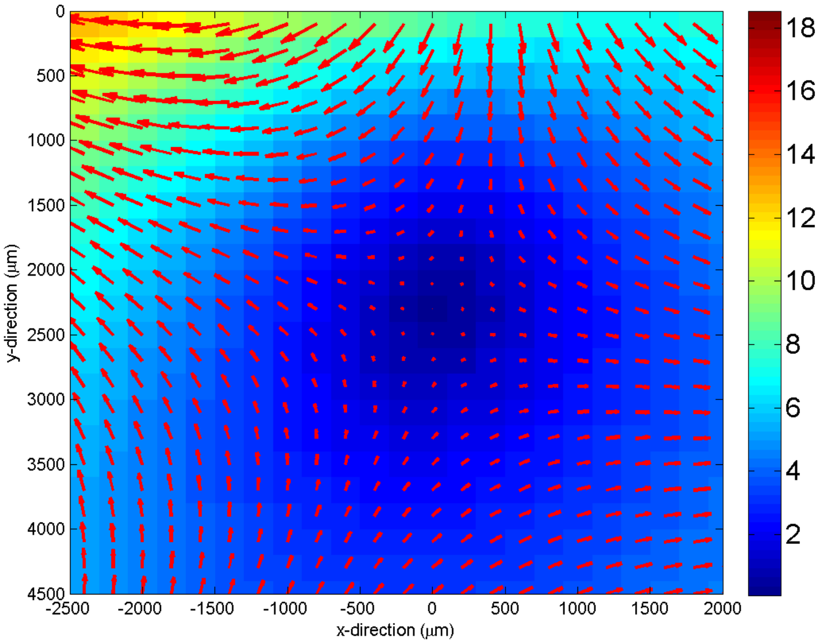

Figure 9.4.: Cross section of the magnetic field of the initial mirror MOT in the two directions perpendicular to the central bar of the copper-H structure at the field minimum along the bar. The point $(x, y) = (0, 0)$ corresponds to the bottom right corner of the copper bar's cross section. Thus the trap centre is situated 2.3 mm under the central copper structure.

diameter of the vacuum system, see the positions of the coils relative to the chamber in Figure 9.3. Also it was desired to have good optical access from all directions, excluding designs involving touching coils at the corners which would lead to a large obstruction of the windows situated at 45°. The coil pair in the vertical direction (B.2) is an almost perfect Helmholtz configuration, with the additional advantage of an easily removable top coil. Since the experiment flange is only covered by the latter it is quite easy to change the experimental configuration by replacing the setup mounted on the flange and closing the vacuum chamber again. The horizontal coils have ≈ 80 windings of a coated copper wire with a circular cross section of 3 mm diameter. This produces a field of up to ≈ 55 G in the centre of the vacuum chamber - the desired position of the MOT. The vertical coils have ≈ 90 windings of a 2 mm diameter coated copper wire also with circular cross section. These produce a limiting field of ≈ 40 G in the centre. The wires were attached to the coil mount with a silicon based glue[7].

---

[7] a warning to all the experimenters out there: don't use Stycast if you don't have to, there are plenty of other options not ruining your lungs and clothes.

9.3. Laser system

The laser system for the MOT is in principle the same as in the micro-optics experiment, see [69],[32] and [59]. The main change was the replacement of the repump external cavity diode laser (ECDL) by a distributed feedback (DFB) laser, providing a more stable lock and smaller casing[8] making room for more beam shaping optics. Also the cooling laser system had to be replaced due to ageing of the - both homebuilt - seeding laser and tapered amplifier by company-manufactured laser systems . The four lasers in use are described in the following, see also Figure9.5. First there is the **master** laser acting as a frequency reference for the cooler and imaging lasers. The master laser itself is frequency-modulation (FM) locked to the $F = 2 \rightarrow F' = 2/F' = 3$ crossover in the Doppler-free saturation spectrum of a rubidium cell. This homebuilt ECDL is also used as a frequency reference for the nanofibre cavity, which is locked to the light after it is frequency shifted with an acousto-optic modulator by -133.3 MHz to be resonant with the $F = 2 \rightarrow F' = 2$ transition. This is done to keep the cavity off-resonant with respect to the MOT lasers during the cooling phase.

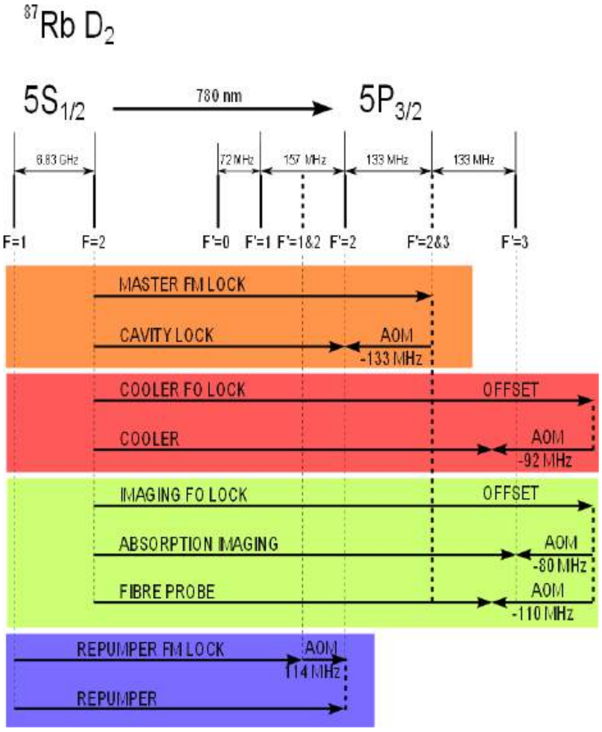

Figure 9.5.: Frequencies of the four lasers in use. The cooling and imaging laser is frequency-offset locked to the master laser, which is also used to lock the nanofibre cavity during the experiment, when no measurement using the fibre probe beam is done.

The **cooler** laser is frequency-offset (FO) locked to the master laser which allows large frequency tunability during the running experiment. The cooler is a commercial ECDL which seeds a tapered amplifier[9] with an output power of more than 300 mW going into the vacuum chamber. The frequency is shifted by -92 MHz, with an AOM mainly used as fast switch and as a control of the light intensity. The cooler light is usually red detuned by ≈ 15 MHz with respect to the cycling $F = 2 \rightarrow F' = 3$ transition.

The **imaging** laser - another homebuilt ECDL - is FO locked to the master laser in the same manner as the cooler and is used for two different purposes: first as a light source for **absorption imaging**, where the light beam is controlled by an AOM with a frequency shift of -80.7 MHz, and second, it is used as the **fibre probe** laser for the measurements involving cavity transmission and reflection. This laser is controlled by

---

[8] Thorlabs LDM21 Laser Diode Mount

[9] Toptica: DL pro and BoosTA

another AOM with a shift of -110.7 MHz.
Finally there is the **repumper** laser coupling the $F = 1$ and $F' = 2$ state to pump $F = 1$ atoms back to the cycling cooler transition. This DFB laser[10] is FM locked to the $F = 1 \rightarrow F' = 1/F' = 2$ crossover peak in the Doppler-free saturation spectrum in another rubidium cell and shifted by 114.7 MHz into resonance with the $F = 1 \rightarrow F' = 2$ transition with an AOM.

---

[10] Eagleyard photonics: Distributed Feedback Laser: EYP-DFB-0780-00080-1500-SOT02-00000

10. Coupling a MOT to a nanofibre

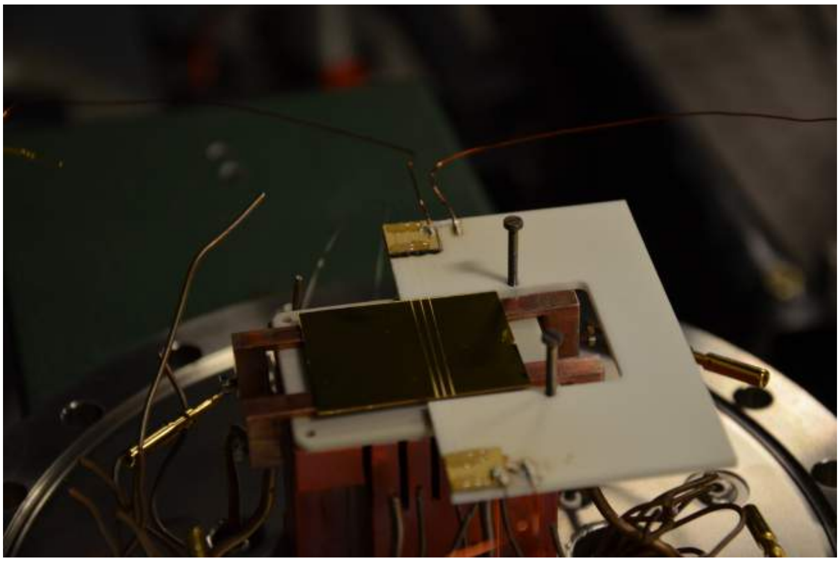

Figure 10.1.: Mount for the nanofibre experiment. On top of the solid copper block lies an insulating AlN subchip (gray), on top of which an H-shaped copper structure is glued, which provides the inhomogeneous magnetic field in the MOT. On top is a gold coated silicon wafer, which acts as a mirror for the MOT beams. The white U-shaped fibre holder is machined from Macor. On top of the yellow squared piezo actuators, which are mounted for testing their feasibility, are three nanofibres glued with a UV cured epoxy. All three fibres where tested in the experiment and the MOT atoms cold be magnetically transferred to all of them, which was demonstrated by attenuation of the transmitted light through the fibres.

Before the nanofibre experiment including the Fabry-Perot cavity was performed, a test of the mounting procedure close to the surface of the gold mirror was done with the help of a bare nanofibre. This also acted as a reference for the coupling strength in comparison with that of the cavity fibre. After a brief summary of the experimental cycle 10.1) the absorption of the transmitted light is discussed and related to the geometry and temperature of the MOT (10.2).

10.1. Experimental procedure

The preparation of the atomic ensemble is described as the following, see also Figure 10.2 for a sketch of the relevant timings. Rubidium atoms are evaporated into the vacuum chamber by pulsing two dispensing wires for a few seconds and the atoms are immediately

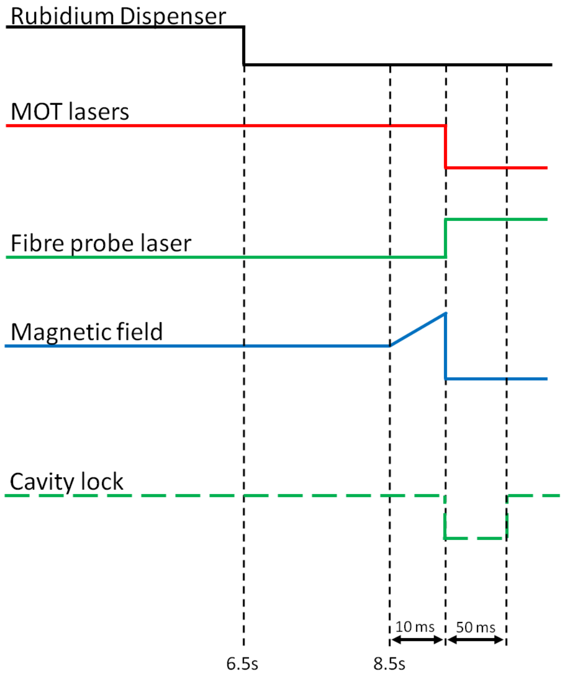

Figure 10.2: Experimental cycle: In the first 6.5 s the rubidium dispensing wires are pulsed. At the same time the cooling and repump laser as well as the magnetic fields are switched on, to immediately accumulate atoms in the MOT. After an additional waiting time of 2 s during which the atom number in the MOT saturates at $\approx 2 * 10^7$, the MOT position is ramped towards the nanofibre by increasing the magnetic field within 10 ms to its final value. Then the MOT lasers and the magnetic field are switched off and the fibre probe laser excites atoms passing the nanofibre and the transmission and reflection is detected with an SPCM. In the cavity experiment (see 11) additionally the timing of the frequency stabilisation is important. Since the Bragg mirrors are very narrow, the cavity is locked with a laser close to the atomic resonance, which would interfere with the measurements in the cavity. Therefore the cavity lock is switched off during the measurement.

confined in the minimum of a magnetic quadrupole field (see section 9.2), where also the MOT laser beams intersect, approximately 5 mm below the mirror surface and the nanofibre. In this MOT, $\approx 2 \times 10^7$ atoms are collected and cooled down to $\approx 100\ \mu$K. As soon as the atom number has saturated, the MOT position is rapidly shifted towards the nanofibre within 10 ms. Then both MOT lasers and the magnetic field are switched off and the probe laser is shone through the nanofibre. The atoms arrive within a few milliseconds at the nanofibre and a drop in the transmission through the fibre is detected with a single photon counting module [1]. The timing of the signal is given by the final position of the magnetic field.

---

[1] PerkinElmer SPCM-AQR-12-FC

10.2. Coupling a MOT to a standard nanofibre

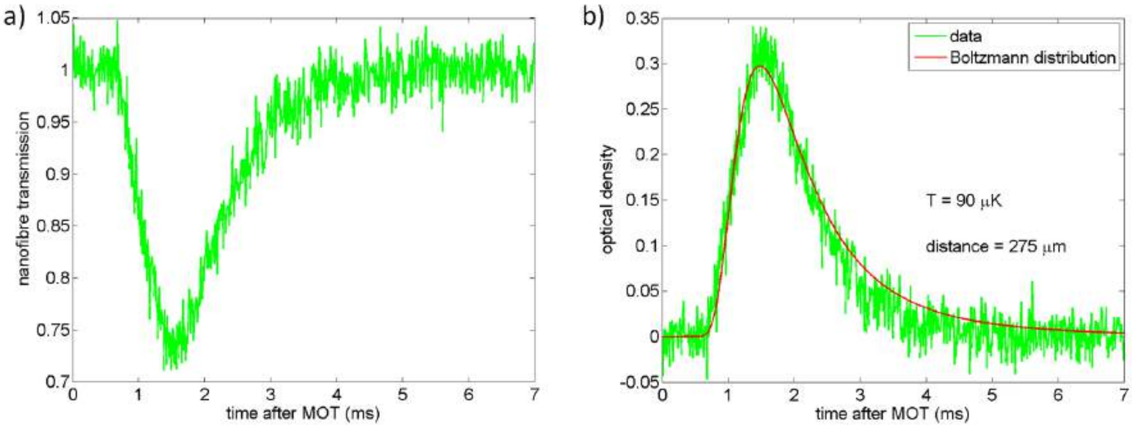

Figure 10.3.: a): Transmission through the nanofibre after the MOT is ramped towards its position. The atoms pass the fibre within a few ms leading to an attenuation of the transmitted resonant light by ≈ 30 %. The depth and shape of the signal depends on the end position of the MOT. **b)**: The attenuation can be directly converted to a time-dependent optical density. As a guide to the eye a 3d Boltzmann distribution is plotted (red), assuming a distance of 275 μm between the final MOT position and the fibre and a temperature of 90 μK. The agreement seems to imply that the atoms are thermally expanding to the fibre, from a position close to the fibre. In the discussed thermal distribution no centre-of-mass velocity has been considered, thus the determined temperature is an upper estimate.

The transmitted power through the fibre P_{tr} is measured (see Figure 10.3) and the attenuation of the incoming light power P_{in} is described by the optical density

$$OD = -\ln\frac{P_{tr}}{P_{in}}. \tag{10.1}$$

The integrated counts in the detector give a time dependent optical density proportional to the arrival rate of atoms at the fibre, with the proportionality factor $4C_1 = OD/N$ being the single atom free space cooparativity. The signal shape can be described by a 3d Boltzmann distribution (its 1d version has been already introduced in 2.3.1)

$$OD(t)dt = 4C_1N(t)dt = 4\pi OD_{int}\left(\frac{m}{2k_BT}\right)^{3/2}\frac{d^2}{t^2}\exp^{-\frac{md^2}{2k_BTt^2}}dt, \tag{10.2}$$

with an integrated optical density OD_{int} and a distance d between the final MOT position and the nanofibre. As can be seen in Figure 10.3, the temperature of 90 μK is of the same order as measured with absorption imaging in time-of-flight. The distance between MOT and nanofibre has to be on the order of a few hundred micrometers in order to achieve a significant signal since the atomic density decreases with the distance squared. The distance can be controlled by changing the position of the magnetic field minimum. Then different signal shapes for the transmission are measured, see Figure 10.4.

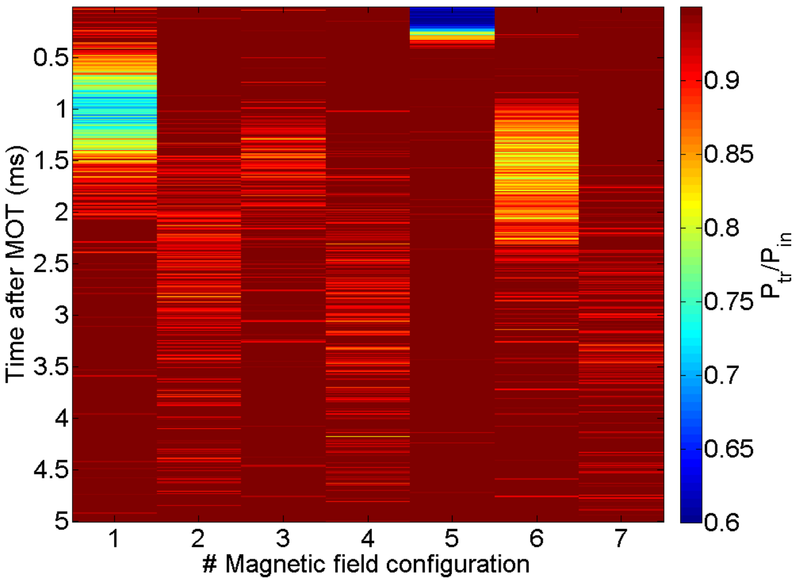

Figure 10.4.: Nanofibre transmission (colour scale) for different end positions of the magnetic quadrupole. The closer the MOT is transported to the nanofibre position before switching off the MOT fields and lasers the larger is the absorption corresponding to a higher atomic density at the fibre. Configuration no. 1 is discussed in Figure 10.3. Also of interest is no. 5, where the MOT position is directly at the nanofibre, where the transmission seems to reach a lower plateau of $(P_{tr}/P_{in}) \approx 0.6$.

11. A nanofibre Fabry-Perot resonator

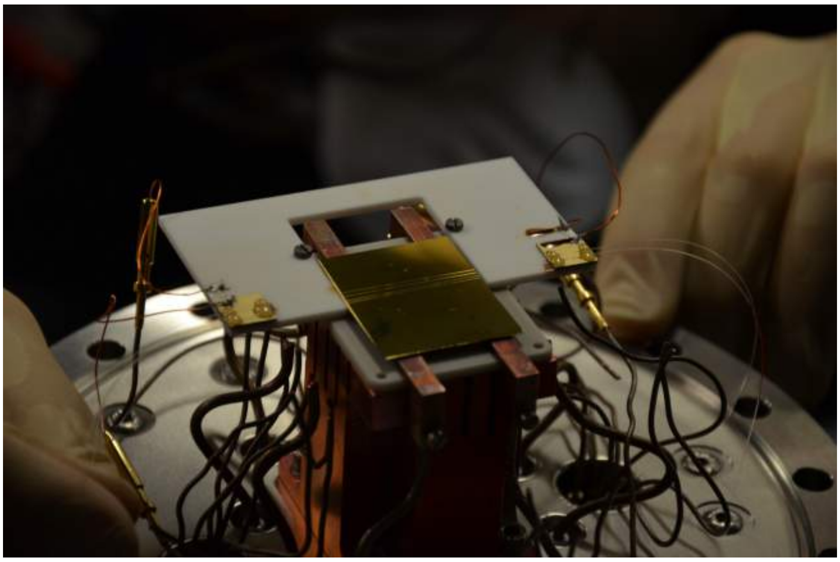

Figure 11.1.: The experiment mount loaded with the cavity nanofibre (bottom) and a bare reference fibre (top).

The first goal of the nanofibre cavity experiment was to test all the steps of its assembly without destroying it, and the second goal was to see the effect of the atoms on the cavity signal. The standard single-mode fibres with written-in Bragg mirror pairs were tested before pulling to the diameter of the final nanofibre waist (11.1). A similar characterisation was performed for the built-in fibre with the nano-waist (11.2) and then the change in the transmission spectrum due to the presence of MOT atoms was analysed (11.3).

11.1. Characterisation of nanofibre Bragg mirror Fabry-Perot cavities

The Bragg mirrors are laser-written into commercial single mode fibres in the following way [42]. An interference pattern of a UV laser is produced by splitting it into two beams and by recombining them under a certain angle, which defines the spacing of the grating. The illumination of the fibre with this spatial intensity modulation creates a location dependent shift of its refractive index, thus forming a periodic structure. The creation of such a mirror is challenging because the temperature of the sample has to be stabilised well during the writing process. Thus a sample of many fibres was produced at the group of Manfred Rothhardt at the Institute of Photonic Technology in Jena, where the spectral overlap of the two mirrors (see fig. 11.2) and the coincidence of their active wavelengths with the rubidium D2 line had to be tested.

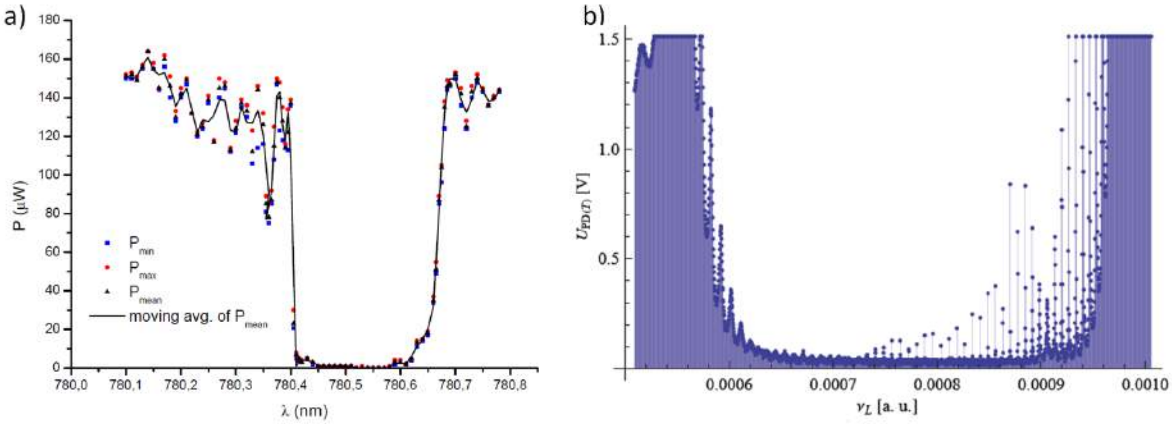

Figure 11.2.: a) Coarse transmission spectrum of a DFB laser through a fibre with two Bragg mirrors before being pulled to a nanofibre. The Bragg condition for the individual mirrors implies a spectral window of ≈ 0.3 nm of a large reflectivity. Outside of this window the usual fibre transmission is unaltered. It is a challenge to write two mirrors with a good spectral overlap. Only then both mirrors also form a Fabry-Perot resonator. **b)** By going to larger spectral resolution it is possible to observe the individual resonances.

The measurable properties of the Fabry-Perot resonator are its finesse and the two contrasts of the reflected light from both sides. The finesse is defined as the ratio of the free spectral range (FSR) and the FHWM linewidth $FSR/\delta\nu$ and it is solely related to the optical properties of the cavity via eq. 3.26

$$\mathcal{F} = \frac{\pi\sqrt{g_{rt}}}{1 - g_{rt}} \tag{3.26}$$

with the round trip gain $g_{rt} = r_1 r_2 t_{rt}$, defined in 3.3.1. The reflection contrasts are defined using eq. 3.30 on resonance

$$\mathcal{C}_i = \min\left(\frac{E^i_{ref}}{E^i_{in}}\right) = \frac{r_i - g_{rt}/r_i}{1 - g_{rt}}, \tag{11.1}$$

where the mirror with the index i is the input mirror of the cavity. This is a quadratic equation which can be used to solve for r_i, with the additional knowledge of g_{rt} obtained from eq. 3.26. Note that, since only the reflected light intensities are measurable, one only has access to the absolute squares of the contrasts.

11.2. Characterisation of the built-in Fibre cavity

After a successful selection of the best suitable mirrored fibres, the pulling to the nanofibre diameter, the mounting thereof on top of the piezo actuators and insertion into the vacuum system, the only nanofibre cavity surviving this treatment was characterised again because the pulling procedure increases the distance between the mirror from 20 mm to 60 mm which alters the FSR and, in combination with possible contamination of the fibre surface, the absorption along the waist and the taper. This was done by measuring the nanofibre spectrum. A description of the mechanical oscillation of the fibre is also given.

11.2.1. Cavity transmission spectrum

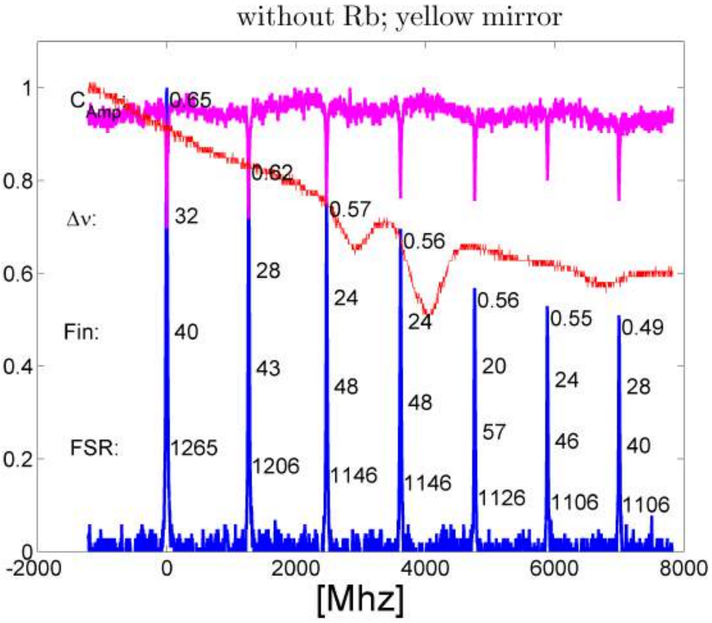

Figure 11.3.: Spectrum of the built in nanofibre with the Bragg mirror cavity in transmission (blue) and reflection (pink). As reference the absorption spectrum of the rubidium D2 line is measured (red). The individual resonances are characterised by their FWHM linewidths $\Delta\nu$, the free spectral range (FSR), from which the cavity finesse (Fin) can be derived. From the latter and the contrast C_{amp} of the reflected signal the mirror reflectivities can be estimated.

After the pulling the fibre to its final taper profile the properties of the resonator are changed, because the length of the cavity is larger. By tuning the current of a DFB laser a coarse spectrum of the built-in fibre has been measured and compared to the rubidium spectroscopy and also to a calibrated Fabry-Perot interferometer (fig. 11.3). By taking finer transmission spectra with the cavity probe laser for different piezo voltages, defining its length, the cavity linewidth can be obtained by a Lorentz fit, see fig. 11.4. The cavity linewidth $\kappa = 2\pi \times \delta\nu_{HWHM}$ was found to be $2\pi \times 10.4 \pm 2.7$ MHz. Since the free spectral range obtained from the coarse measurement was found to be 1.1 GHz, the cavity finesse is 53 ± 10.

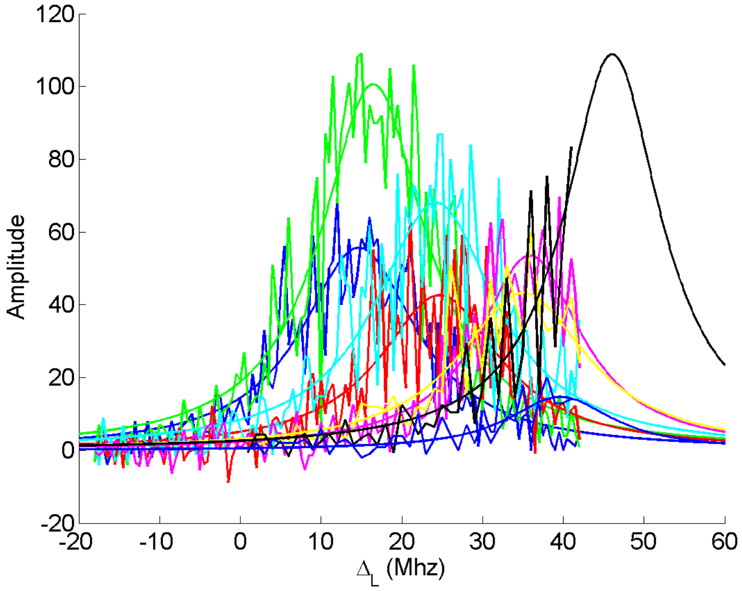

Figure 11.4.: Transmission spectra of the built-in cavity for different piezo voltages and the corresponding Lorentz fits.

The reflection contrasts for the chosen interference peak are $\mathcal{C}_1 = 0.76$ and $\mathcal{C}_2 = 0.6$. Using eq. 3.26 and 11.1 from the last section the reflectivities of $R_1 = r_1^2 = 98.59$ % and $R_2 = r_2^2 = 90.95$ % for the two Bragg mirrors and a round trip transmission $T_{rt} = t_{rt}^2 = 99.06$ % have been found.

11.2.2. Fibre oscillations

"Eppur si muove "(Galileo Galilei)

The nanofibre shows characteristic mechanical oscillations if excited, resulting in a corresponding oscillation of the transmitted power through the cavity. The most prominent modes of fibre oscillation are at frequencies ≈ 300 Hz, ≈ 600 Hz, and ≈ 1200 Hz, the latter usually showing the largest amplitude. These oscillations on the fibre transmission were already observable during the acceleration phase of the turbo-molecular pump at the corresponding rotation frequencies. In the experiment the fibre is excited due to the rapid switch-off of the current through the large coils providing the magnetic field for the MOT. The energy stored in the magnetic field is transferred into mechanical energy within a few milliseconds, as can be seen in fig. 11.5. The optical length of the cavity oscillates correspondingly and thus also the transmission spectrum of the light. The oscillation spectrum can be obtained from the Fourier transform along the time-axis of the transmission spectrum, see fig. 11.6.

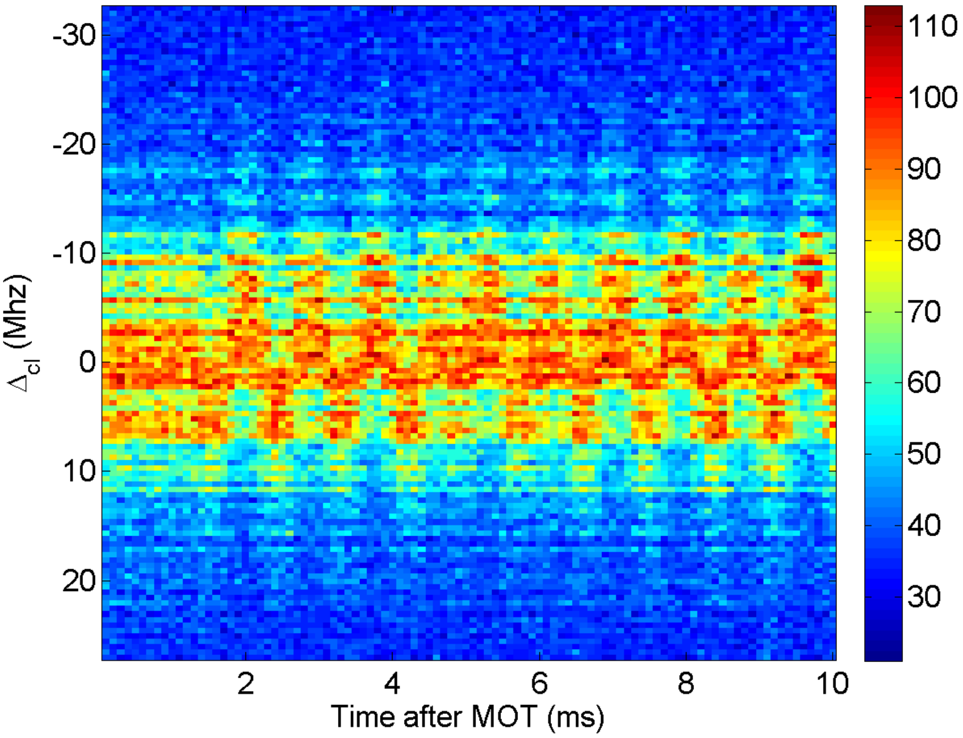

Figure 11.5.: Spectrum of transmitted light through the nanofibre resonator versus time after the MOT phase. The switch-off of the MOT fields at $t = 0$ induces a mechanical vibration of the fibre, which is also visible on the transmitted light. The colour scale is given by detected photon counts per time bin of 100 μs.

In order to gain insight into the behaviour of the light transmission spectrum through the cavity, independent of the current phase of the fibre oscillation, the rest position of the optical length of the cavity has to be found. This is done by choosing 1.2 kHz as a representative frequency and fitting the derivative of a Lorentzian

$$A(\Delta_{cl}) = A_0 \frac{\Delta_{cl}}{\left(1 + \frac{\Delta_{cl}^2}{\kappa^2}\right)^2} \tag{11.2}$$

to the real part of the Fourier transform (see Figure 11.7) for this particular frequency. Besides the detuning $\Delta_{cl} = \omega_l - \omega_c$ between the laser and the cavity resonance frequency at the mechanical centre position a measure for the cavity linewidth $\kappa \approx 2\pi \times 9.5$ MHz is found. Performing this procedure for different lengths of the cavity, set by changing the voltage of the shear piezos, a calibration for the cavity detuning relative to the light frequency can be derived, see Figure 11.7. Since the experimentally relevant frequency range is small compared to the full piezo stroke a linear relation between cavity length and piezo drive voltage can be assumed for a fit.

As already mentioned it takes more than 1 ms for the oscillation to start after switching

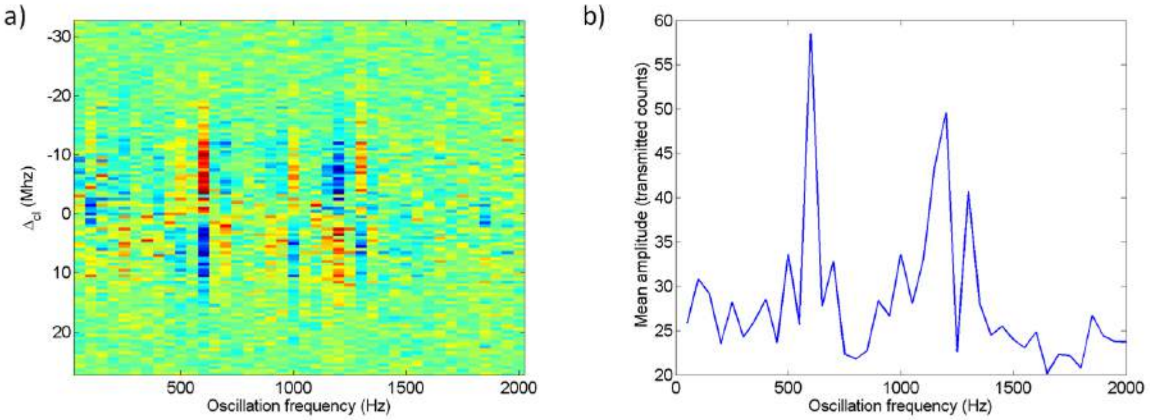

Figure 11.6.: a) Real part of the Fourier transform of the transmission spectrum. **b)** Mean spectrum of the of the observed oscillation, which are twice the frequency of the mechanical fibre oscillation.

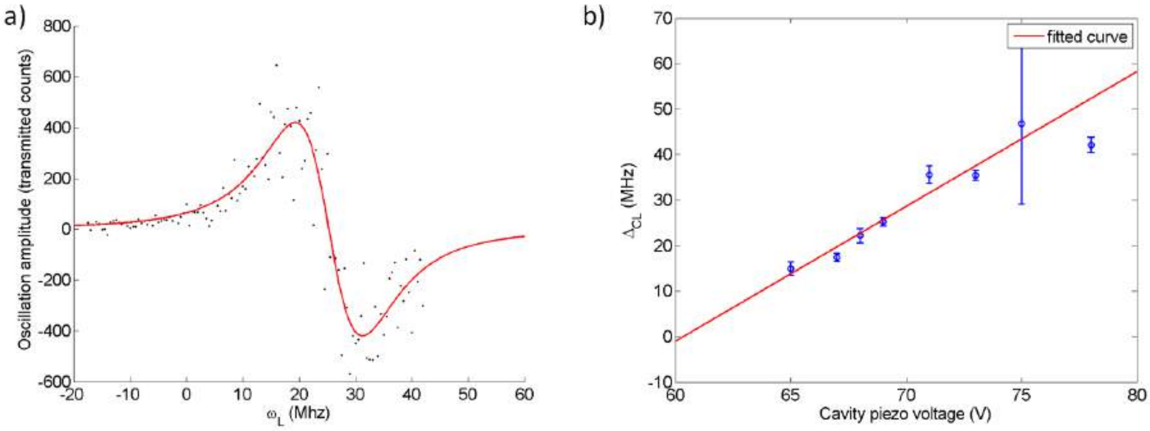

Figure 11.7.: a) Real part of the oscillation spectrum versus laser detuning for the mode with ≈ 1.2 kHz. The behaviour corresponds to the derivative of a Lorentzian and is fitted to determine the cavity-laser detuning. **b)** Cavity-laser detuning versus cavity piezo drive voltage. The linear fit results in a slope of ≈ 300 MHz/V

off the MOT, as can be seen in Figure 11.5. The atoms from the MOT would mainly arrive in this time period without mechanical excitation (see next chapter), as can be also understood quantitatively by comparing the frequency calibration with the direct Lorentz fit of the empty cavity at the times where the atoms would arrive at the fibre (see Figure 11.8). Thus it is possible to use the mechanical oscillation, after all the atoms have passed the nanofibre region, as a calibration of the cavity frequency instead of taking additional empty shots.

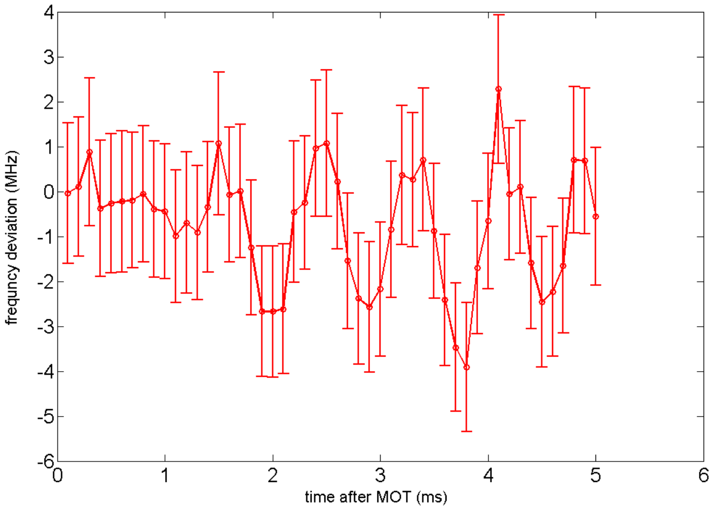

Figure 11.8.: Deviation of the cavity resonance frequency, due to mechanical oscillations of the fibre measured for the first 5 ms after switching off all the coils, from the cavity resonance at rest, measured by fitting a Lorentzian to the cavity spectrum when the fibre oscillation is gone. It can be observed, that there is almost no oscillation in the first ≈ 1.5 ms, where most of the atoms arrive.

11.3. Coupling a MOT to a Fabry-Perot resonator

11.3.1. Experimental procedure

The preparation of the atomic ensemble is almost identical to case with the bare nanofibre in the previous chapter (see timing sketch of the cavity cycle in Figure 10.2). The only difference is the stabilisation of the cavity during the cycle. This is done by locking the cavity to a resonant laser which is FM locked to an atomic transition. As soon as the atom number has saturated the MOT position is rapidly shifted towards the nanofibre within 10 ms and the cavity resonance frequency is ramped from its lock value to the desired frequency. Then both MOT lasers and magnetic fields are switched off and the cavity probe laser is shone through the nanofibre. The atoms arrive in the first two milliseconds at the nanofibre and the coupling between them and the cavity can be determined by counting transmitted photons with (Figure 11.9) and without (Figure 11.5) atoms with a single photon counting module for different probe laser frequencies and cavity detunings.

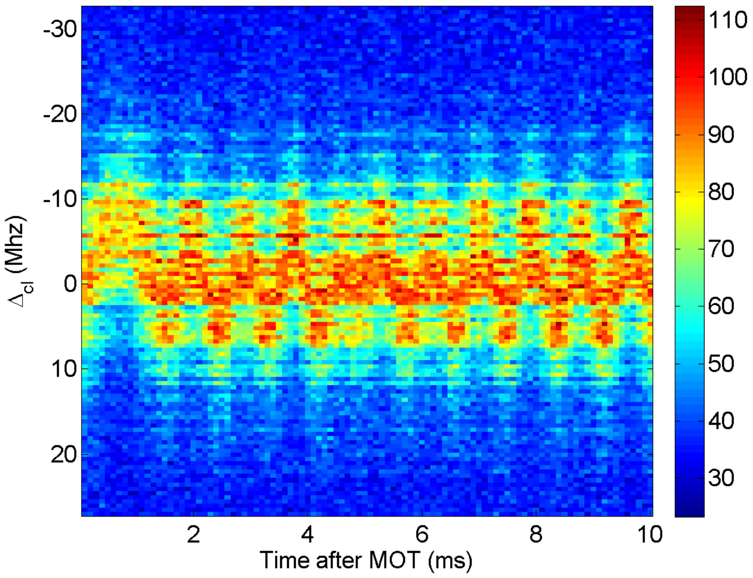

Figure 11.9.: Detected counts of light transmitted through the nanofibre resonator versus the time after the MOT phase and the cavity-laser detuning Δ_{cl} for fixed cavity length. The atoms are magnetically transported to the position of the nanofibre waist, altering the spectrum in the first 2 ms. The colour scale is detected photon counts per time bin of 100 μs.

11.3.2. Cavity transmission spectrum

In order to correct for the fibre oscillation 5 background measurements without atoms are always taken, and subtracted from the mean of 15 measurements with atoms. As can be seen in Figure 11.10, the remaining features are a combination of a dispersive shift for the positive and absorption for the negative values induced by atoms present in the vicinity of the nanofibre waist. For a certain cavity resonance frequency and time after the MOT, that means by taking a slice through Figure 11.10 at a distinct time, one can look at the transmission spectrum and compare it to the oscillator model:

$$\left(\frac{P_{tr}}{P_{in}}\right) = \frac{1}{\left(1 + 2C\mathcal{L}_a(\Delta_{la})\right)^2 + \left(\frac{\Delta_{cl}}{\kappa} + 2C\mathcal{L}_d(\Delta_{la})\right)^2}. \tag{3.33}$$

This fit is done for all time slices of 100 μs for the first 5 ms after the MOT phase. From each fit the cooperativity C is determined and a temporal dependence can be observed in Figure 11.11 with a maximum value of $C = 6.6$, but due to the small number of experimental repeats per frequency so far the error is still too large to give more than an estimation of the order of magnitude. Also, the fit is performed with the atomic linewidth fixed at the natural linewidth. A more elaborated analysis, which takes care

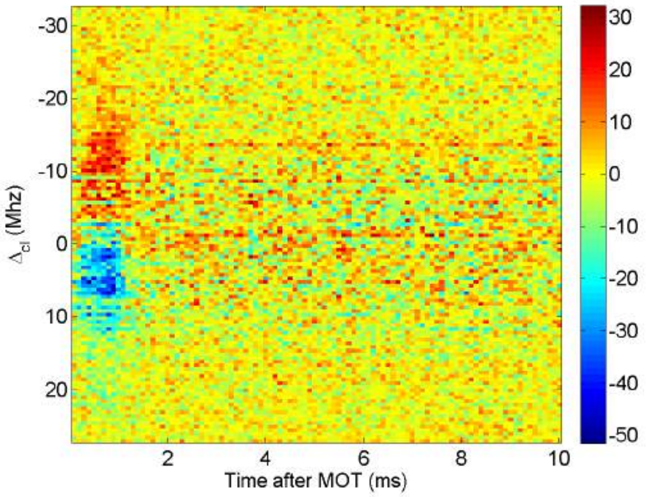

Figure 11.10.: Difference of detected counts with and without atoms versus time after the MOT phase and cavity-laser detuning Δ_{cl}. The colour scale is the difference of detected photon counts per time bin of 100 μs.

of the large inhomogeneous broadening, has to be performed as soon as a more exact value of the broadening is determined (see also the discussion in the next section).

11.3.3. Shift of the cavity resonance frequency

In order to get some insight in the effect of the atoms on the cavity transmission the shift of the cavity resonance frequency due to the presence of the atoms can be measured. This is a good strategy for this first phase of the experiment, where the atom-cavity detuning as well as the inhomogeneous broadening is not known. Thus most measurements are done with a detuning larger than the cavity linewidth and additionally as already indicated in the previous section there seems to be a large broadening, much larger than the cavity linewidth. Then the absorption of the atoms is constant over a large frequency range on the order of atomic linewidth. Thus it seems more significant to look at the shift of the cavity resonance frequency, which can be understood as change in the refractive index depending on the atomic density within the resonator mirrors. The frequency shift of the cavity resonance $\delta\omega_c$ is obtained by a Lorentz fit to the transmission spectrum through the cavity with atoms and comparing it to the spectrum of the empty cavity. This is done for several atom-cavity detunings as can be seen in Figure 11.13.

It can be observed that there is a linear relation between the resonance shift and its position in the spectrum. This can be understood as follows: For the description of the cavity transmission the oscillator model is used, where the atomic linewidth γ is simply replaced by an inhomogeneous broadening γ_{inh}, which is a rather crude model. Assuming γ_{inh} large compared to the range of the offset-locked laser and hence the laser-atom detuning, the absorptive Lorentzian $\mathcal{L}_a$ remains almost constant at 1 and eq. 3.33

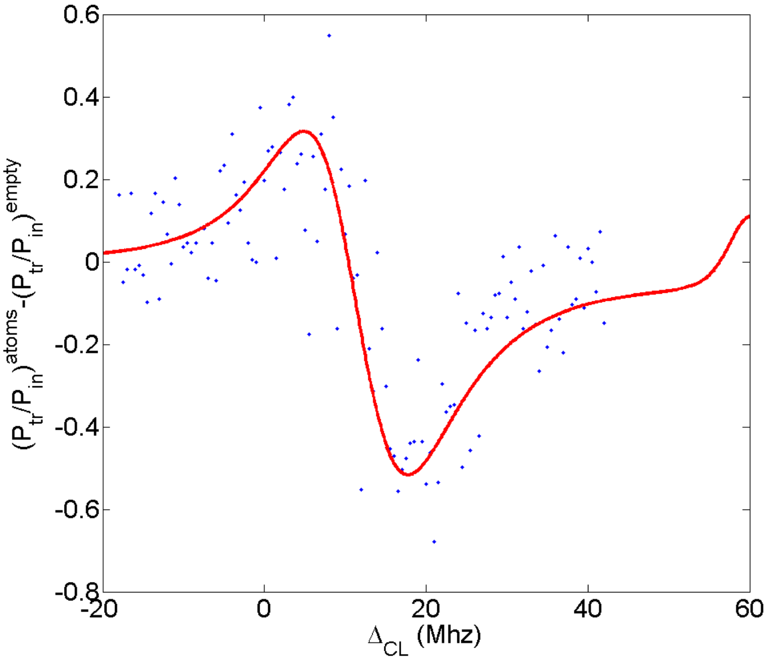

Figure 11.11.: Difference of the measured transmission with and without atoms respectively in a time slice 600 μs after the MOT phase. The fit is the transmission with (eq. 3.33) minus a Lorentzian for the empty cavity. This fit is done with the atomic linewidth fixed at its natural value leaving the cooperativity C as relevant fit parameter. This is further discussed in Figure 11.12.

can be approximated to

$$\left(\frac{P_{tr}}{P_{in}}\right) \approx \frac{1}{(1+2C)^2 + \left(\frac{\Delta_{cl}}{\kappa} + 2C\mathcal{L}_d\right)^2} =: \frac{1}{(1+2C)^2}\frac{1}{1+\frac{\Delta'^2}{\kappa'^2}}, \tag{11.3}$$

which is again an effective Lorentzian with a new shifted cavity detuning $\Delta' = \Delta_{cl} + 2C\kappa\mathcal{L}_d$ and a new effective cavity linewidth $\kappa' = \kappa(1+2C)$. Thus the frequency shift is

$$\delta\omega_c = 2C\kappa\mathcal{L}_d, \tag{11.4}$$

which, in case of a large inhomogeneous broadening $\Delta_{la} \ll \gamma_{inh}$ of the atomic linewidth, can be linearised to

$$\delta\omega_c = -2C\kappa\frac{\Delta_{la}}{\gamma_{inh}}. \tag{11.5}$$

This linear relation can be fitted to different cavity detunings and its slope is proportional to the cooperativity. Since the inhomogeneous broadening is not known yet, only the ratio C/γ_{inh} can be obtained by this method. In Figure 11.14 this ratio times the natural linewidth is plotted for different arrival times and thus atomic densities. The shape of the signal looks very similar to that of the optical density measured without

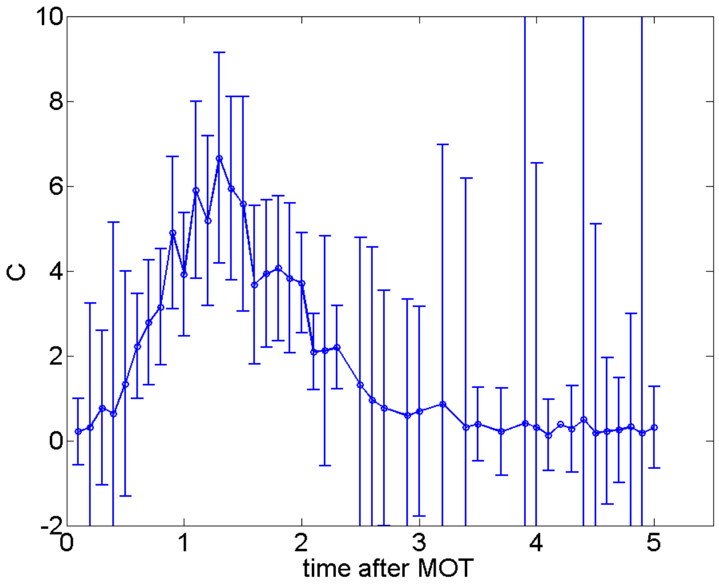

Figure 11.12.: The cooperativity C obtained from the fit described in Figure 11.11 for different times after the MOT phase. The error bars correspond to the a fit confidence of 1σ.

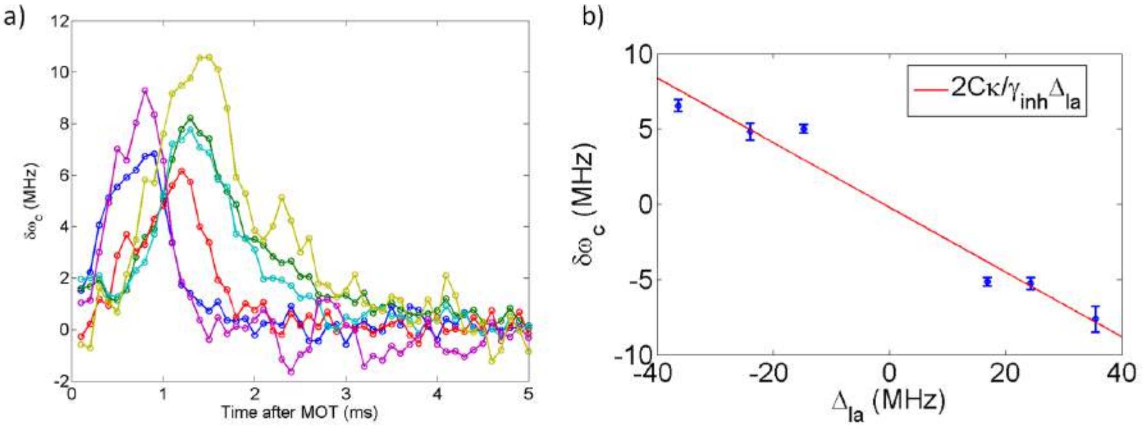

Figure 11.13.: **a)**: Shift $\delta\omega_c$ of the cavity resonance frequency versus time after the MOT phase, determined by Lorentz fits to the transmission spectra with and without atoms respectively. The colour corresponds to different cavity detunings. **b)**: Frequency shift of the cavity resonance versus laser detuning. The cavity is detuned from atomic resonance, thus a linear relation between shift and laser detuning can be assumed. The slope of a linear fit is related to the cooperativity C, the cavity and inhomogeneously broadened atomic linewidth κ and γ_{inh}, respectively. This fit is done for every time slice, assuming an approximately constant mean atomic density within each time bin.

the resonator (see Figure 10.3). A comparison of both signals gives a measure for the inhomogeneous broadening as the coupling to the cavity nanofibre should be at least the same as for the bare one. The peak cooperativity of the bare fibre is $OD/4 \approx 0.08$ and

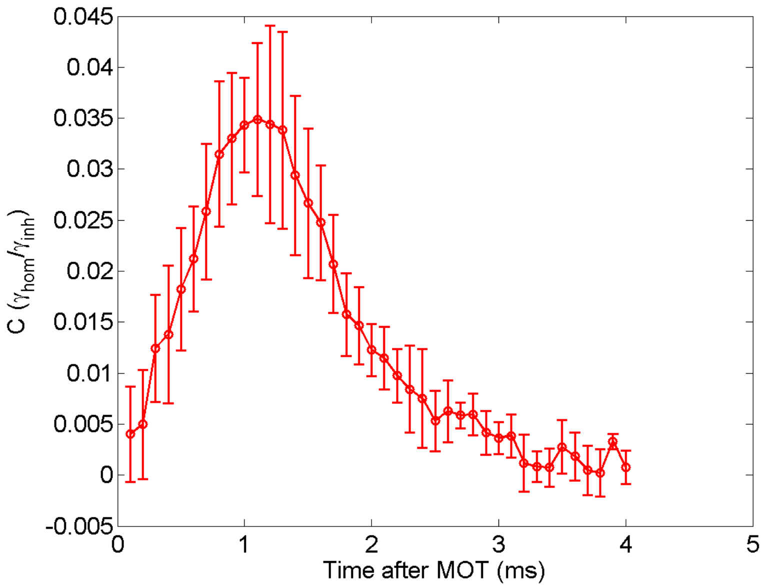

Figure 11.14.: Estimate for the cooperativity C versus arrival time after the MOT phase. C is corrected for the unknown inhomogeneous broadening γ_{inh}. This is a lower bound for the cooperativity because it increases by the ratio $\gamma_{inh}/\gamma_{hom}$.

the peak in the weighted resonator cooperativity is $C(\gamma_{hom}/\gamma_{inh}) \approx 0.04$. This sets a lower estimate for γ_{inh} to $2\gamma_{hom}$, which would be still smaller than the cavity linewidth. On the other hand, the experimental results, for example the linear behaviour for the cavity resonance shift, suggest that the former is considerably larger than the latter, indicating that the cooperativity has to be larger in the cavity by some factor on the order of $5 - 10$ compared to that in the bare nanofibre. Thus a lower estimate for the cooperativity of ≈ 0.5 can be given with this method which is one order of magnitude smaller than the measured value in the previous paragraph. There is an ambiguity for the inhomogeneously broadened signal, since the profile looks quite similar for different values of C and γ_{inh} as long as their ratio is nearly constant. This can be resolved by measuring the inhomogeneous broadening without the cavity.

12. Nanofibre cavity experiment: Results

A brief summary of the results so far of the nanofibre experiment is given from both a technological as-well-as a physics point-of-view and a small outlook is given about the next experimental steps in order to improve the performance of the existing components and increase the experiment's versatility by adding an atom chip.

12.1. Results

Technology

The main accomplishment of the nanofibre cavity experiment within this thesis was building the actual setup and understanding of the different steps during the design and building process, from getting the right sizes of vacuum pumps to trying to fit in coils and MOT beams into the setup. The most challenging part of the assembly is the mounting of the fibre holder onto the experiment flange and achieving vacuum without contaminating the nanofibre waist with dirt, which would lead to strong heating of the fibre in vacuum due to the lack of heat transport, resulting not only in a small transmission but also in a final melting and destruction of the fibre waist. Since this experiment is heading for combining chip structures with the nanofibre, the latter has to be mounted very close to the surface, which poses an additional risk for mechanical destruction or contamination. A more reproducible mounting procedure is desirable in the future, using for example a translation stage.

Physics

The main physical result is the first test of a nanofibre coupling to cold atoms close to a surface. This could also be achieved with a nanofibre with a Fabry-Perot resonator built of two laser-written fibre Bragg mirrors. The free-space cooparativity of the bare nanofibre-atom system has been measured to be $C = 0.08$ for thermally expanding atoms. It could also be shown that the magnetic substructure makes it possible to control the relative position of MOT and nanofibre in a precise way. The coupling of the MOT to the nanofibre cavity has been shown, but the inhomogeneous broadening of the atoms directly loaded from the switched-off MOT makes a quantitative discussion of the atom-cavity coupling difficult. An estimation for the cooparativity has been made by using a full fit to the transmission spectrum, and also by measuring the frequency shift of the cavity. The former gives a cooperativity of $C = (6.6 \pm 2.5)$, the latter gives a lower estimate of $C = 0.5$, both for the largest atomic arrival rate at the cavity. The source of the large inhomogeneous broadening is not known yet. It could be due to a different Zeeman shift of atoms being in different sub-states in a remaining magnetic field 1 ms after the switch-off. This can be avoided by optically pumping into a defined magnetic sublevel and loading a magnetic traps. Since in the experiment a maximum magnetic field 50 G is used, there have to be other causes, for example the van-der-Waals force in the vicinity of the nanofibre. Finally a comparison of the performance of the bare and the cavity fibre can be given. The absorbance A, defined by

$$\left(\frac{P_{tr}}{P_{in}}\right) = 10^{-A}, \tag{12.1}$$

describes the attenuation of the transmitted due the presence of the atoms. It is a measure for the optical depth in a decadic description. In Table 12.1 the maximum values for the free-space A_{fs} and cavity absorbance A_{cav} are shown, as well as their relation to the free-space optical density and the cavity cooperativity. For better comparison between both cases, the values are taken for similar shapes of the atomic arrival signal, so that the atom number near the nanofibre is on the same order of magnitude. The enhancement factor of the cavity defined by the ratio of the absorbances with and without the cavity gives 14.3 ± 1 which is close to the theoretical value $\mathcal{F}/\pi \approx 18$.

Parameter	Definition	Value
A_{fs}	$\frac{10}{\ln(10)} OD_{fs}$	1.61 dB
A_{cav}	$\frac{10}{\ln(10)} 2\ln(1+2C)$	23.1 ± 1.5 dB
A_{cav}/A_{fs}	OD_{cav}/OD_{fs}	14.3 ± 1

Table 12.1.: Measured absorbance, defined in eq. 12.1 as the attenuation due the presence of atoms, shown for the bare fibre (A_{fs}) and for the cavity (A_{cav}). Their ratio gives the enhancement of the absorption due to the presence of the atoms. Also shown is the relation of the absorbance to the measured parameters of both systems (see their respective discussion in Chapter 10 and Chapter 11)

12.2. Outlook: a nanofibre cavity close to an atom chip

The final goal of the nanofibre cavity experiment is its combination with an atom chip. Mounting the nanofibre parallel to an elongated magnetic trap provided by the chip wires should give a good overlap of the atom cloud and the evanescent light field at the nanofibre and thus a large optical density. This is a prerequisite for many the experiments proposed in the introduction, such as EIT and slow light, quantum repeaters and 1d polariton gases. The atom chip also provides ultra-cold samples of atoms, which should result in long coherence times necessary for storage or number squeezing of light pulses. In order to improve the control of the fibre cavity a second pair of Bragg mirrors in a far off-detuned region of the spectrum compared to the rubidium

D2 transition will be added to a new fibre cavity. Then it should be possible to stabilise the cavity during the measurement without disturbing the atoms, also it could provide the possibility of shining in a strong off-resonant light field acting as an optical trap.

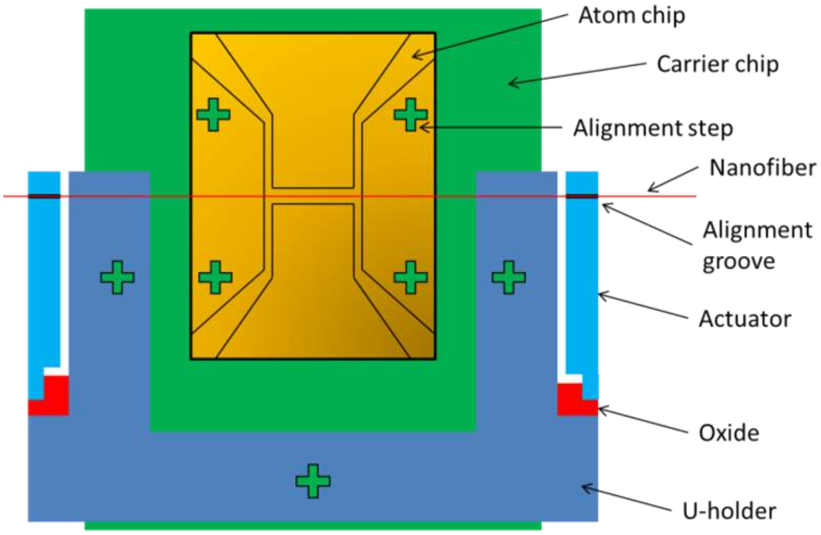

Figure 12.1.: Proposed new experiment: The nanofibre is mounted with micrometer precision along the central chip wire using micro-fabrication, allowing a good overlap of the light field and the BEC, trapped by the wire. The cavity length can be precisely tuned by mounting the fibre onto micro-actuators.

As a second step the nanofibre can be aligned with the chip trap with micrometer precision using micro-fabrication (see Figure 12.1). Additionally the fibre can be mounted on a micro-actuator. Besides increasing the controllability of the cavity length, it can also produce a movable standing wave potential inside the cavity. This could be used to excite phonons in the BEC. By studying the response of a condensate to such an excitation, new insights into the relaxation process of a many-body system could be gained. By controlling the cavity length the response of the atomic ensemble to the quantum field of the cavity could be observed and the phenomenon of self-organisation could be studied [66].

A. SU-8 micro-structures for integrated optics

For a new fluorescence detector (introduced in section 7.4) a two layer holding structure (as a result see Figure A.1) is needed in order to hold fibres with two different diameters, 125 μm and 230 μm. The thick fibre lies on directly on the substrate and needs a holding groove with a height of $\geq$ 200 μm and the thin fibre has to be mounted at a height of $\approx$ 60 μm to have the optical axes of both fibres in the same plane. Due to technical reasons it is easier to fabricate these two layers of different geometries in a three-layer process, thus splitting the upper layer into two fabrication steps using the same lithography mask as can be seen in Figure A.1. In the following table (A) an instruction for this three layer process is given, which results in bottom-to-top thicknesses of $\approx$ 60 μm, $\approx$ 100 μm and $\approx$ 100 μm, respectively. By changing the exposure time of the individual layers the undercut can be controlled in such a way that the overhanging structures additionally enclose the fibres from the top (see Figure A.3).

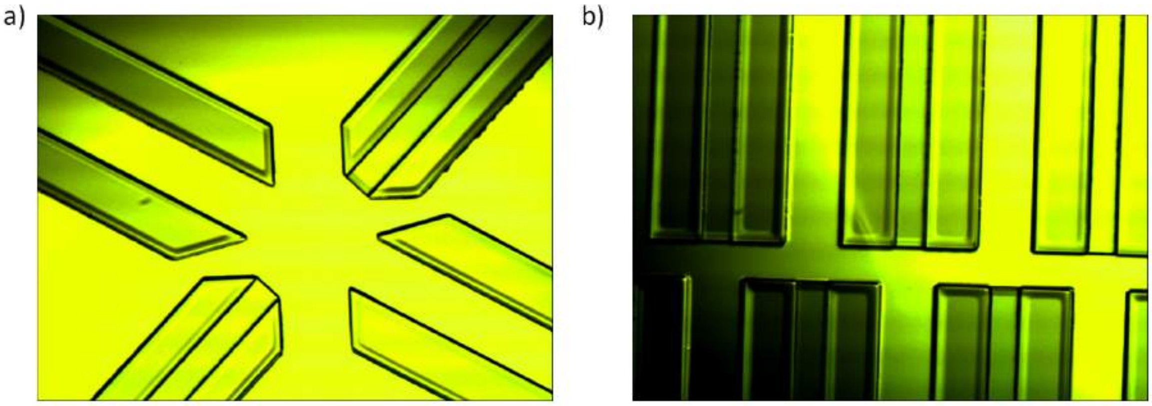

Figure A.1.: Top view of the final triple-layer SU-8 structures in a test geometry for a possible new fluorescence (**a)**) and absorption (**b)**) detector, respectively.

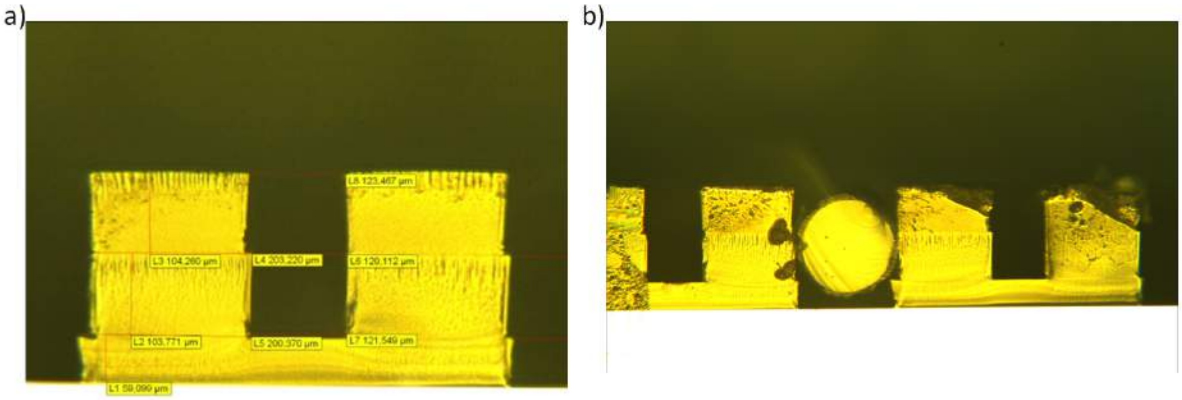

Figure A.2.: Cross section of the final SU-8 design with the measured widths and height of the different layers **a)** and a with an actual MM fibre mounted in the groove **b)**. The fabrication process is understood but it can be observed that the test structures are not wide enough to fit the fibre in as whole.

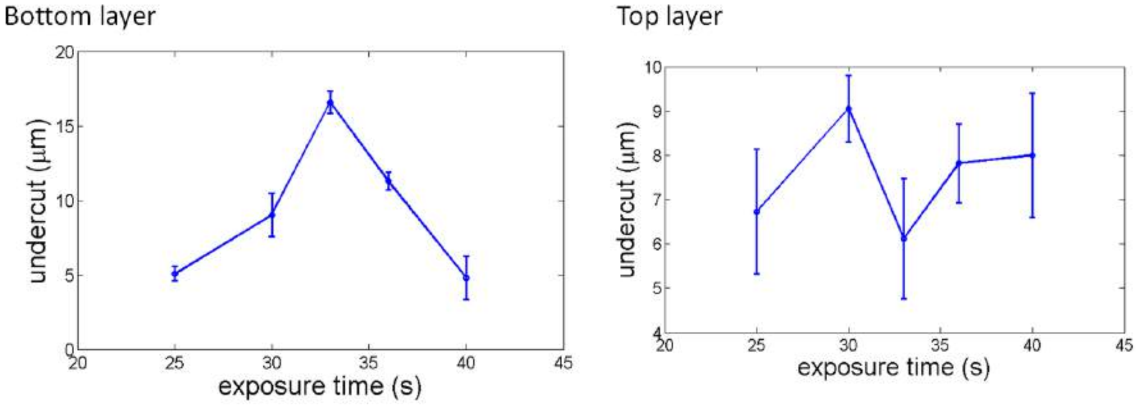

Figure A.3.: Undercut of the bottom and top holding structure versus exposure time. The error bars are defined by the standard deviation of length measurements of similar structures at different sites on the chip.

Table A.1.: Fabrication instruction for a three-layer process with a thickness of ≈ 60 μm, ≈ 100 μm and ≈ 100 μm for the respective layer.

PECVD a thin SiO layer onto the gold surface	Thickness: a few $\mathring{A}$
Clean in distilled water and dry an hot plate	$T = 200$ °C
Spin **first layer** SU-8 50	500 rpm for 20 s then 3000 rpm for 20 s
Prebake first step	10 min $T = 65$ °C, 6 min ramp to $T = 95$ °C
Prebake second step	leave at $T = 95$ °C for 2 h
Expose in mask aligner (bottom mask)	$t_{expose} = 25$ s
Postbake first step	1 min $T = 65$ °C, 2 min ramp to $T = 95$ °C
Postbake second step	leave at $T = 95$ °C for 9 min
Rinse in SU-8 developer	≥ 15 min
Rinse in isopropanol	1 min
Rinse in distilled water	
Spin **second layer** SU-8 50	500 rpm for 20 s then 1500 rpm for 20 s
Prebake first step	10 min $T = 65$ °C, 6 min ramp to $T = 95$ °C
Prebake second step	leave at $T = 95$ °C for 2 h
Expose in mask aligner (top mask)	$t_{expose} = 30$ s
No development and no postbake!	
Spin **third layer** SU-8 50	500 rpm for 20 s then 1500 rpm for 20 s
Prebake first step	10 min $T = 65$ °C, 6 min ramp to $T = 95$ °C
Prebake second step	leave at $T = 95$ °C for 9 min
Expose in mask aligner (top mask)	$t_{expose} = 33$ s
Postbake first step	1 min $T = 65$ °C, 2 min ramp to $T = 95$ °C
Postbake second step	leave at $T = 95$ °C for 9 min
Rinse in SU-8 developer	1 day!
Rinse in isopropanol and distilled water	

B. Nanofibre experiment: technical drawings

The drawings of the components custom designed for the nanofibre cavity experiment are the following:

1. Bias coils B.1
2. Up down coils B.2
3. Experiment flange B.3
4. AlN insulating substructure B.4
5. Copper H structure B.5
6. Nanofibre Macor holder B.6

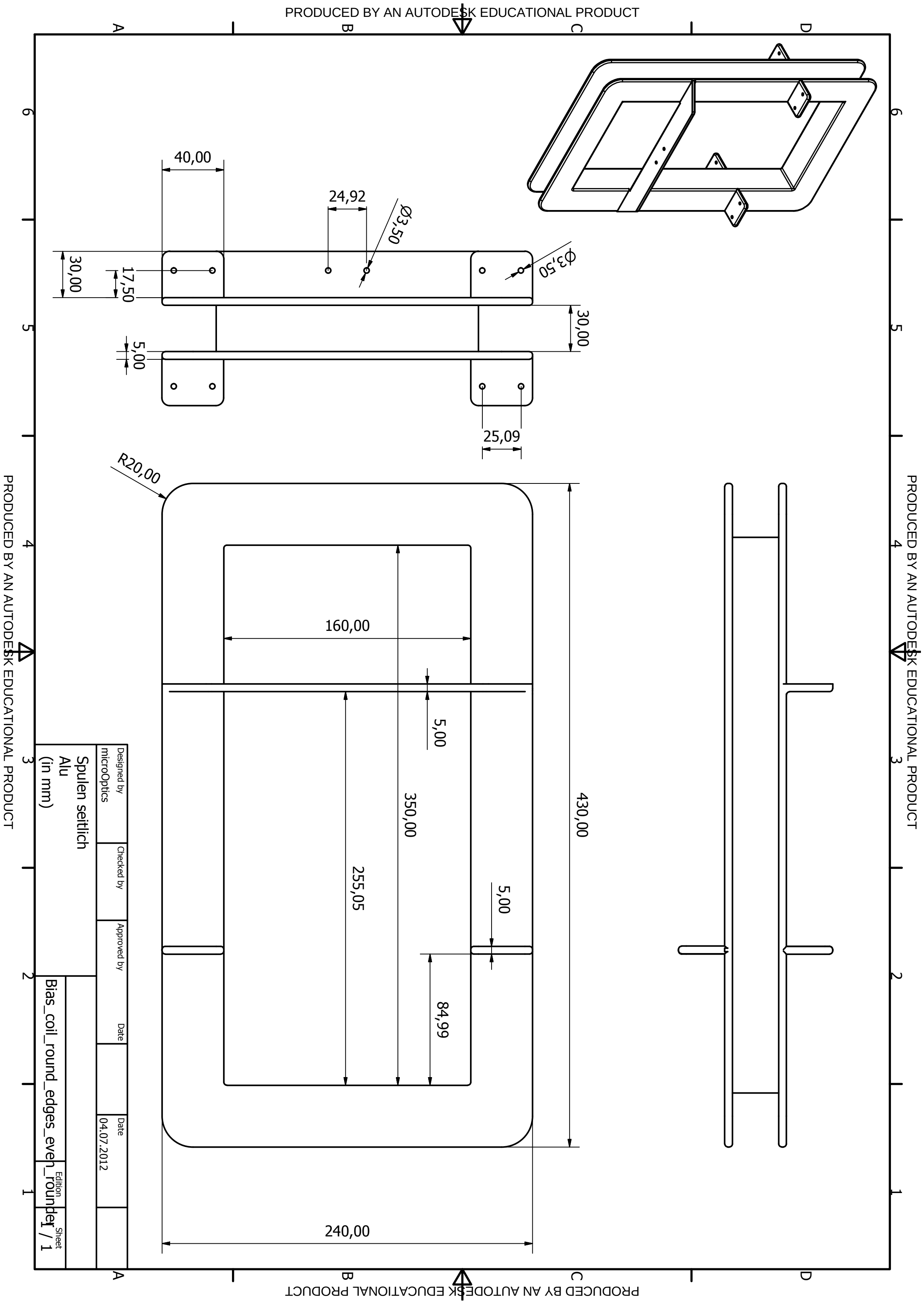

Figure B.1.: Bias coils

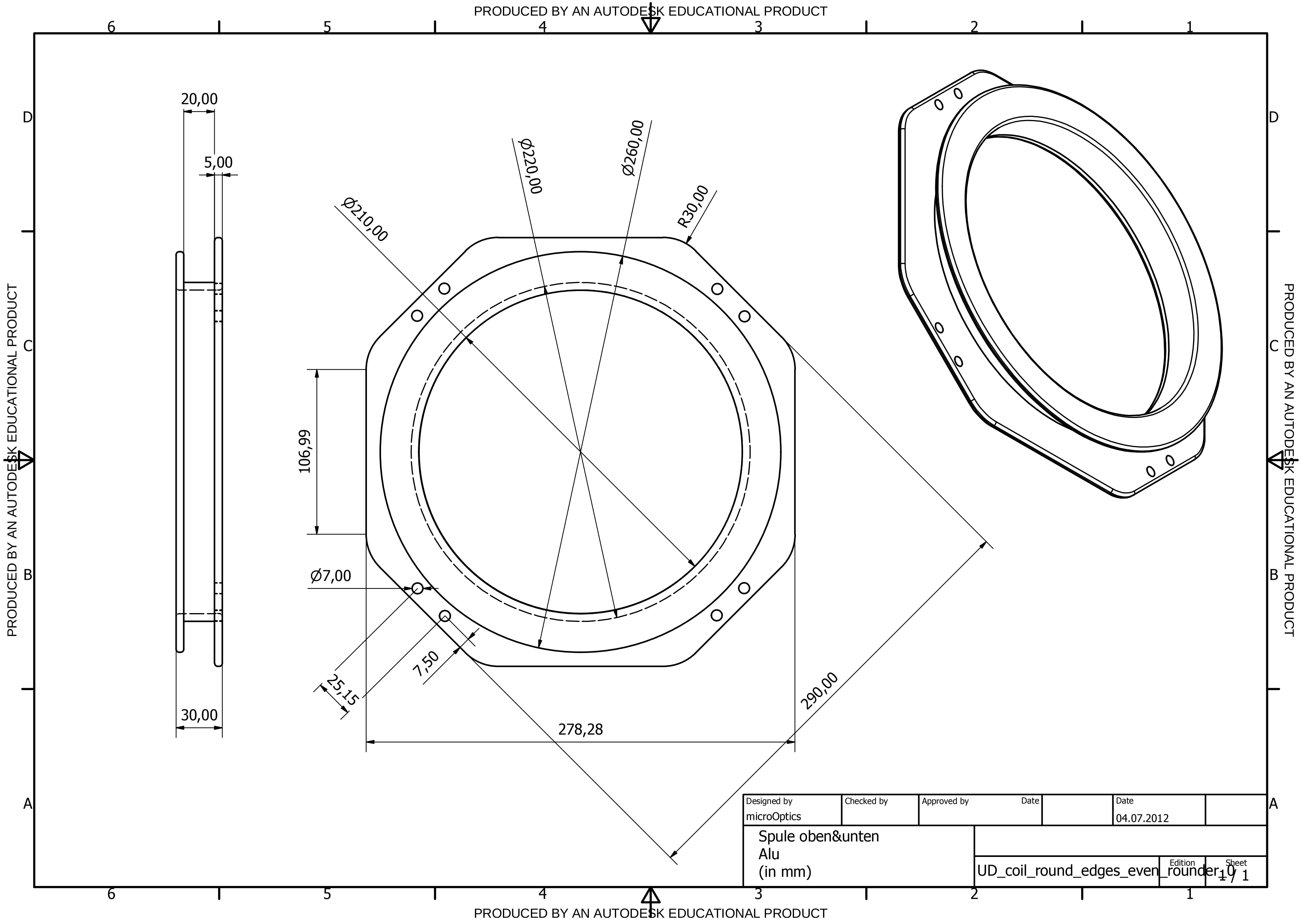

Figure B.2.: Up-down coils

8 inchLesker big currents.pdf

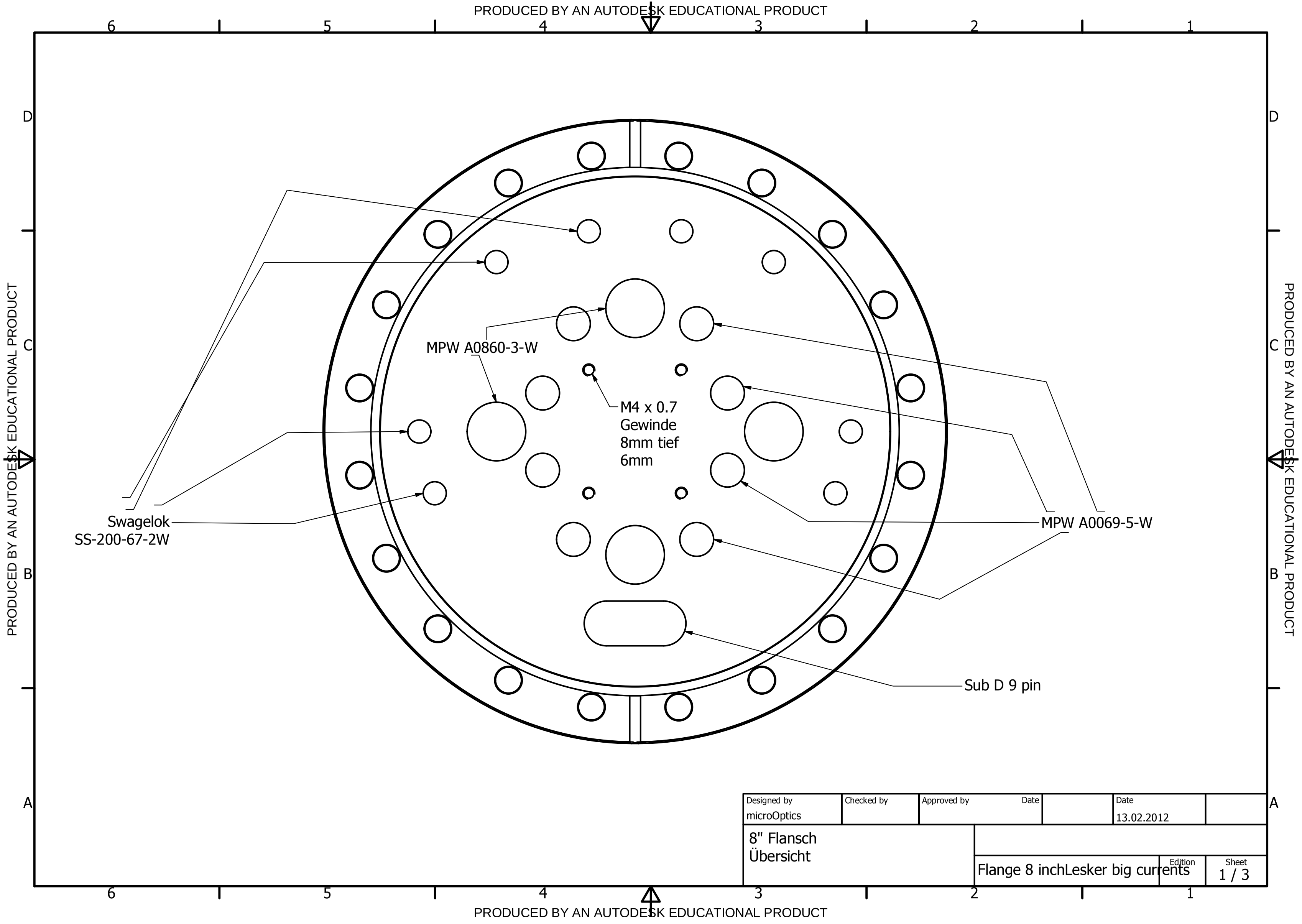

Figure B.3.: Experiment flange

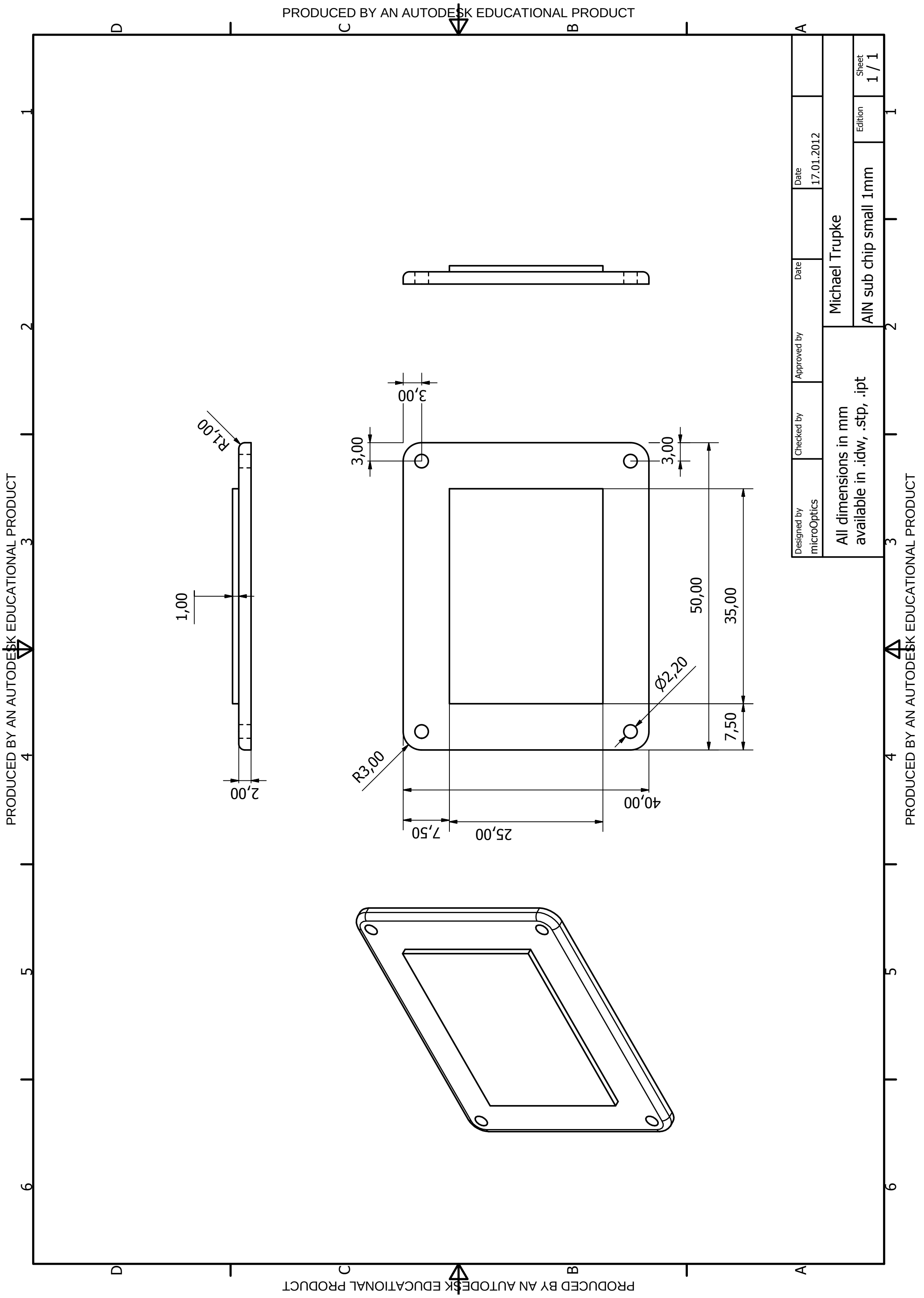

Figure B.4.: AlN insulating substructure

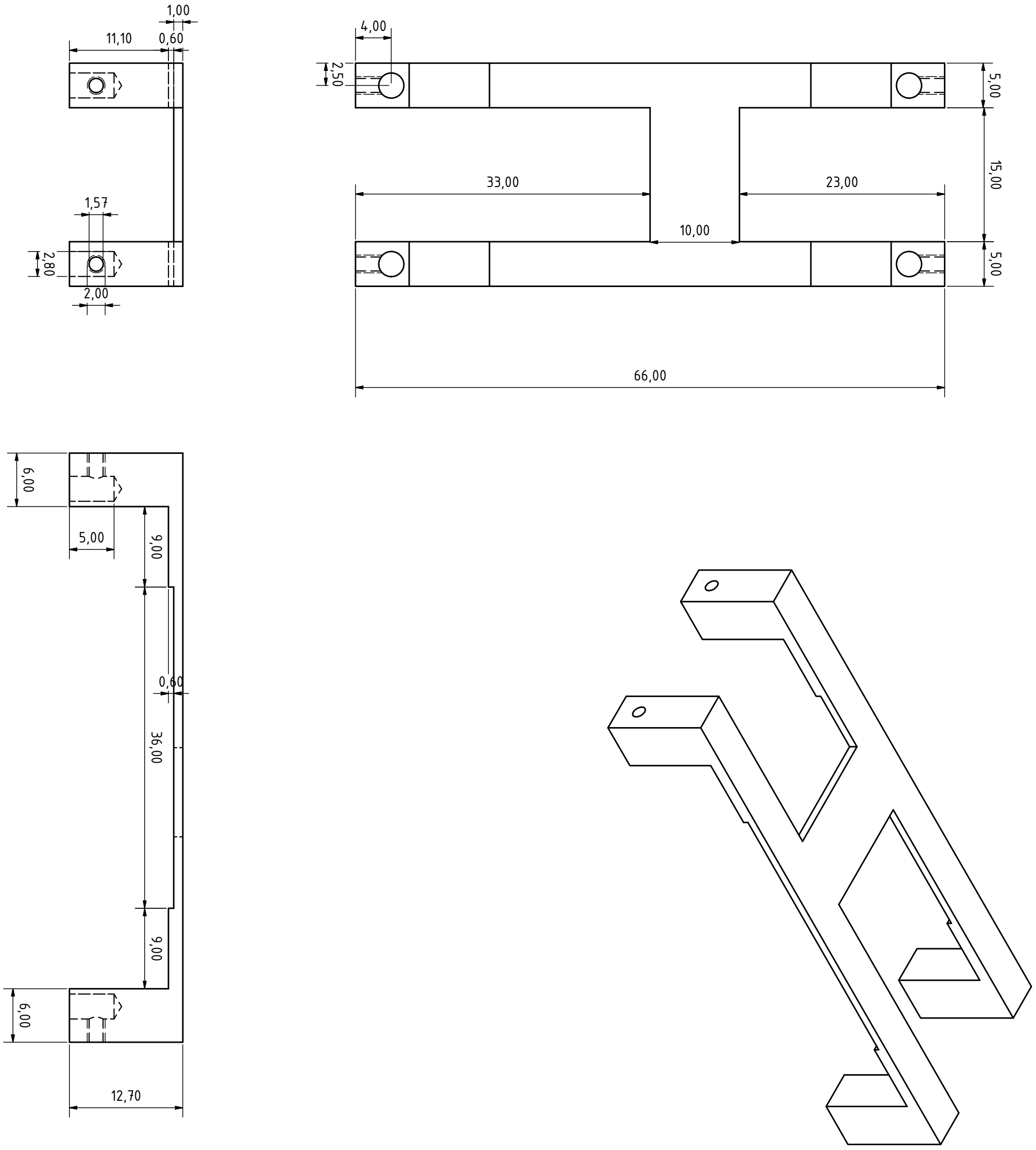

Figure B.5.: Copper H structure

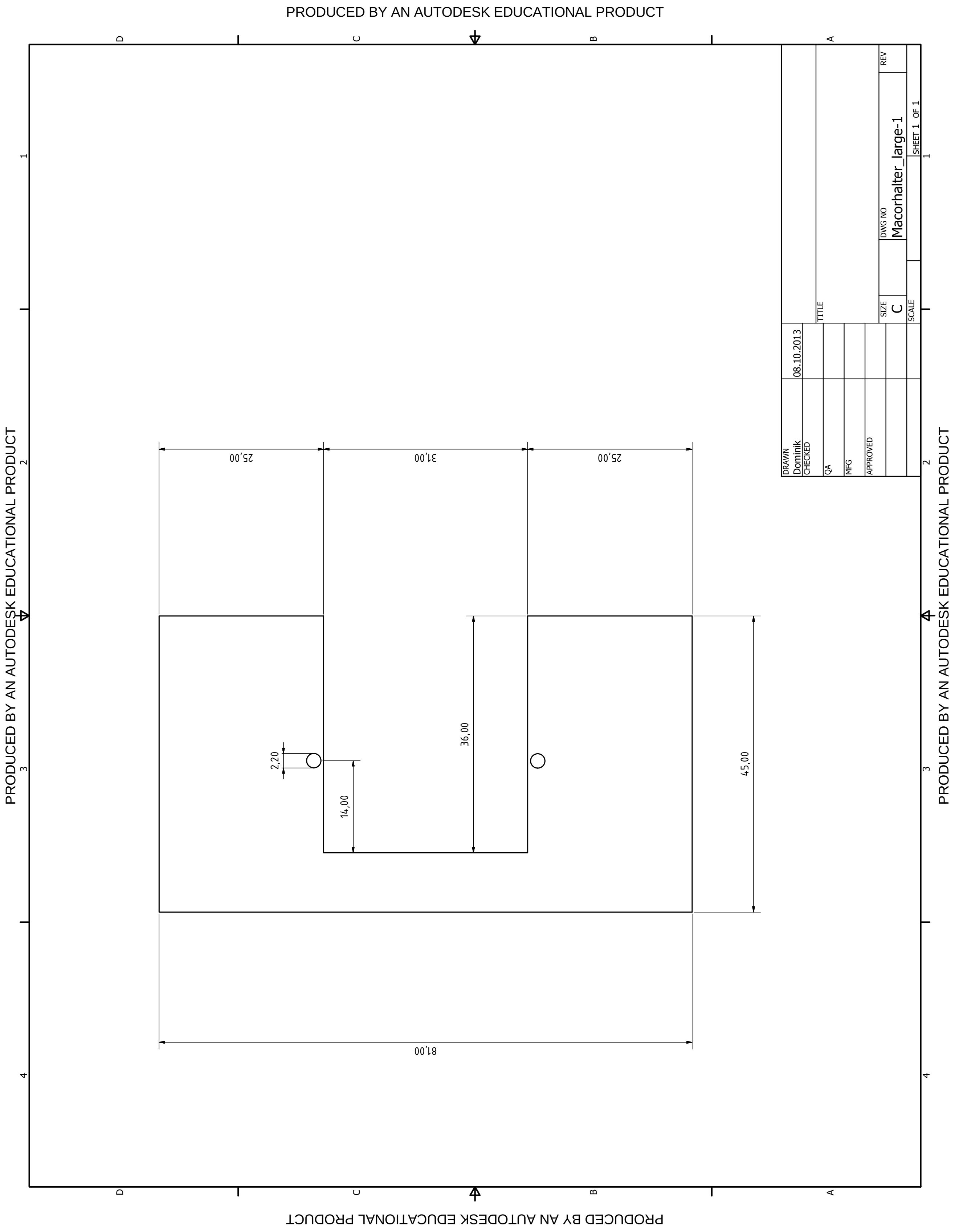

Figure B.6.: Nanofibre Macor holder (height 2 mm)

Bibliography

[1] E R Abraham and E A Cornell. Teflon feedthrough for coupling optical fibers into ultrahigh vacuum systems. *Applied optics*, 37:1762–1763, 1998.

[2] A H Van Amerongen, J J P Van Es, P Wicke, K V Kheruntsyan, and N J Van Druten. Yang-Yang Thermodynamics on an Atom Chip. *Phys. Rev. Lett.*, 090402(March):13–15, 2008.

[3] M H Anderson, J R Ensher, M R Matthews, C E Wieman, and E A Cornell. Observation of Bose-Einstein Condensation in a Dilute Atomic Vapor. *Science*, 269(5221):198–201, 1995.

[4] Anonymous. Proceedings of the american physical society. *Phys. Rev.*, 69:674–674, Jun 1946.

[5] Bindiya Arora, M. S. Safronova, and Charles W. Clark. Magic wavelengths for the np-ns transitions in alkali-metal atoms. *Physical Review A - Atomic, Molecular, and Optical Physics*, 76, 2007.

[6] Roberto Balbinot, Alessandro Fabbri, Serena Fagnocchi, Alessio Recati, and Iacopo Carusotto. Nonlocal density correlations as a signature of Hawking radiation from acoustic black holes. *Physical Review A - Atomic, Molecular, and Optical Physics*, 78, 2008.

[7] Kristian Baumann, Christine Guerlin, Ferdinand Brennecke, and Tilman Esslinger. Dicke quantum phase transition with a superfluid gas in an optical cavity. *Nature*, 464(7293):1301–1306, 2010.

[8] G Binnig, Ch. Gerber, E Stoll, T. R. Albrecht, and C. F Quate. Atomic Resolution with Atomic Force Microscope. *Europhysics Letters (EPL)*, 3:1281–1286, 1987.

[9] I. Bouchoule, N. J. van Druten, and C. I. Westbrook. *Atom Chips and One-Dimensional Bose Gases*, pages 331–363. Wiley-VCH Verlag GmbH Co. KGaA, 2011.

[10] R Hanbury Brown and R Q Twiss. A New Type of Interferometer for Use in Radio Astronomy. *Phil. Mag.*, 45:663, 1954.

[11] Robert Bücker. *Twin-atom beam generation in a one-dimensional Bose gas.* PhD thesis, Vienna University of Technology, 2013.

[12] D E Chang, V Gritsev, G Morigi, V Vuletic, M D Lukin, and E A Demler. Crystallization of strongly interacting photons in a nonlinear optical fibre. *Nat Phys*, 4(11):884–889, November 2008.

[13] Yves Colombe, Tilo Steinmetz, Guilhem Dubois, Felix Linke, David Hunger, and Jakob Reichel. Strong atom–field coupling for bose–einstein condensates in an optical cavity on a chip. *Nature*, 450(7167):272–276, 2007.

[14] W. Demtröder. *Experimentalphysik 3: Atome, Moleküle und Festkörper*. Experimentalphysik / Wolfgang Demtröder. Springer, 2005.

[15] Wolfgang Demtröder. *Experimentalphysik 2 Elektrizität und Optik*, volume 5. Auflage. 2009.

[16] S Dettmer, D Hellweg, P Ryytty, J Arlt, W Ertmer, K Sengstock, D Petrov, G Shlyapnikov, H Kreutzmann, L Santos, and M Lewenstein. Observation of Phase Fluctuations in Elongated Bose-Einstein Condensates. *Phys. Rev. Lett.*, 87(16):160406, 2001.

[17] A. Einstein. Zur Elektrodynamik bewegter Körper. *Annalen der Physik*, 17(10):891–921, 1905.

[18] V P Ermakov. Transformation of differential equations. *Univ. Izv. Kiev.*, 20:1, 1880.

[19] M Fleischhauer and M D Lukin. Quantum memory for photons: Dark-state polaritons. *Phys. Rev. A*, 65:22314, 2002.

[20] Michael Fleischhauer, Atac Imamoglu, and Jonathan P Marangos. Electromagnetically induced transparency: Optics in coherent media. *Rev. Mod. Phys.*, 77(2):633–673, 2005.

[21] R Folman, P Krüger, J Schmiedmayer, J Denschlag, and C Henkel. Microscopic atom optics: from wires to an atom chip. *Adv. At. Mol. Opt. Phys.*, 48:263–356, 2002.

[22] Ron Folman, Peter Krüger, Jörg Schmiedmayer, Johannes Denschlag, and Carsten Henkel. Microscopic Atomic Optics: From Wires to an Atomic Chip. *Advances in Atomic Molecular and Optical Physics*, 48:263–356, 2002.

[23] R Garcia-Fernandez, W Alt, F Bruse, C Dan, K Karapetyan, O Rehband, A Stiebeiner, U Wiedemann, D Meschede, and A Rauschenbeutel. Optical nanofibers and spectroscopy. *Appl. Phys. B*, 105(1):3–15, 2011.

[24] F Gerbier. Quasi-1D Bose-Einstein condensates in the dimensional crossover regime. *Europhys. Lett.*, 66(6):771–777, 2004.

[25] Roy J. Glauber. Coherent and incoherent states of the radiation field. *Phys. Rev.*, 131:2766–2788, Sep 1963.

[26] J. Viana Gomes, A. Perrin, M. Schellekens, D. Boiron, C. I. Westbrook, and M. Belsley. Theory for a hanbury brown twiss experiment with a ballistically expanding cloud of cold atoms. *Phys. Rev. A*, 74:053607, Nov 2006.

[27] Rudolf Grimm, Matthias Weidemüller, and Yurii B. Ovchinnikov. Optical Dipole Traps for Neutral Atoms. *Advances in Atomic, Molecular and Optical Physics*, 42(C):95–170, 2000.

[28] Serge Haroche. Nobel lecture: Controlling photons in a box and exploring the quantum to classical boundary*. *Rev. Mod. Phys.*, 85:1083–1102, Jul 2013.

[29] Lene Vestergaard Hau, S. E. Harris, Zachary Dutton, and Cyrus H. Behroozi. Light speed reduction to 17 metres per second in an ultracold atomic gas. *Nature*, 397:594–598, 1999.

[30] Gerald Hechenblaikner, Markus Gangl, Peter Horak, and Helmut Ritsch. Cooling an atom in a weakly driven high-q cavity. *Phys. Rev. A*, 58:3030–3042, Oct 1998.

[31] D Heine, W Rohringer, D Fischer, M Wilzbach, T Raub, S Loziczky, XiYuan Liu, S Groth, B Hessmo, and J Schmiedmayer. A single-atom detector integrated on an atom chip: fabrication, characterization and application. *New J. Phys.*, 12(9):95005, September 2010.

[32] Dennis Heine. *Single Atom Detection and Nonclassical Photon Correlations*. Ph.d. thesis, University of Heidelberg, 2008.

[33] Dennis Heine, Marco Wilzbach, Thomas Raub, Björn Hessmo, and Jörg Schmiedmayer. Integrated atom detector: Single atoms and photon statistics. *Physical Review A - Atomic, Molecular, and Optical Physics*, 79, 2009.

[34] Dennis Heine, Marco Wilzbach, Thomas Raub, Björn Hessmo, and Jörg Schmiedmayer. Integrated atom detector: Single atoms and photon statistics. *Physical Review A - Atomic, Molecular, and Optical Physics*, 79, 2009.

[35] Tin-Lun Ho and Michael Ma. Quasi 1 and 2d dilute bose gas in magnetic traps: Existence of off-diagonal order and anomalous quantum fluctuations. *Journal of Low Temperature Physics*, 115(1-2):61–70, 1999.

[36] A. Imambekov, I. E. Mazets, D. S. Petrov, V. Gritsev, S. Manz, S. Hofferberth, T. Schumm, E. Demler, and J. Schmiedmayer. Density ripples in expanding low-dimensional gases as a probe of correlations. *Physical Review A - Atomic, Molecular, and Optical Physics*, 80, 2009.

[37] Wolfgang Ketterle, Dallin S Durfee, and D M Stamper-Kurn. Making, probing and understanding Bose-Einstein condensates. In Massimo Inguscio, Sandro Stringari, and Carl E Wieman, editors, *Bose-Einstein Condens. At. gases*, pages 76–176. IOS Press, Amsterdam, 1999.

[38] Fam Le Kien, J. Q. Liang, K. Hakuta, and V. I. Balykin. Field intensity distributions and polarization orientations in a vacuum-clad subwavelength-diameter optical fiber, 2004.

[39] H J Kimble. Strong interactions of single atoms and photons in cavity qed. *Physica Scripta*, 1998(T76):127, 1998.

[40] Daniel Kleppner. Inhibited spontaneous emission. *Phys. Rev. Lett.*, 47:233–236, Jul 1981.

[41] Elliott H Lieb and Werner Liniger. Exact Analysis of an Interacting Bose Gas. I. The General Solution and the Ground State. *Phys. Rev.*, 130(4):1605–1616, 1963.

[42] Eric Lindner, Christoph Chojetzki, Sven Brückner, Martin Becker, Manfred Rothhardt, and Hartmut Bartelt. Thermal regeneration of fiber Bragg gratings in photosensitive fibers. *Opt. Express*, 17(15):12523–12531, 2009.

[43] S. Manz, R. Bücker, T. Betz, Ch Koller, S. Hofferberth, I. E. Mazets, A. Imambekov, E. Demler, A. Perrin, J. Schmiedmayer, and T. Schumm. Two-point density correlations of quasicondensates in free expansion. *Physical Review A - Atomic, Molecular, and Optical Physics*, 81, 2010.

[44] Guido Martina, Romano Scarpa, and Giovan Battista Carpi. Die Macht des Goldes. *LTB*, 93:62.

[45] N Masuhara, J M Doyle, J C Sandberg, D Kleppner, T J Greytak, H F Hess, and G P Kochanski. Evaporative Cooling of Spin-Polarized Atomic Hydrogen. *Phys. Rev. Lett.*, 61:935, 1988.

[46] Chiara Menotti and Sandro Stringari. Collective oscillations of a one-dimensional trapped Bose-Einstein gas. *Phys. Rev. A*, 66(4):43610, 2002.

[47] Todd P Meyrath. Electromagnet Design Basics for Cold Atom Experiments Some Theory of Electromagnets Exact Field of a Circular Current Loop. *Res. Gate*, 2(1):1–13, 2004.

[48] C Monroe, W Swann, H Robinson, and C Wieman. Very Cold Trapped Atoms in a Vapor Cell. *Phys. Rev. Lett.*, 65:1571, 1990.

[49] Torben Müller, Bruno Zimmermann, Jakob Meineke, Jean-Philippe Brantut, Tilman Esslinger, and Henning Moritz. Local observation of antibunching in a trapped fermi gas. *Phys. Rev. Lett.*, 105:040401, Jul 2010.

[50] M Naraschewski and R Glauber. Spatial coherence and density correlations of trapped Bose gases. *Phys. Rev. A*, 59(6):4595–4607, 1999.

[51] Z.Y. Ou, C.K. Hong, and L. Mandel. Relation between input and output states for a beam splitter, 1987.

[52] Oliver Penrose and Lars Onsager. Bose-Einstein Condensation and Liquid Helium. *Phys. Rev.*, 104(3):576–584, November 1956.

[53] C Pethick and H Smith. *Bose-Einstein Condensation in Dilute Gases.* Cambridge University Press, 2002.

[54] D S Petrov, G V Shlyapnikov, and J T M Walraven. Regimes of Quantum Degeneracy in Trapped 1D Gases. *Phys. Rev. Lett.*, 85(October):3745–3749, 2000.

[55] L P Pitaevskii and A Rosch. Breathing modes and hidden symmetry of trapped atoms in two dimensions. *Phys. Rev. A*, 55(2):853–856, 1997.

[56] Angus Prain, Serena Fagnocchi, and Stefano Liberati. Analogue cosmological particle creation: Quantum correlations in expanding Bose-Einstein condensates. *Phys. Rev. D*, 82(10):105018, November 2010.

[57] J Reichel, W Hänsel, P Hommelhoff, and T W Hänsch. Applications of integrated magnetic microtraps. *Appl. Phys. B*, 72:81, 2001.

[58] Helmut Ritsch, Peter Domokos, Ferdinand Brennecke, and Tilman Esslinger. Cold atoms in cavity-generated dynamical optical potentials. *Rev. Mod. Phys.*, 85:553–601, Apr 2013.

[59] W Rohringer, D Fischer, F Steiner, I E Mazets, J Schmiedmayer, and M Trupke. Scale invariance and shortcuts to adiabaticity in a one-dimensional Bose gas. 1(3):1–3, 2014.

[60] Wolfgang Rohringer. Dynamics of One-Dimensional Bose Gases in Time-Dependent Traps 1d Bose gases I. (April), 2014.

[61] C. Sayrin, C. Clausen, B. Albrecht, P. Schneeweiss, and A. Rauschenbeutel. Storage of fiber-guided light in a nanofiber-trapped ensemble of cold atoms. *Optica*, 2(4):353–356, Apr 2015.

[62] Anthony E. Siegman. *Lasers.* University Science Books, 1986.

[63] David A Smith, Simon Aigner, Sebastian Hofferberth, Michael Gring, Mauritz Andersson, Stefan Wildermuth, Peter Krüger, Stephan Schneider, Thorsten Schumm, and Jörg Schmiedmayer. Absorption imaging of ultracold atoms on atom chips. *Optics express*, 19:8471–8485, 2011.

[64] Haruka Tanji-Suzuki, Ian D. Leroux, Monika H. Schleier-Smith, Marko Cetina, Andrew T. Grier, Jonathan Simon, and Vladan Vuletić. Interaction between Atomic Ensembles and Optical Resonators. Classical Description. *Advances in Atomic, Molecular and Optical Physics*, 60:201–237, 2011.

[65] Limin Tong, Rafael R Gattass, Jonathan B Ashcom, Sailing He, Jingyi Lou, Mengyan Shen, Iva Maxwell, and Eric Mazur. Subwavelength-diameter silica wires for low-loss optical wave guiding. *Nature*, 426(6968):816–819, 2003.

[66] Valentin Torggler and Helmut Ritsch. Adaptive multifrequency light collection by self-ordered mobile scatterers in optical resonators. *Optica*, 1(5):336–342, Nov 2014.

[67] Philipp Treutlein, Claudiu Genes, Klemens Hammerer, Martino Poggio, and Peter Rabl. Hybrid mechanical systems. In *Cavity Optomechanics*, pages 327–351. Springer Berlin Heidelberg, 2014.

[68] Stefan Wildermuth. *One-dimensional Bose-Einstein condensates in micro-traps*. Ph.d. thesis, University of Heidelberg, 2005.

[69] Marco Wilzbach. *Single atom detection on an atom chip with integrated optics*. Ph.d. thesis, University of Heidelberg, 2007.

[70] Marco Wilzbach, Dennis Heine, Sönke Groth, Xiyuan Liu, Thomas Raub, Björn Hessmo, and Jörg Schmiedmayer. Simple integrated single-atom detector. *Optics letters*, 34:259–261, 2009.

[71] C Wuttke, M Becker, S Brückner, M Rothhardt, and A Rauschenbeutel. Nanofiber Fabry–Perot microresonator for nonlinear optics and cavity quantum electrodynamics. *Opt. Lett.*, 37(11):1949–1951, 2012.

Acknowledgements

This thesis is the product of many people's effort with different contributions: First of all I thank Jörg Schmiedmayer for giving me the opportunity to work in this field and this team. I thank him for his faith in our experiment and for getting us focused at the right times. I thank Michael Trupke for being a good boss and organiser as well as for being an expert in every aspect of experimental physics. I inherited a decent experiment from Dennis Heine, Thomas Raub, Marco Wilzbach and Björn Hessmo, which they had to set up a second time here in Vienna. I am standing on the shoulders of giants, but especially on the giant shoulders of Dennis. I am grateful to have worked with my two lab mates and Phd colleagues Wolfgang Rohringer and Florian Steiner on the frontier of science and technology. I was collaborating with Wolfgang almost my entire academic life and I have never grown tired of discussing science and other things with him. These discussions and Wojcek Zurek are responsible for a complete change in my view on quantum theory. Without Florian the nanofibre experiment would never have come into existence, I would still try to get the test vacuum chamber clean. The main reason for the nice setup we have now is his dedication to the work on it. I have to thank the long term memory of our group, Stephan Schneider and Thorsten Schumm, who know every aspect of cold atoms experiments because they seem to have built almost all of them. Stephan Schneider showed me how to handle vacuum parts, when no one else in the group remembered what a turbo pump looks like. I have to thank Thorsten especially for being the experiment's interim supervisor, who helped us a lot to make the machine BEC-worthy although he was busy with other projects. I thank Igor Mazets for the derivation of the Ermakov equation and for being our first address for problems in quantum liquid theory. I thank Christian Koller for sharing with me not only some beers but also the experience of explaining BECs to - and receiving explanations of catalysis from - chemists in the FunMat doctoral college. I also thank all the other members of our quantum optics group for all the wisdom and experience they had to share and all the fun I had, making even the worst situations in the lab bearable. I had nice discussions with almost all of them. The existence of the nanofibre cavity experiment lay in the steady hands of Thomas Hoinkes, who managed to pull the literally last cavity fibre to a nanowaist without destroying it. We really discussed, from a psychological point-of-view, whether it is better to tell him or not to, that it is the last try. The whole group relies on the patience and the experience of Matthias Stüwe, who spent weeks in the clean room to find the right parameters for the new SU-8 structures, where the fabrication of one sample takes more than a day. I thank the guys from the electronics workshop for their effort especially in repairing the high current switches on a weekly basis. I thank the secretaries for their patience in explaining me those boring administrative tasks. I thank Arno Rauschenbeutel and all the members of his quantum technology group for their support and for sharing all their knowledge about nanofibres. I always saw collaborators in them in the difficult task to gain new insights about the system nanofibre-atom. I thank Manfred Rothhardt and his group at the institute for photonic technology in Jena for laser-writing the Bragg mirrors for our fibre cavity. I thank the diploma students at our experiment, Georg Winkler for achieving the first optical pancake trap underneath an atom chip in the world and Michaela Trimmel for building the first version of the best absorption imaging in the group. I thank all project or bachelor students for the support in our experiment and for letting me practise my skills as a supervisor. In chronological order I thank Sarah Reisenbauer for setting up our new repump laser, Cyrille Solaro for testing the feasibility of new fibre-based integrated optics, Cesare Martinelli for frequency modulating a diode laser, Roman Kastner and Franz Leberl for setting up the dipole barrier used in the micro-optics experiment, Sebastian Ecker and Florian Prawits for testing the first batch of Bragg mirror cavities, Benedikt Pesendorfer for building a Mach-Zehnder interferometer for spatially separating the hyperfine-split lines of rubidium, Michael Wagner for building an improved objective for our absorption imaging. I thank Don Rosa, Carl Barks, Giovan Battista Carpi, Guido Martina, Romano Scarpa for giving me the initial education in modern culture. I thank my parents and my sister for letting me keep my stubbornness and for stimulating my curiosity which to my opinion are the two necessary ingredients to do science. I owe my partial sanity to those people I drink beer with after science, Flo and Karin, Guido and Angie, Michl, Thomas and Carina. I also thank all the guests at Café Anno, who did not find a place because I occupied the last table alone writing this thesis. Finally I have to thank Livia for being patient with me, whenever I had to work instead of playing with her, and Kathi for the effort of making my work on this thesis as comfortable as possible.

È la virtute un raggio
Di celeste bellezza,
Pregio dell'alma ond'ella sol s'apprezza.
Questa di temp'oltraggio
Non tem', anzi maggiore
Nell'uom rendono gl'anni il suo splendore.
Orfeo vinse l'Inferno e vinto poi
Fu dagl'affetti suoi.
Degno d'eterna gloria
Fia sol colui ch'avrà di sé vittoria.
"L'orfeo" (Claudio Monteverdi), forth act, chorus of the spirits